Depth resolved investigation of ion beam induced pattern formation on silicon using X-ray methods

DISSERTATION

zur Erlangung des Grades eines Doktors

der Naturwissenschaften

vorgelegt von

M. Sc. Behnam Khanbabaee Patekhour

eingereicht bei der Naturwissenschaftlich-Technischen Fakultät

der Universität Siegen

Siegen 2014

Gutachter:	Prof. Dr. Dr. h.c. Ullrich Pietsch
	Prof. Dr. Dr. h.c. Bernd Rauschenbach
Prüfer:	Prof. Dr. Hans Dieter Dahmen
	Prof. Dr. Christian Gutt

Tag der mündlichen Prüfung: 30.04.2014

Abstract

In the present work, ion beam induced pattern formation on silicon surfaces is investigated, which was induced by off-normal irradiation of Fe ions. It is observed that the self-organized surface patterning takes place when the ion fluence exceeds a certain limit. The influence of the ion parameters on the patterning mechanism was investigated via monitoring of the near surface area where incorporated Fe ions play a dominant role.

In a first step, ion beam induced surface density variation was studied as a function of ion parameters. Conventional X-ray reflectivity revealed the formation of a nm sub-surface layer with incorporated Fe atoms. Using X-ray reflectivity, no major dependence of the surface density on the ion fluence could be obtained. Thus, a new powerful technique with higher surface sensitivity was applied based on extremely asymmetrical X-ray diffraction methods. The density information was extracted from the shift of the diffraction peak caused by refraction of the X-ray beam at the air-sample interface. Simulations based on the dynamical theory of X-ray diffraction revealed a decrease of the density for increasing ion fluence in a region close to the surface. It shows that there is a threshold value for ion fluence leading to reduction of surface density. The obtained results reveal that the change of local density contributes to the development of the pattern on the surface.

In a second step, Fe-silicide formation in various stoichiometries was investigated in the amorphized surface region of crystalline Si(100) after irradiation with Fe ions. A depth resolved analysis of chemical states of Si and Fe atoms in the near surface region was performed by combining X-ray photoelectron spectroscopy and X-ray absorption spectroscopy using synchrotron radiation. The formation of silicide bonds of different stoichiometric composition changing from an Fe-rich silicide (Fe_3Si) close to the surface into a Si-rich silicide ($FeSi_2$) towards to the inner interfaces was observed. This observation shows that the presence of chemically bonded iron close to the surface is an important prerequisite of pattern formation.

In a third step, the recrystallization of the pre-formed Fe-silicides of various stoichiometries was investigated below the amorphized surface of crystalline Si(100). A thermal annealing process was applied in the range between room temperature and 800°C. Depth profiling by grazing incidence X-ray diffraction confirmed that a ε-FeSi phase was formed close to the surface changing to a β-$FeSi_2$ phase with lower Fe content at larger depths. Both phases are distributed

with different ratios within the Fe-Si layer at smooth and patterned surfaces, corresponding to low and high ion fluences, respectively.

In the last step, the obtained results were examined for pattern formation on Si(001) surfaces under normal incident Kr ion bombardment with simultaneous incorporation of Fe atoms. It was verified that the surface patterning takes place only when the incorporated Fe concentration again exceeds a certain limit. For a high Fe concentration the ripple formation is accompanied by the enrichment of Fe atoms at the top part of ripples, whereas no such Fe enhancement is found for a low Fe concentration at samples with smooth surfaces. Modeling of the measured X-ray photoelectron spectroscopy and X-ray absorption spectroscopy spectra reveals the appearance of different silicide phases with a decreasing Fe content from top towards the volume.

Zusammenfassung

In der vorliegenden Arbeit wird die Musterbildung auf Siliziumoberflächen durch den Beschuss mit Eisenionen unter schrägem Einfallswinkeln untersucht. Experimentell wird beobachtet, dass es zu selbstorganisierter Strukturbildung an der Oberfläche kommt, wenn die Ionendosis (Fluenz) einen bestimmten Schwellenwert überschreitet. In dieser Arbeit wird der Einfluss der Ionenstrahl-Parameter auf die Musterbildung untersucht. Insbesondere wird die Region nahe der Oberfläche, in welcher die Fe-Ionen eine entscheidende Rolle bei der Musterbildung spielen, mittels Oberflächensensitiver Röntgenstreuung untersucht.

In einem ersten Schritt wird das Dichteprofil nahe der Oberfläche als Funktion von Ionenenergie und Fluenz untersucht. Röntgenreflektometrie zeigt dabei die Ausbildung eine mit Eisen angereicherten Schicht in den ersten Nanometern unterhalb der Oberfläche, jedoch wird keine ausgeprägte Abhängigkeit von der Ionenfluenz festgestellt.

Um die Oberflächensensitivität weiter zu erhöhen, wird eine neue Methode basierend auf der extrem asymmetrischen Röntgenbeugung eingesetzt. Diese erlaubt die Ermittelung kleinster Dichtevariationen infolge des Nachweises kleinster Winkelverschiebungen des gebeugten Röntgenstrahls auf Grund der Brechung des Röntgenstrahls an der Oberfläche. Durch Simulationen mit Hilfe der dynamischen Theorie der Röntgenbeugung wird eine mit steigender Fluenz zunehmende Verringerung der Dichte nahe der Oberfläche nachgewiesen. Daraus wird gefolgert, dass die Massendichte an der Oberfläche unter Einfluss der Musterbildung abnimmt.

In einem zweiten Schritt wird die Ausbildung von Eisen-Siliziden verschiedener Stöchiometrie in der amorphisierten Region nahe der Oberfläche untersucht. Die Kombination von Röntgen-Photoemissions-Spektroskopie und Röntgenabsorptionsspektroskopie mittels Synchrotronstrahlung erlaubt eine tiefenaufgelöste Bestimmung der chemischen Bindungszustände von Si und Fe atomen nahe der Oberfläche. Es wird gezeigt, dass sich nahe der Oberfläche Eisenreiches Silizid (Fe_3Si), in größerer Tiefe nahe der Grenzsschicht zu noch kristallinem Silizium jedoch vermehrt Siliziumreiches $FeSi_2$ Silizid bilded. Dieser Nachweis belegt, dass chemisch gebundenes Eisen eine Vorbedingung zur Musterbildung darstellt. Die gebildeten Phasen mit unterschiedlichem Fe-Si Verhältnis auf glatten und strukturierten Oberflächen entsprechen niedrigen und hohen Ionen Flüssen.

In einem dritten Schritt wird die Rekristallisation dieser Eisensilizide während thermischem Ausheizens bei Temperaturen bis 800°C untersucht. Tiefenaufgelöste Messungen mittels Röntgenbeugung unter streifendem Einfall (GID) belegen, dass sich nahe der Oberfläche ε-FeSi bildet, in größerer Tiefe jedoch β-$FeSi_2$ mit geringerem Fe-Gehalt. Verschiedene gebildeten Phasen mit unterschiedlichen Verhältnis im Fe-Si Schicht auf glatten und strukturierten Oberflächen entsprach niedrige und hohe Ionen Flüssen.

Zuletzt wird die Musterbildung auf Si(001) Oberflächen nach Krypton-Sputtering bei gleichzeitigem Eisen-Eintrag untersucht. Es zeigt sich, dass es auch in diesem Fall nur zu Musterbildung kommt, wenn die Konzentration von Eisenatomen an der Oberfläche einen Schwellenwert überschreitet. Für hohe Eisenkonzentrationen kommt es zur Ausbildung periodischer Ripple-Muster mit einer Anreicherung von Eisen nahe der „Gipfel" der Ripples. Photoelektronen-Spektroskopie und Röntgenabsorptionsspektroskopie zeigen auch hier die Ausbildung von Silizidphasen mit abnehmendem Eisengehalt von der Oberfläche in Richtung auf das Volumen.

Contents

1 **Introduction** **1**

2 **Ion beam induced pattern formation** **5**

2.1 Ion-solid interaction process 5

2.2 Theoretical approaches in surface morphology modulation 7

2.3 Bradley and Harper linear instability model 10

2.4 Patterning by ion bombardment with co-deposition of impurities 11

3 **Surface and interface characterization methods** **13**

3.1 Refraction and reflection of X-rays from interfaces 13

3.2 X-ray diffraction theories 17

3.2.1 Kinematical theory 17

3.2.2 Dynamical theory 23

3.3 Experimental realization 31

3.3.1 Surface sensitive extremely asymmetrical X-ray diffraction 35

3.4 X-ray absorption methods 40

3.4.1 X-ray Photoelectron spectroscopy 42

3.4.2 X-ray absorption spectroscopy 45

3.5 Experimental procedure 51

4 **Pattern formation on direct off-normal Fe ion irradiated Si(100) surfaces** **59**

4.1 Sample preparation 59

4.2 Surface and interface morphology analysis 60

4.3 Depth density profiling of Si(100) after irradiation with Fe ions 69

4.3.1 X-ray reflectivity 69

4.3.2 Extremely asymmetric diffraction with changing scattering geometry 72

4.3.3 Extremely asymmetric diffraction with changing the wavelength 79

5 Near surface silicide formation after Fe ion irradiation of Si(100) surfaces 85

5.1 X-ray photoelectron spectroscopy analysis 85

5.2 X-ray absorption spectroscopy analysis 94

6 Recrystallization of Fe ion irradiated Si(100) 101

6.1 Effect of ion fluence on the phase composition 105

6.1.1 Structural evolution in high-fluence ion irradiated Si upon thermal annealing 105

6.1.2 Structural evolution in low-fluence ion irradiated Si upon thermal annealing 109

6.2 Strain analysis 111

7 Ion beam induced patterning with incorporation of metal atom impurities 115

7.1 Surface patterning using a broad-beam ion source 116

7.2 Surface patterning using a focused-beam ion source 122

8 Summary and conclusions 129

Acknowledgements 131

Bibliography 133

Glossary

The some of the acronyms used herein are presented:

GI-XRD	grazing incidence X-ray diffraction
XRR	X-ray reflectivity
EAD	extremely asymmetric diffraction
RLP	reciprocal lattice point
XPS	X-ray photoelectron spectroscopy
IMFP	inelastic mean free path
BE	binding energy
VB	valence band
FWHM	full width at half maximum
XAS	X-ray absorption spectroscopy
XANES	X-ray absorption near edge spectroscopy
EXAFS	extended X-ray absorption fine structure
AFM	atomic force microscopy
RMS	root mean square
FFT	fast Fourier transform
TEM	transmission electron microscopy
RT	room temperature
STM	scanning tunneling microscopy
RBS	Rutherford back scattering spectroscopy
SIMS	secondary ion mass spectrometry

1 Introduction

The bombardment of solid surfaces with energetic ions can induce a wide variety of surface morphology evolutions that have been the subject of extensive theoretical and experimental studies over the last few decades [1-4]. The experimental studies show that a remarkable variety of self-assembled nanoscale patterns, i.e. periodic height modulations or "ripples", dots and relief pattern can be fabricated in a wide variety of materials, e.g. in elemental and compound semiconductors by varying the experimental parameters such as ion energy, fluence, ion incidence angle and the use of different ion species, e.g. Ar^+, Kr^+, Xe^+ [2].

There is substantial scientific and technological motivation to increase the understanding of the mechanism of surface patterning [5, 6]. This conception becomes difficult due to many active parameters involved in the surface patterning mechanism. The variation of these parameters causes a variation of properties of irradiated materials, e.g. by sputtering yield, surface binding energy, and surface density that can be considered as active factors in the surface patterning process.

Most of the theoretical models describe the pattern formation mechanism as a result of the complex interplay between the processes leading to roughening and smoothing [3-8]. However, identification of these processes is a challenge for theoreticians.

In practice, pattern formation is commonly observed after irradiation of semiconductor surfaces by noble gas ions [7-9]. However, a number of experimental works have shown that the simultaneous co-deposition of foreign atoms, in particular metal atoms like Fe, during noble gas bombardment has tremendous influence on self-organized nanopattern formation and offers a new degree of freedom for pattern control. Besides the experimental evidence for the crucial role of metal atom impurities during the patterning process, theoretical models were developed recently to describe the effect of incorporated impurities on pattern formation [10-14].

The focus of this work is the observation of surface patterning after a direct off-normal irradiation of low energy Fe ions on Si(100) without the assistance of noble gas ions. For adequate modeling of ion-beam induced surface patterning, identification of relevant active parameters are a prerequisite. The aim of this work is to find out and distinguish these parameters affecting the patterning mechanism via monitoring of the near surface area where Fe ions play a

role. For this, ion beam induced surface density variation, and depth resolved tracing of the chemical environment and crystalline structure of distributed Fe within the Si matrix are investigated. Afterward, the obtained results are examined for co-deposited Fe atoms during normal bombardment of Kr ions on Si(001) to study the effect of incorporated Fe atoms on the patterning mechanism.

This work is organized as follows:

In chapter 2, a short review is given on essential theoretical approaches governing the surface evolutions as well as the sputtering phenomena due to the ion-solid interaction process. Additionally, the Bradley-Harper model for ion-beam induced patterning on isotropic surfaces is briefly explained.

In chapter 3, the used X-ray diffraction and absorption techniques are introduced, along with their realization with enhanced surface sensitivity.

In chapter 4, nanopatterning on Si(100) surfaces under an off-normal irradiation process with energetic Fe ions is presented. To find out the ion beam induced variation of surface density, X-ray reflectivity (XRR) and extremely asymmetric diffraction (EAD) methods were carried out.

In chapter 5, Fe-silicides formation in various stoichiometries below the amorphized surface of crystalline Si(100) after irradiation with Fe ions is presented. For this, X-ray photoelectron spectroscopy (XPS) and X-ray absorption spectroscopy (XAS) based on synchrotron radiation were applied.

In chapter 6, the structural transition of formed Fe-silicides from amorphous to crystalline phase during a thermal annealing process is described. The formed phases and their spatial distribution in the Fe-Si layer were observed by grazing incidence X-ray diffraction (GI-XRD) measurements.

In chapter 7, pattern formation on Si(001) surface under normal incident Kr ion bombardment with simultaneous incorporation of metal atoms is reported. The effect of incorporated Fe atoms on patterning processes was investigated using XRR, XPS and XAS methods.

Chapter 8 contains a short summary and conclusion.

List of publications in association with this work:

Most of the results presented in this thesis have been already published or are under review. The following publications and conferences list are in related to this thesis.

B. Khanbabaee, B. Arezki, A. Biermanns, M. Cornejo, D. Hirsch, D. Lützenkirchen-Hecht, F. Frost, and U. Pietsch, *Depth profile investigation of the incorporated iron atoms during Kr+ ion beam sputtering on Si (001).* Thin Solid Films **527**, 349-353 (2013)

B. Khanbabaee, A. Biermanns, S. Facsko, J. Grenzer, and U. Pietsch, *Depth profiling of Fe-implanted Si (100) by means of X-ray reflectivity and extremely asymmetric X-ray diffraction.* Journal of applied crystallography **46**, 505 (2013)

B. Khanbabaee, D. Lützenkirchen-Hecht, S. Facsko, J. Grenzer, and U. Pietsch, *Near surface silicide formation after off-normal Fe-implantation of Si (001).* Journal of applied physics (under review)

B. Khanbabaee, J. Grenzer, S. Facsko, C. Baehtz and U. Pietsch, *Recrystallization of Fe-silicides in the top part of silicon [001]surfaces after oblique irradiation by 20 keV Fe-ions,* Journal of applied physics letters (under submission)

B. Khanbabaee, J. Grenzer, S. Facsko, and U. Pietsch, *Near-surface density profiling of Fe ion irradiated Si (100) using extremely asymmetric diffraction by variation of the wavelength,* Journal of applied physics letters (under submission)

List of attended conferences:

B. Khanbabaee, B. Arezki, A. Biermanns, M. Cornejo, F. Frost, and U. Pietsch, *Depth resolved damage profile created by iron co-sputtering in silicon during ion beam induced pattern formation.* 10th Biennial Conference on High Resolution X-Ray Diffraction and Imaging, (XTOP), 20th-23rd September 2010, University of Warwick (UK)

B. Khanbabaee, A. Biermanns, M. Cornejo, F. Frost, and U. Pietsch, *Investigation of the depth profile of ion beam induced nanopatterns on Si with simultaneous metal incorporation.* 75th Annual Meeting of the DPG and DPG Spring Meeting, 13th -18th of March 2011, Dresden, Germany

B. Khanbabaee, A. Biermanns, S. Fasco, J. Grenzer, and U. Pietsch, *Density and strain profile of Fe implanted Silicon (001) after normal and oblique incidence*. International Symposium on 'NANOSCALE PATTERN FORMATION AT SURFACEES' 18th-22th of September 2011, El Escorial (Madrid), Spain

B. Khanbabaee, B. Arezki, A. Biermanns, M. Cornejo, F. Frost, and U. Pietsch, *X-ray investigation of the depth profile of ion beam induced nanopatterned Si surface after co-sputtering of Kr^{+} and metal ions.* International Symposium on 'NANOSCALE PATTERN FORMATION AT SURFACEES' 18th-22th of September 2011, El Escorial (Madrid), Spain

B. Khanbabaee, S. Fascko, J. Grenzer, and U. Pietsch, *Structure and strain analysis of iron ion implanted Si surface by using Depth dependence X-ray diffraction methods*. 8th Autumn School on X-ray Scattering from Surfaces and Thin Layers, 4th-7th of October 2011, Smolenice Castle, Slovakia

B. Khanbabaee, A. Biermanns, M. Cornejo, F. Frost D. Lützenkirchen-Hecht and U. Pietsch, *Depth profile investigation of the incorporated Fe atoms during Kr ion beam sputtering on Si(001).* 7th DELTA User-Meeting, 30th of November 2011, Dortmund, Germany

B. Khanbabaee **,** A. Biermanns, M. Cornejo, D. Hirsch, F. Frost, and U. Pietsch, *Investigation of the Fe incorporation in ion-beam induced patterning on Si (100).* 76th Annual Meeting of the DPG and DPG Spring Meeting, 25th – 30th of March 2012, Berlin, Germany

B. Khanbabaee, A. Biermanns, S. Facsko, J. Grenzer, and U. Pietsch, *Depth profiling of iron implanted Si (100) using extremely asymmetrical diffraction.* The 11th Biennial Conference on High Resolution X-Ray Diffraction and Imaging (XTOP), 15th-20th of September 2012, Saint-Petersburg, Russia

B. Khanbabaee, S. Facsko, S. Doyle and U. Pietsch, *Depth profile of Fe implanted Si (100) by means of extremely asymmetric X-ray diffraction (EAD).* Fourth ANKA and KNMF User Meeting, 10th-11th of October 2012, Karlsruhe, Germany

B. Khanbabaee, S. Facsko, D. Lützenkirchen-Hecht, and U. Pietsch, *Depth profiling of Fe implanted Si (100) by means of Extended X-ray absorption fine structure and X-ray photoelectron spectroscopy.* 8th DELTA User-Meeting, 28th of November 2012, Dortmund, Germany

B. Khanbabaee, S. Facsko, and U. Pietsch, *Depth-resolved X-ray photoelectron and X-ray absorption spectroscopic study of Fe-implanted Si.* 77th Annual Meeting of the DPG and DPG Spring Meeting, 10th – 15th of March 2013, Regensburg, Germany

B. Khanbabaee, A.Biermanns, S.Facsko, J. Grenzer, and U. Pietsch, *Depth profile investigation of Fe implanted Si (100) by means of extremely asymmetric X-ray diffraction*. International Symposium on Nanoscale Pattern Formation at Surfaces, 26th-30th of May 2013, Copenhagen, Denmark

B. Khanbabaee**,** S. Facsko, J. Grenzer, and U. Pietsch, *Near- surface density profiling in Fe implanted Si (100) by using extremely asymmetric X-ray diffraction*. 9th Autumn School on X-ray Scattering From Surfaces and Thin Layers , 25th-28th of September 2013, Smolenice Castle, Slovakia

B.Khanbabaee, J. Grenzer, S. Facsko, and U. Pietsch, *Structural evolution upon thermal annealing for Fe ion irradiated Si(100).* 78th Annual Meeting of the DPG and DPG Spring Meeting, From 30th of March to 5th of April 2014, Dresden, Germany

2 Ion beam induced pattern formation

It has been established that the sputtering process can modify the surface morphology [15-17]. Systematic studies of sputtered topology started in the early 1950s, and gave evidence that even with an uniform and collimated ion beam, the removal of the atoms from the surface is not uniform but depends on the local topology, composition, crystal structure, and existing defects such as dislocations and impurities. A review of the observed morphologies was published by Carter *et al.* [18]. In section 2.1 of this chapter the sputtering phenomenon caused by the ion-solid interaction process is introduced. In section 2.2, a short review is given concerning essential theoretical approaches governing the surface evolution. In section 2.3, the Bradley-Harper model for ion-beam induced patterning on isotropic surfaces is briefly explained. In the last section 2.4, the effects of co-deposited metal atoms and noble gas atoms during ion bombardment on surfaces evolution are described, recently published by Bradley's advanced theory.

2.1 Ion-solid interaction process

Ion bombardment of a solid surface is the injection of energetic particles in the form of ionized atoms beneath the surface of a material [19]. Upon penetrating the solid, the ion initiates a "collision cascade," a succession of encounters with host atoms, involving atomic ionization and bond-breaking, or nuclear collision in which the ion is scattered elastically and the struck atom recoils. If the recoiling atom receives sufficient energy, it escapes from its local lattice site and migrates, producing its own "cascade," while the original ion continues its own random path. After losing energy to the host via multiple collisions, the ion and the recoil particles eventually come to rest beneath the surface in typically less than 10^{-12} sec [19]. They may occupy pre-existing lattice vacancies, create their own vacancies, or they may lodge interstitially. Since the final result is the deposition of all the energy of the primary ion into the host, this energy will mainly appear as lattice phonons, or heat, in the host.

Sputtering

Surface sputtering loss may appear when occasional recoil atoms in the cascade return to the free surface with enough energy to escape from the host (Fig. 2.1a). In this process, surface atoms are

removed by collisions between the incoming particles and the atoms in the near surface layers of a solid. Whereas most of the sputtered atoms are located at the surface, the scattering events that might lead to sputtering take place within a certain layer of average depth a, which is the average energy deposition depth (usually it is of the order of the incident ion penetration depth) [20].

The yield of the sputtered atoms (the number of sputtered atoms per incident ion) typically falls in the range of 0.5-20, depending on parameters of incident ion beam, experimental geometry and composition of target material. The sputtering yield, Y, for particles incident normal to the surface is expressed by Sigmund as [21]

$$Y = \Omega F_D(E_0) \,, \tag{2.1}$$

where Ω is called a *material factor* containing all material properties, such as surface binding energies. It is a description of the number of recoil atoms that can escape from the solid. In Sigmund's description [21]:

$$\Omega \cong \frac{4.2}{NU_0} (nm\, eV^{-1}) \tag{2.2}$$

where N is the atomic density in $(nm)^{-3}$, and U_0 is the surface binding energy in eV. U_0 can be estimated from the cohesive energy and has typical values between 2 and 4 eV [22]. Values of cohesive energy are given in Kittel [23]. For Si it has a value of 4.6 eV.

$F_D(E_0)$ is the energy deposited per unit length due to the nuclear process at the surface. According to Sigmund's theory, the ion is traveling along the z axis and is deposited at a point $P(x, y, z)$ inside the bulk of material. Its kinetic energy spreads according to Gaussian distribution which is given by:

$$F_D(r) = \frac{E}{(2\pi)^{3/2}} exp\left[-\frac{[z-h_0+a]^2}{2\sigma^2} - \frac{x^2+y^2}{2\mu^2}\right] \tag{2.3}$$

where, P represent a point (x, y, z) in the target, a is the average depth of the deposited energy, σ and μ are the widths of the distribution in directions parallel and perpendicular to the incoming beam, respectively, and h_0 is the height at zero time (see Fig. 2.1b). Deviation of the energy

distribution occurs mainly when $M_1 > M_2$, where M_1 is the mass of the projectile and M_2 is the mass of the target atom [24].

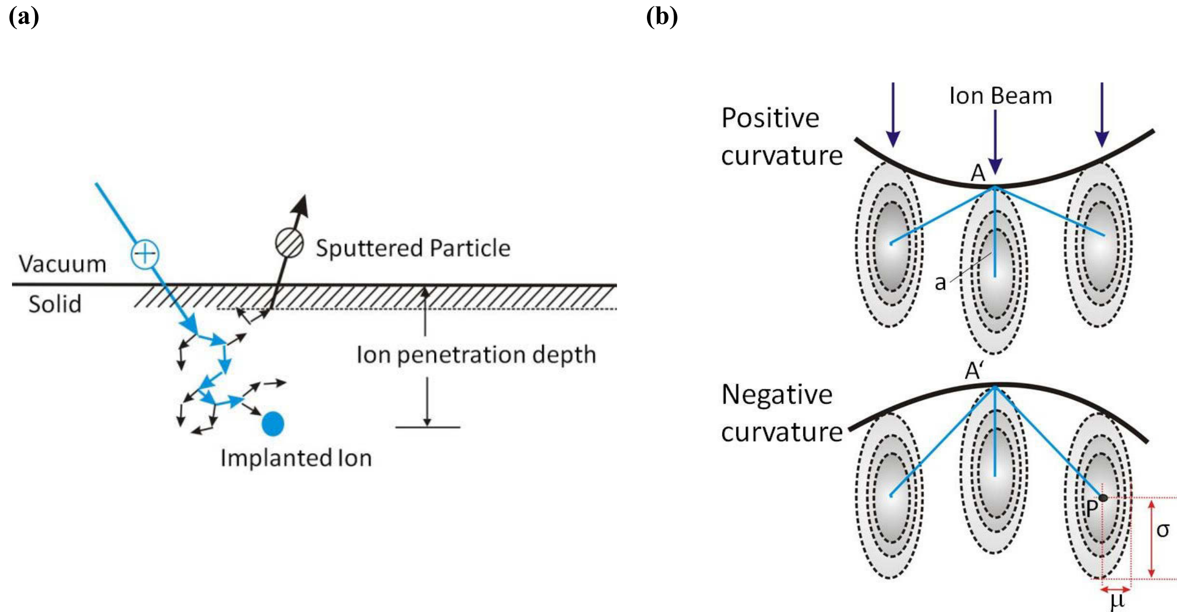

Figure 2.1: (a) schematic of ion-solid interaction and sputtering process. Blue circles: incident ion; blue arrows: random path of incoming ions; black arrows: cascade collision of recoiling atoms; black circle: sputtered atom. (b) Sigmund's theory: The ion penetrates the bulk material and stops at point P, where all its kinetic energy is released and spread out to the neighboring sites following a Gaussian (dashed ellipsoid lines) form with widths σ and μ. Schematic illustration of the physical origin of the BH instability during erosion nonplanar surfaces. A surface element with positive curvature (up) is eroded faster than that with a negative curvature (down), due to the smaller distance (blue lines) that the energy has to travel from the impact point to the surface (A and A´ points).

2.2 Theoretical approaches in surface morphology modulation

During sputtering, the following individual mechanism leading to roughening and smoothing of the surface may contribute to the evolution of the surface. They depend on processing condition or the type of the surface, different mechanism may be more or less active.

Roughening process:

Morphology dependent sputter yield-BH (Bradley-Harper) instability

Bradley and Harper introduced a theoretical approach providing a function that describes the sputtering yield as a function of distance from the point of entry of the primary ion and its angle of incidence. The yield variation with the local surface curvature induces an instability, which leads to the formation of periodically modulated structures. The sputter-induced surface evolution equation can be simplified into a linear partial differential equation [25]:

$$\frac{\partial h}{\partial t} = -\nu_0 + \frac{\partial \nu_0}{\partial \theta}\frac{\partial h}{\partial x} + \nu_x(\theta)\frac{\partial^2 h}{\partial x^2} + \nu_y(\theta)\frac{\partial^2 h}{\partial y^2}, \quad (2.4)$$

where the parameter ν_0 is the average erosion rate of the surface and depends on θ, the angle of ion incidence with respect to surface normal. $\nu_x(\theta)$ and $\nu_y(\theta)$ are the effective surface tensions generated by the erosion process, dependent on the angle of incidence of the ions, θ. The results obtained by BH (i.e., that the local sputter yield is proportional at the surface curvature) means that more energy is deposited on the surface with a positive curvature (bottom of valleys) than at a surface with a negative curvature (top of hills). This makes the former erode faster than the latter one and leads to an unstable behavior; i.e., the lower points on the surface sputter faster than the higher points on the surface [3] (See Fig. 2.1b).

Smoothing processes:

Diffusion on isotropic surface

While sputtering and ion-induced defects cause surface roughness, diffusion of defects on the surface reduces the surface roughness. On an isotropic surface, such as amorphous material, the relaxation is driven by the reduction in total surface area and the minimization of the surface chemical potential which is approximately proportional to the surface curvature ($\frac{\partial^2 h}{\partial x^2}$). The gradients in chemical potential generate a flux of mobile species that decrease the surface

roughness. Under these conditions, Herring and Mullins [26, 27] demonstrated that the rate of surface height variation is proportional to the divergence of the curvature,

$$\frac{\partial h}{\partial t} = -B\nabla^4 h \ , \ \text{ with } \ B = \frac{\gamma D_s C}{n^2 k_B T} \tag{2.5}$$

where γ is the surface energy, D_s is the surface diffusion constant, C is the average concentration of mobile defects on the surface (number per unit area), and n is the number of atoms per unit volume. Eq. 2.5 predicts that perturbation at wave vector k decays with a rate that is proportional to Bk^4.

Radiation induced viscous flow

In addition to surface diffusion, the roughness of the amorphous surface can be reduced by viscous flow. In this case, surface roughness leads to a gradient of local stress inducing a cooperative rearrangement of atoms in the near-surface area. This process can lead to the relaxation of surface corrugation with a relaxation rate that depends on the wave vector of the feature and the viscosity η. The relaxation rate in momentum space can be expressed as [28]:

$$\frac{\partial h}{\partial t} = -h(\boldsymbol{k}, t)\frac{\gamma d^3}{\eta} k^4 \ , \tag{2.6}$$

where, d is the depth of the ion-enhanced viscous layer that equals approximately with the depth of ion. This equation shows the same wave vector dependence as Eq. 2.5, which means that both the surface diffusion and the surface-confined viscous flow produce similar relaxation kinetics.

Ballistic diffusion: Carter Vishnyakov (CV) effect

When an ion enters the bulk, it displaces the target atoms through a series of collision. These ion-induced displacements can be considered as an effective diffusion process, causing a random mixing of target atoms. This radiation-induced diffusivity is commonly used to explain the mixing of different species in the bulk during ion bombardment. Applying these ideas to the surface, Carter and Vishnyakov [15] and Carter *et al.* [29] proposed that some of the surface

atoms can gain enough energy to be displaced transversely along the surface but do not have enough energy to overcome the surface binding energy to be sputtered away. The number of these atomic recoils on the surface can be written as a function of incident angle and surface slope, which results in a curvature-dependent smoothing term [15]. Carter *et al*. showed that the smoothing term induced by ballistic diffusion can counteract the roughening indicted by the curvature-dependent sputter yield (the BH mechanism), especially at normal or near normal ion incidence.

2.3 Bradley and Harper linear instability model

(curvature dependent sputtering and smoothing via thermal diffusion)

Sigmund's theory of description of the ion bombardment is not able to provide direct information about the morphology of ion-sputtered surfaces.

A rather successful model was developed by Bradley and Harper [30]. They combined the curvature dependent erosion velocity with the surface smoothing mechanism due to surface diffusion by Herring/Mullins approach (see above) [31, 32] and derived a linear partial differential equation for surface morphology evolution:

$$\frac{\partial h}{\partial t} = -v_0(\theta) + \frac{\partial v_0}{\partial \theta}\frac{\partial h}{\partial x} + v_x(\theta)\frac{\partial^2 h}{\partial x^2} + v_y(\theta)\frac{\partial^2 h}{\partial y^2} - B\nabla^4 h \tag{2.7}$$

Eq. 2.7 is unstable, with a Fourier mode of k_c because its amplitude grows exponentially and dominates all the others terms. This mode is observed as the periodic ripple structure. Using linear stability analysis, BH derived the ripple wavelength from Eq. 2.7:

$$\lambda_c = 2\pi/k_c\sqrt{\frac{2B}{|\nu|}} \sim (JT)^{-1/2}\exp\left(\frac{-\Delta E}{k_B T}\right), \tag{2.8}$$

where ΔE is the activation energy for surface diffusion, T is temperature and ν is the largest value of the two negative surface tension coefficients, ν_x and ν_y and J is the ion flux.

The importance of the BH model is that the orientation of the pattern depends on the ion beam azimuthal direction and angle of incidence: for small θ the ripples are parallel to the ion

direction, while for large θ they are perpendicular to it. The model also describes how the patterning depends on temperature and flux.

The BH equation is linear, predicting exponential growth of the ripple amplitude. Thus it cannot describe the stabilization of the ripples and kinetic roughening, as observed in experiments. Furthermore, the BH model cannot account for low temperature ripple formation since the only smoothing mechanism is of thermal origin. At low temperature the ion energy and flux dependence of the ripple wavelength also disagree with the BH predictions.

Higher order derivatives in the linear instability model

A modification of the BH model was achieved by Makeev and Barabasi [33] by considering series expansion of Eq. 2.7 to include higher order derivatives. The dominate effect on the periodicity of the pattern is due to the replacement of the smoothing term in Eq. 2.7 by the form

$$-B\nabla^4 h - B_{I,x}\frac{\partial^4 h}{\partial x^4} - B_{I,xy}\frac{\partial^4 h}{\partial x^2 x^2} - B_{I,y}\frac{\partial^4 h}{\partial y^4} \qquad (2.9)$$

The B_I coefficients have an effect on the surface evolution similar to the relaxation by thermal diffusion in Eq. 2.7; for this reason these terms were named ion-induced effective surface diffusion coefficients. However, the coefficients are completely independent of temperature and only describe the interaction of the ion with the surface to reduce the surface height. This affect is called a athermal smoothing.

2.4 Patterning by ion bombardment with co-deposition of impurities

The BH theory [34] predicts that a flat solid surface is unstable for all angles of incidence. Off-normal incidence ion bombardment of silicon, however, does not result in the formation of ripples for values of θ less than a nonzero critical value θ_c that is roughly equal to 45°, contrary to the prediction of the BH theory [35]. This has been attributed to the Carte-Vishnykov effect [35, 36]: momentum transfer from the incident ions to atoms near the surface of the solid produces a surface atomic current [15, 37]. This current has a smoothing effect on the surface of the solid for $< 45°$, but tends to destabilize the surface for larger angles of incidence, according

to a simple theory of the phenomenon. Surprisingly, ripples are found to develop during oblique-incidence ion bombardment of silicon for values of θ as small as 5° or 10° in other experimental work [38, 39]. It is now believed that this is the result of the inadvertent deposition of impurities (metal atoms) during ion bombardment, but how the presence of the impurities led to ripple formation is unclear. Furthermore, a number of experimental results over the past few years show that a solid surface can be destabilized by the deposition of impurities during ion bombardment [40-46]. When a silicon surface is subjected to normal-incidence ion bombardment no pattern formation happens and the surface develops only low-amplitude, long-wavelength height variation characteristic of kinetic roughening. In contrast, if the surface is seeded with molybdenum atoms during bombardment, a disordered array of nanodots emerges [40, 47]. Bradley introduced a theory that accounts for these observations. In his theory, the silicon surface remains flat if it is bombarded in the absence of impurities. When a sufficient flux of metal atoms is incident on the surface, on the other hand, the theory predicts that the surface becomes unstable. In this theory, it is assumed that nearly all of the metal atoms on the surface are immobilized [48].

3 Surface and interface characterization methods

In the case of low energy ion beam bombardment, the penetration depth of the implanted ions and hence the ion induced damage in the host lattice are limited to a depth of a few nanometers. Therefore, surface sensitive methods are needed for the investigation of the surface and the near surface region. The used characterization techniques and their realization with enhanced surface sensitivity are presented in this chapter as follows: in section 3.1 the basic theory of X-ray reflectivity method; in section 3.2 kinematical and dynamical theories of X-ray diffraction in crystalline material; in section 3.3 the realization of X-ray scattering methods for this work; in section 3.4 the theory and realization of absorption methods as chemical characterization techniques, and finally in section 3.5 experimental setups of applied techniques are presented.

3.1 Refraction and reflection of X-rays from interfaces

In this section, X-ray reflectivity is described in terms of wave optics. It is shown that a light reflects from surface according to the Fresnel formula and the reflectivity of a surface with arbitrary density profiles may be calculated using the slicing method via the Parratt formalism. This approach is also applicable for X-rays.

Basic principles

The specular reflection of X-rays is accurately described by Fresnel's equation in conjunction with the proper refractive index, which is given for hard X-rays and away from absorption edges by [49]:

$$n(r) = 1 - \delta(r) + i\beta(r) \quad \text{with} \quad \delta = \frac{\lambda^2}{2\pi} r_e \rho \quad \text{and} \quad \beta = \frac{\lambda}{4\pi}\mu \tag{3.1}$$

where $r_e = 2.818 \times 10^{-15}\ m$ denotes the classical electron radius; λ is the X-ray wavelength; ρ is the electron density of the material and μ is the linear absorption coefficient. The mass density is given by $\rho_m = \rho A / N_A Z$ (A is the mass number and N_A is Avogadro's constant and Z is the atomic number). The values of $\delta \sim 10^{-6}$ for X-rays, i.e. the real part of the refractive index are slightly smaller than unity. The absorption β is usually one or two order of magnitude smaller.

For single vacuum/medium interface the *Snell's law* of refraction by neglecting the absorption term β is given by:

$$cos\ \alpha_i = (1 - \delta)\ cos\ \alpha_t \tag{3.2}$$

where α_i and α_t are the incidence and refracted angles with respect to the surface (Fig. 3.1a). This implies that below a certain incident grazing angle, X-rays undergo total external reflection in air. This angle is called *critical angle,* α_c, and is given by [49] :

$$\alpha_c \approx \sqrt{2\delta} = \lambda \sqrt{r_e \rho / \pi} \tag{3.3}$$

Reflectivity parameters of silicon at $\lambda = 1.54$ Å ($CuK\alpha$ radiation) are listed in table 3.1

Table 3.1. Electron density, ρ, mass density, ρ_m, dispersion, δ, linear absorption coefficient, µ, critical angle, α_c, critical wavevector, Q_c, of silicon for X-rays at λ = 1.54 Å [22, 50, 51].

Atomic number (Z)	Atomic weight (amu)	Atomic density ($atoms\ cm^{-3}$)	Mass density ($g\ cm^{-3}$)	Electron density (e^- Å^{-3})	Lattice constant (Å)	$\delta \times 10^6$	$\mu \times 10^6$ (Å^{-1})	α_c (°)	Q_c (Å^{-1})
14	28.0855	5×10^{22}	2.33	0.699	5.43	7.6	1.399	0.22	0.032

Reflectivity in single surface

If a plane electromagnetic wave $E_i(\boldsymbol{r}) = Ae^{i\boldsymbol{k_i}\cdot\boldsymbol{r}}$ with wavevector $\boldsymbol{k_i}$, hits a flat surface of a medium at grazing angle α_i, the reflected and transmitted field may be described by $E_r(\boldsymbol{r}) = Be^{i\boldsymbol{k_f}\cdot\boldsymbol{r}}$and $E_t(\boldsymbol{r}) = Ce^{i\boldsymbol{k_t}\cdot\boldsymbol{r}}$ with reflected wavevector $\boldsymbol{k_f}$ and transmitted wavevector $\boldsymbol{k_t}$, respectively (see Fig. 3.1a). From the boundary condition one obtains the well-known Fresnel formula to determine the reflection and transmission coefficients $r_s = \frac{B}{A}$ and $t_s = \frac{C}{A}$ [52]. The intensity $R_F = |r_s|^2$ of the reflected X-ray wave is given by (*Fresnel reflectivity*):

$$R_F = \frac{(\alpha_i - p_+)^2 + p_-^2}{(\alpha_i + p_+)^2 + p_-^2}, \tag{3.4}$$

where for small angles the real and imaginary part of the transmission angle $\alpha_t = p_+ + ip_-$ can be approximated by,

$$p_{+,-}^2 \approx \frac{1}{2}\left\{\sqrt{(\alpha_i^2 - \alpha_c^2)^2 + 4\beta^2} \pm (\alpha_i^2 - \alpha_c^2)\right\} \tag{3.5}$$

For $\alpha_i > 3\alpha_c$, an expansion of Eq. (3.4) shows that the Fresnel reflectivity may be well approximated by $R_F \cong (\alpha_c/2\alpha_i)^4$.

If $\alpha_i \leq \alpha_c$, p_- is larger and the transmitted wave propagates parallel to the interface and is called as *evanescent wave* and its amplitude decays exponentially into the material. The penetration depth Λ of this wave is given as [50]:

$$\Lambda = \frac{1}{kp_-} = \frac{\lambda}{\sqrt{2}\pi}\left\{\sqrt{(\alpha_i^2 - \alpha_c^2)^2 + 4\beta^2} - (\alpha_i^2 - \alpha_c^2)\right\}^{-1/2} \tag{3.6}$$

If $\alpha_i \to 0$ the penetration depth tends to $\Lambda_0 = \frac{\lambda}{2\pi\alpha_c} = \frac{1}{\sqrt{4\pi r_0 \rho}}$ independently from wavelength. For most of the materials this penetration depth is around few nanometers, showing that in the region of very small incident angles the scattering mainly is generated from the near-surface region. This fact is extensively used in the so-called extremely asymmetrical diffraction technique (section 3.3.1), where the Bragg diffraction is combined with the surface sensitivity in the region of critical angle [53-55]. For $\alpha_i > \alpha_c$ the penetration depth Λ rapidly increases towards a maximum value of $\Lambda_{\max} = \frac{\lambda}{4\beta} \sim 10 - 100\ \mu m$ for most materials [50].

Reflectivity in multiple interfaces

For practical application the case of stratified media is much more important than of a single surface. In most cases, layer system is applied where the scattering from all interfaces has to be taken into account. Fig. 3.1b schematically shows a multilayer stack consisting of N interfaces at the positions $z_j \leq 0$.

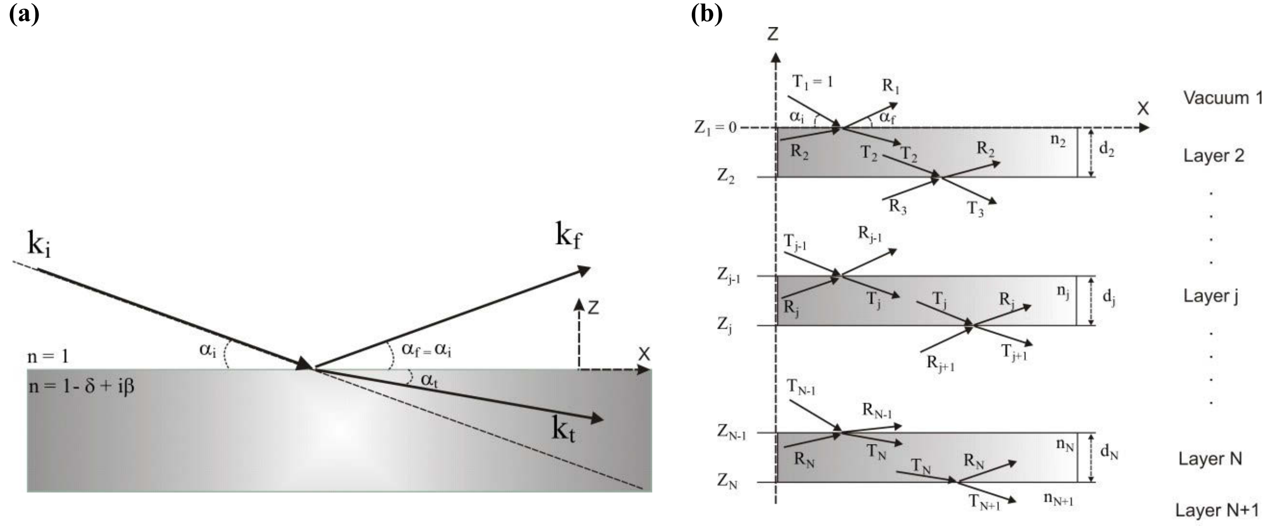

Figure 3.1: (a) A plane electromagnetic wave with wavevector k_i hitting the surface at a grazing angle α_i and splits into a reflected wave with wavevector k_f at angle of α_f and a refracted wave with wavevector k_t transmitted at the angle α_t. (b) Sketch of a system consisting of $N + 1$ layer with N interfaces. The vacuums counts as "layer 1" with the first interface at $z_i = 0$ and the last interface located at z_N with the underlying semi-infinite substrate counts as "layer $N + 1$". The incident wave with normalized amplitude to unity, $T_1 = 1$, hits the surface at the grazing angle α_i. No wave is reflected from the substrate. i.e. $R_{N+1} = 0$. The refractive index of each layer, with thickness $d_j = z_{j-1} - z_j$, is denoted by $n_j = 1 - \delta_j + i\,\beta_j$. $k_{t,j}$ and T_j are the wavevector and the amplitude of the transmitted wave and $k_{f,j}$ and R_j are the corresponding value for the reflected wave inside layer j.

The dynamical calculation of reflected intensity was given by Abeles [56], who introduced a transfer matrix for each layer, which connects the fields at interface j with those at interface $j + 1$, thus yielding the reflected amplitude R_1 after N matrix multiplications [56, 57]. Equivalent to this formalism it is a recursive approach first described by Parratt [58]. If X_{j+1} denoted the ratio of R_{j+1} and T_{j+1} in layer j+1, then X_j for the layer above may be calculated via:

$$X_j = \frac{R_j}{T_j} = \exp\left(-2i\, k_{z,j}\, z_j\right) \frac{r_{j,j+1} + X_{j+1} \exp(2i\, k_{z,j+1}\, Xz_j)}{1 + r_{j,j+1}\, X_{j+1} \exp(2i\, k_{z,j+1}\, Xz_j)} \tag{3.7}$$

where $r_{j,j+1} = \frac{k_{z,j} - k_{z,j+1}}{k_{z,j} + k_{z,j+1}}$ (3.8)

is the Fresnel coefficient of interface j with $k_{z,j} = k\,(n_j^2 - cos^2\,\alpha_i)^{1/2}$ being the z component of the wavevector in layer j. In general substrate is much thicker than the penetration depth of X-ray; consequently there is no reflection from the substrate. i.e. one can set $R_{N+1} = X_{N+1} = 0$ as the start of the recursion. The specularly reflected intensity R is obtained from Eq. (3.7) after N iterations:

$$R = |X_1|^2 = |R_1|^2 \tag{3.9}$$

In practice, surface and interface are always rough and interface roughness has to be included in the calculation of the reflectivity of a layer system. The roughness (σ) damps the specularly reflected intensity. Later, Nevot and Corce [59] show that roughness damps the specularly reflectivity by a factor $\exp(-2k_{z,1}k_{z,2}\sigma^2)$ where $k_{z,1}$ and $k_{z,2}$ are the z component of wavevector inside the vacuum and medium, respectively.

3.2 X-ray diffraction theories

The X-ray diffraction theory is described by two approaches, the so-called kinematical and dynamical theories. The kinematical approach is valid in the so-called ”weak-scattering” i.e. when the cross section for the scattered radiation is small, and hence multiple-scattering effects can be neglected. A very thin crystal is an example of weak scattering. Kinematical approximation breaks down in the region of the critical angle of total external reflection (α_c) where “multiple-scattering” is pronounced. It is valid for incident angles $\alpha_i > 3\alpha_c$, since the reflected intensity rapidly decreases for $\alpha_i > \alpha_c$. When the scattering is strong, for example for the diffracted intensities and rocking curve widths of near-perfect crystals, dynamical theory is used for characterization research.

3.2.1 Kinematical theory

The structure factor

When a plane wave strikes a three-dimensional atomic lattice, each scattering point (electron or nuclear particle) acts as a source of spherical waves. The addition of the amplitudes of all these

waves results in almost zero intensity in most directions but strong beams in some directions when the wavelength of the wave is comparable with the spacing of the scattering centers. This is the phenomenon of diffraction. The most useful description of crystal diffraction was obtained by Bragg [60]:

$$n\lambda = 2d_{hkl}sin\theta_{hkl} \qquad (3.10)$$

where n is an integer representing the order of diffraction, λ is the wavelength, d the interplanar spacing of reflecting plane and θ the angle of incidence and of diffraction of the radiation relative to the reflecting plane (Fig. 3.2a). The diffraction for a given plane does not take place over the zero angular range defined by the Bragg law, but over a small finite range. This range, called the *rocking curve* width, varies tremendously and it governs the strain sensitivity of the technique. The intensity of the diffracted beam depends on upon the strength of the scattering that the material constrains upon the radiation. The basic scattering unit of a crystal is its *unit cell*, and we may calculate the scattering at any angle by multiplying

The scattering strength of an electron or nucleus

The scattering strength of an atom

The scattering strength of unit cell

The scattering strength of the total number of unit cells,

all with regard to the direction of scattering and the relative phase of the scattered waves.

Electron, and atomic scattering factors are tabulated for X-rays [61]. The angular dependence of the intensity is represented by calculating the scattering strength of the unit cell for a particular lattice plane reflection, hkl, wavelength and crystal structure. This fundamental quantity is called *structure factor* F_{hkl}, and calculated as follows:

Waves of vector $\boldsymbol{k}$ scattered from two separated points in the unit cell by a vector $\boldsymbol{r}$ (Fig. 3.2b), will have a phase difference of:

$$exp\{-2\pi i\boldsymbol{k}.\boldsymbol{r}\} = exp\{-2\pi i(hu + kv + lw)\} \tag{3.11}$$

for hkl reflection, where (uvw) are the fractional coordinates of the vector $\boldsymbol{r}$. The structure factor is obtained by adding up of scattered waves from each atom with regard to the atomic scattering factor of each atom and the phase of the wave from each atom over the unit cell:

$$F_{hkl} = \sum_{\mathrm{i}} f_i exp\{-2\pi i(hu + kv + lw)\} \tag{3.12}$$

where f_i are the atomic scattering factors of the atoms of type i. These depends upon both θ and λ. The phases may cause the waves to add (for example Si 004) or cancel (for example Si 002).

(a) **(b)**

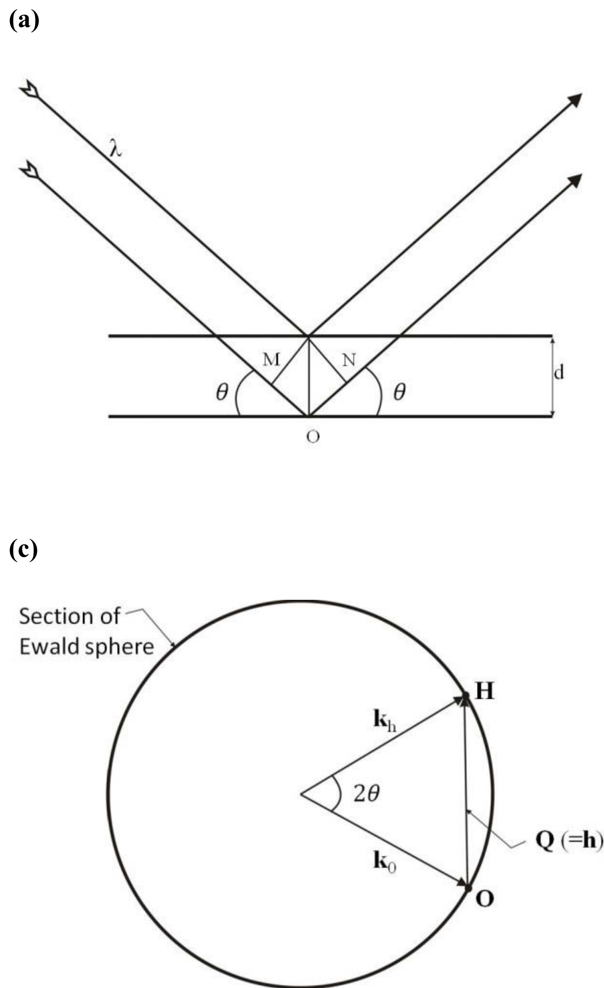

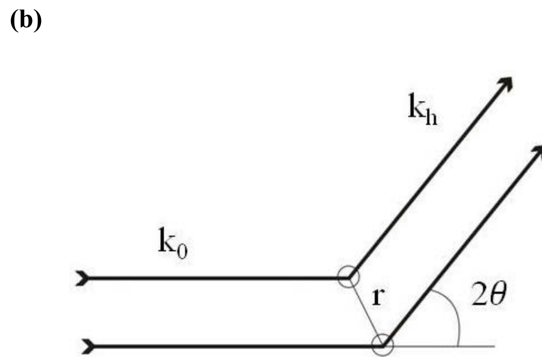

Figure 3.2: (a) Diffraction of a plane wave from crystal planes. Strong diffraction happens when the angles of incidence and diffraction, θ, are equal and the path difference MON between the two beams is equal to $n\lambda$, an integral number of wavelength. Hence the Bragg law, $n\lambda = 2dsin\theta$. (b) The addition of waves scattered by an angle 2θ from an atom at the origin and one at a vector **r** from the origin. The wavevectors $\boldsymbol{k_0}$ and $\boldsymbol{k_h}$ are in the directions of the incident and diffracted beams, respectively, and $|\boldsymbol{k_0}| = |\boldsymbol{k_h}| = 2\pi/\lambda$. (c) The Ewald sphere construction in reciprocal space. The vector relationship between the incident beam vector $\boldsymbol{k_0}$, the scattered beam vector $\boldsymbol{k_h}$, and the scattering vector $\boldsymbol{Q}$.

Atomic scattering factor

The atomic scattering factor f_i are calculated in terms of the scattering of an individual free electron which is considered as a classical oscillator (the assumption is that the electron is a free charged particle). This is termed *elastic or Thomson scattering* in which forced oscillator by the radiation field of an incident X-ray re-radiates in all direction at the same frequency as the incident wave frequency. For an X-ray beam, the intensity I scattered by one electron through an angle 2θ relative to the incident intensity I_0 is

$$\frac{I}{I_0} = \frac{C^2 r_e^2}{R^2} \tag{3.13}$$

where R is the distance of observation from the particle and r_e is classical electron radius. The polarization factor $C = 1$ if the electric vector of the X-ray wave is perpendicular to the dispersion plane; this is known as σ polarization. For π polarization, in which the electric vector is parallel to the dispersion plane, $C = cos2\theta$. For an individual electron, the angular variation of the scattering only arises through this polarization term. The atomic scattering factor is obtained by adding the scattering of electrons with regard to phase in similar equation for the structure factor, but since the distribution of electrons is continues we express it as an integral rather than a summation.

$$f_i = \int_{space} \rho(r) \exp(2\pi i \boldsymbol{Q}.\boldsymbol{r})\, dV \tag{3.14}$$

The scattering vector $\boldsymbol{Q} = \boldsymbol{k_h} - \boldsymbol{k_0}$, where $\boldsymbol{k_0}$ is incident beam vector and $\boldsymbol{k_h}$ the scattered beam vector (Fig. 3.2c). Q is given by

$$Q = \frac{2\pi}{\lambda} sin\theta \tag{3.15}$$

$\rho(r)dV$ is the probability that an electron lies in a volume element dV of the atom at a radial distance r from the nucleus. $\rho(r)$ is the electron probability density and is a meaningful and measurable quantity. The scattered amplitude is therefore the Fourier transform of the electron density. The wavelength and angular dependence of atomic scattering factor is given via $\boldsymbol{Q}$.

The strengths of X-ray reflections

Based on kinematical theory the scattering intensity increases monotonically with the structure factor [62]. The structure factors of reflections in different cubic structure are shown in table 3.2. The intensity formula always contain the modulus of the structure factor $|F_h| = \sqrt{F_h F_{h^*}} = \sqrt{F_h F_{\bar{h}}}$ (or its equivalent in susceptibility, e.g. $\sqrt{\chi_h \chi_{\bar{h}}}$), and also $1/V$, where V is the volume of

the unit cell. The modulus formulas are given for Si in table 3.2. A number of values are zero, referring as forbidden reflections.

Table 3.2. Values of $|F_{hkl}|$ for a number of reflections in cubic structures, with examples of $|F_{hkl}|/V$ in electron units per Å^3 for Si [62].

Reflection	001	002	004	111	222	333	011	022	044	112	224	113	115
fcc	0	4f	4f	4f	4f	4f	0	4f	4f	0	4f	4f	4f
Diamond cubic	0	0	8f	5.66f	0	5.66f	0	8f	8f	0	8f	5.66f	5.66f
Si	0	0	0.39	0.38	0	0.24	0	0.45	0.31	0	0.35	0.30	0.24

To obtain the scattered intensity, we add up the scattering from each unit cell in the same way that we added up the scattering from each atom to obtain the structure factor, or the scattering power of the unit cell. The phase difference $\boldsymbol{r_i}.\boldsymbol{Q}$ between scattered from unit cells located at different r_i from the origin, results in an interference function J, describing the interference of waves scattered from all the unit cells in the crystal, where

$$J = \sum_i exp(2\pi i \boldsymbol{r_i}.\boldsymbol{Q}) \quad (3.16)$$

The summation is taken over all unit cells in the crystal. The overall scattering amplitude is given by $A = F_{hkl}J$ and the intensity I by the square of the amplitude

$$I = F_{khl}^2 J^2 \quad (3.17)$$

Reciprocal space geometry

Since we have elastic scattering, it is always true that the magnification of $\boldsymbol{k_0}$ and $\boldsymbol{k_h}$ are both $1/\lambda$. A sphere of radius $1/\lambda$ can therefore define all the possible incident and scattered beam vectors. The incident beam vector runs from the center of this *Ewald sphere* to the origin, the scattered beam vector runs from the center to any point on the surface of the sphere, and the

scattering vectors runs from the origin to the end of scattered beam vector. Fig. 3.2c shows a two dimensional section of this three-dimensional construction. In this figure the scattering vector $\boldsymbol{Q}$ has been made to coincide with a vector $\boldsymbol{h}$ (where $|h| = 1/d_{hkl}$, d_{hkl} is the spacing of a plane with Miller indices hkl, and the direction of h is perpendicular to the (hkl) plans) that satisfies the Bragg's law and we expect strong diffraction. Many reflections are possible from a regular lattice, and if the set of vectors such as $\boldsymbol{h}$ is represented then we can graphically visualize all the reflecting planes and consequent reflected directions in the crystal. The general formula for the reciprocal lattice space axes, $\boldsymbol{a_1^*}$, $\boldsymbol{a_2^*}$ and $\boldsymbol{a_3^*}$ in terms of the real-space axes $\boldsymbol{a_1}$, $\boldsymbol{a_2}$, $\boldsymbol{a_3}$ are [62]:

$$\boldsymbol{a_1^*} = \frac{\boldsymbol{a_2 \times a_3}}{\boldsymbol{a_1 \cdot [a_2 \times a_3]}} \quad , \quad \boldsymbol{a_2^*} = \frac{\boldsymbol{a_3 \times a_1}}{\boldsymbol{a_2 \cdot [a_3 \times a_1]}} \quad , \quad \boldsymbol{a_3^*} = \frac{\boldsymbol{a_1 \times a_2}}{\boldsymbol{a_3 \cdot [a_1 \times a_2]}} \tag{3.18}$$

3.2.2 Dynamical theory

Limitation of the kinematical theory

Darwin was the first to point out that the kinematical theory violated the conservation of energy. According to this theory, the integrated intensity diffracted by a small crystal is proportional to its volume. The reason is that it was assumed that the amplitude of the wave received by every diffracting center in the crystal is the same, thus neglecting interaction of the wave with matter and the fact that part of its energy has already been reflected away by the layer it has crossed before. This theory works quite well for the diffracted intensities from thin crystals because the interaction of X-ray with matters is very weak but it will be seriously awry for strong scattering. In addition, kinematic theory does not include refraction of X-ray at air-sample surface.

Ewald's dynamic theory

Ewald considers the interaction of X-ray with a crystal as that of electromagnetic field with a three-dimensional array of dipole. Under influence of the incoming field, each dipole radiates a spherical wave $E\exp(2\pi i\nu t - kr)/r$ which propagates with the velocity of light $c = \nu/k$ [63]. This excitation of the dipoles propagates from one dipole to the other as a progressive wave of

phase velocity $v = c/n$. It is the *optical field*. The optical field which propagates through the crystal and excites the dipoles is a sum of plane waves whose wavevectors can be deduced from one another by translation in reciprocal space.

The aim of theory is to find the possible wavevectors and the possible values of the index of refraction of the waves propagating in the crystal, as well as theirs amplitudes. Ewald introduce the boundaries and determined the wavefields generated by incident beam. The incident beam generates two wavefields for each direction of polarization (double refraction). These wavefields propagate inside the crystal along two different directions of propagation which are respectively parallel to the normal to the surface of dispersion at the two corresponding tiepoints. Their tiepoint are situated on different branch of the dispersion surface in transmit ion geometry (Laue) and on the same branch in the reflection geometry (Bragg).

Laue's dynamical theory

Laue's theory is based on the assumption that the distribution of the dielectric susceptibility, or polarization, of the medium for X-ray can be considered as continuous throughout the whole volume of the crystal and proportional to the electron density. In effect, it is the whole unit cell which contributes to the diffracted intensities through its Fourier coefficients and not singular points. When an electromagnetic wave $E(r)\exp(2\pi i v t)$ propagates in a material, the medium is polarized under the influence of the electric field $= \boldsymbol{D}/\epsilon$, where $\epsilon = \epsilon_0(1+\chi)$ varies with the space coordinates. In order to find out the generated waves inside and outside a crystal, **H** and **B** are eliminating in Maxwell's equations:

$$\nabla \times \boldsymbol{H} = \frac{1}{c}\frac{\partial \boldsymbol{D}}{\partial t} \text{ and } \nabla \times \boldsymbol{E} = -\frac{1}{c}\frac{\partial \boldsymbol{B}}{\partial t} \tag{3.19}$$

where $\boldsymbol{E}$ is the electric field, $\boldsymbol{B}$ the magnetic induction, $\boldsymbol{D}$ the electric flux density, $\boldsymbol{H}$ the magnetic field and c the velocity of light in vacuum. A sufficient model for X-ray scattering from a crystal is Fourier sum of either the electron density or the electric susceptibility over all the reciprocal lattice vector $\boldsymbol{h}$. Thus the crystal is represented as [62]:

$$\chi(r) = \sum_h \chi_h \exp(-2\pi i \boldsymbol{h}.\boldsymbol{r}) \tag{3.20}$$

The coefficient of Fourier expansion of hkl reflection, χ_h, is related to the structure factor F_h by

$$\chi_h = -\frac{r_e\lambda^2}{\pi V}F_h \tag{3.21}$$

where V is the volume of the unit cell over which the structure factors is calculated (For Si, $F_h = 7.526047 \times 10^6\chi_h$ at $Cu\,K\alpha$ radiation). By substituting in the Maxwell equation and eliminating the magnetic component, the equation of propagation of an electromagnetic wave in the crystalline medium is obtained:

$$\nabla \times \nabla \times \boldsymbol{D} = -\frac{(1+\chi)}{c^2}\frac{\partial^2 \boldsymbol{D}}{\partial t^2} \tag{3.22}$$

The solution should be a plane wave, or sum of the plane waves. The capital $\boldsymbol{K_0}$ and $\boldsymbol{K_h}$ are used as wavevectors inside the crystal to distinguish them from $\boldsymbol{k_0}$ and $\boldsymbol{k_h}$ outside the crystal. Inside the crystal the allowed wavevectors should satisfy conservation of momentum, that is:

$$\boldsymbol{K_0} + \boldsymbol{h} = \boldsymbol{K_h} \tag{3.23}$$

This Laue condition is a little less restrictive than the Bragg law, in that we no longer have the condition of $|K_0| = |K_h| = 1/\lambda$. Ewald proposed and Bloch showed that waves that exist in a crystal must have the periodicity of the lattice, that is, the solutions look like

$$D = \sum_h D_h \exp(-2\pi i\boldsymbol{K_h}.\boldsymbol{r}) \tag{3.24}$$

Considering the case that two beams are much stronger than others where these two beams are the diffracted and forward-diffracted beam (the incident beam is not a transmitting unchanged through the crystal, anymore), the solution of the Maxwell equations inside the crystal can be expressed in terms of amplitudes D_0 and D_h of these two beams [64]. In order to express the solution simply, two deviation parameters α_0 and α_h are introduced. These express the deviation of the incident and diffracted wavevectors from kinematical assumption where $|k_0|$=$|k_h|$=1/λ, and are defined as

$$\alpha_0 = 1/2k[K_0.K_0 - k^2(1+\chi_0)] \tag{3.25}$$

$$\alpha_h = 1/2k[K_h.K_h - k^2(1+\chi_0)] \tag{3.26}$$

The *deviation parameter* defines the local refractive index of the crystal. The solution may now be expressed in terms of the relationship between the deviation parameters as [62]:

$$\alpha_0\alpha_h = k^2\chi_h\chi_{\bar{h}}/4 \tag{3.27}$$

where $\chi_{\bar{h}}$ is the coefficient of Fourier expansion of $\bar{h}\bar{k}\bar{l}$ reflection. This equation defines the geometry of diffraction. The amplitude ratio may also be expressed in terms of the deviation parameters as:

$$\left(\frac{D_h}{D_0}\right)^2 = \frac{\alpha_0\chi_h}{\alpha_h\chi_{\bar{h}}} \tag{3.28}$$

These are fundamental equations of two-beam dynamical theory, which allow us to predict the wavefields and their intensities inside and outside the crystal. These equations can be interpreted visually using dispersion space diagram.

Introduction of dispersion surface

The wave satisfying the Eq. 3.27 may exist inside the crystal for a given incident beam wavelength, λ. Since this equation relates wavevectors to the local refractive index, it is a dispersion relationship. The diagram of all allowed wavevectors is therefore called a dispersion surface [63]. For an infinite and perfectly periodic crystal, the locus of wavevectors (the reflection domain) would be represented in reciprocal space by a single point locating in the center of the Ewald sphere and is called *Laue point* (L_a). It is situated on the intersection of the two spheres centered at the reciprocal lattice nodes O and H and with radii $k = 1/\lambda$ (dashed circles in Fig. 3.3a). The wavevector inside the crystal can be corrected by multiplying by the mean refractive index, $nk = (1+\frac{\chi}{2})k$. As χ is negative (see Eq. 3.21), the wavevector inside the crystal is shorter than in vacuum. Thus, the point representing the reflection domain in reciprocal

space sits on the intersection of two spheres with the same centers, but with $\left(1+\frac{\chi}{2}\right)k$ as radius (solid circles in Fig. 3.3a). This point is called *Lorentz point* (L_o).

According to Eq. 3.27, the deviation parameters, which are measured perpendicularly from tangents of two spheres centered on O and H, can only be zero when the susceptibility be zero. In real cases, there must be deviation and its form is a hyperbola (red curves in Fig 3.3b). When diffraction occurs a point lying on circles centered on O and H do not represent the solutions of Maxwell's equation because there will be one wave propagating in the crystal. Once it lies on the connecting surface (p in Fig 3.3b), there are two waves and both wavevectors differ slightly from nk. This surface is called *dispersion surface* [63].

The dispersion surface has two branches. Waves from the two branches are in antiphase relation. This affects their absorption causing to asymmetry in shape of rocking curves. Any point on either branch of the dispersion surface is an equally good solution of the Maxwell equations. Which of the allowed points are selected depends on the incident angle and the boundary conditions.

According to Eq. 3.28, the diffracted beam intensity will be a maximum when $\alpha_0 = \alpha_h$, at the center of the dispersion surface. The angular width of the reflection domain is represented in reciprocal space by the size of this connecting surface between the two spheres. The diameter of the dispersion surface is approximately $\chi_h k$, and thus increases with the structure factor, which is directly proportional to the width of the rocking curve of the crystal (see Eq. 3.31). Therefore, the larger structure factor, the stronger is the interaction and the larger is the reflection domain. For an infinitely weak reflection, the dispersion surface would be concentrated at the Lorenz point; this would correspond to an 'empty' crystal. The distance of the Lorentz point to the dispersion surface, $|C|\sqrt{\chi_h \chi_{\bar{h}}}/2cos\theta_B$, is shorter than the distance of the Lorenz point to the Laue point, $k|\chi_0|/2cos\theta_B$.

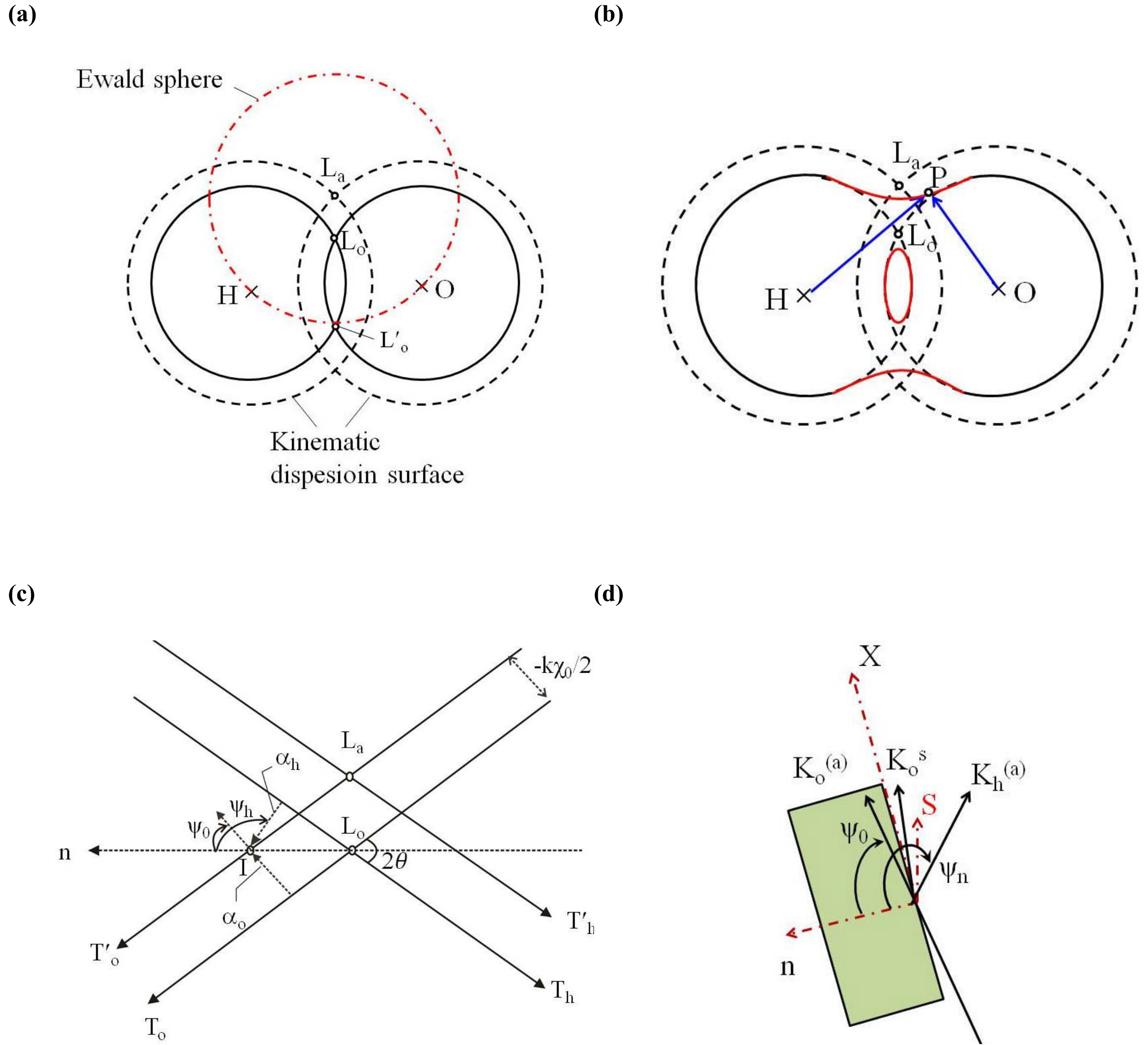

Figure 3.3: (a) Influence of the index refraction. L_o: Lorenz point; $\overline{OL_o} = \overline{HL_o} = nk$, where n is the index of refraction; L_a :Laue point; L_0 and $L_o^{'}$: Lorenz points associated with the reciprocal lattice vector $\boldsymbol{OH} = \boldsymbol{h}$ and $\boldsymbol{HO} = -\boldsymbol{h}$ **,** respectively. (b) Intersection of the refracted (**OP**) and reflected (**HP**) waves. Solid red curve: dispersion surface; P: tiepoint. (C) Deviation from Bragg's angle of the middle of the reflection domain in reflection geometry: I is the excitation point of the wave corresponding to the middle of the reflection domain; it differs from the position given by the kinematical theory, L_a , by $\Delta\theta = \frac{\overline{L_a I}}{k}$; $T_o^{'}$, $T_h^{'}$:tangents to the sphere of centers O and H and of radius k; α_0 and α_h: the distance from I to T_0 and T_h; The distance between T_0 and $T_0^{'}$ (and between T_h and $T_h^{'}$) is $-k\chi_0/2$. (d) Reflection geometry in direct space. $\boldsymbol{k_o^{(a)}}$**:** Incident wavevector; $\boldsymbol{k_o^{(s)}}$**:** specularly reflected off the crystal surface; $\boldsymbol{k_h^{(a)}}$**:** diffracted wavevector; $\boldsymbol{n}$: normal to the crystal surface oriented towards the inside of the crystal; S: parallel to the lattice plane; ψ_0, ψ_n: angles between n and the incident direction and reflected direction.

Advanced dynamical theory

Deviation from Bragg's incidence of the middle of the reflection domain,

The angular position of the center of the reflection domain differs from that given by Bragg's law. This is due to the fact that the effect of refraction is neglected in the kinematic theory. The angle between corresponding directions is called the *deviation from Bragg's angle of the middle of the reflection domain* and is related to the index of refraction. Making approximation that the spheres of centers O and H and with radii k can be approximated by their tangents $T_o^{'}$ and $T_h^{'}$ and with radii $(1+\frac{\chi}{2})k$ can be approximated by their tangents T_0 and T_h (Fig. 3.3c), the deviation from Bragg's angle can be determined as:

$$\Delta\theta = \frac{\overline{L_a I}}{k} = -\frac{\chi_0(1-\gamma)}{2sin2\theta_B} \quad (3.29)$$

where $\gamma = \frac{\gamma_h}{\gamma_0}$ is the asymmetry ration with $\gamma_0 = cos\psi_0 = sin\alpha_i$ and $\gamma_h = cos\,\psi_n$ in which ψ_0 and ψ_n are the angles between surface normal oriented towers inside the crystal and incident direction and reflected direction, respectively. Incidence angle $\alpha_i = 90 - \psi_0$ is the angle between the incident direction and crystal surface. In the Bragg geometry, γ is negative and there is always a deviation from Bragg's angle, even for a symmetric reflection. The reflection geometry in real space is shown in Fig. 3.3d. The reflected wave is directed towards the outside of the crystal. The normal to the crystal surface (n) intersects one branch of the dispersion surface at a time.

Dynamical approach in highly asymmetric coplanar and non-coplanar geometries

In extremely asymmetry diffraction condition, it is possible to reduce drastically the penetration depth, in particular for angles of incidence close to the critical angle for specular reflection (α_c). There are two geometries for reducing the penetration depth: non-coplanar and coplanar. In both geometries, the spheres of centers O and H cannot approximated by their tangential planes because deviation from Bragg's angle according to Eq. 3.29 tends towards infinity when the

glancing angle tends towards zero, which is physically impossible. The curvatures of the spheres can be taken into account by using a parabolic approximation instead of a linear one for spheres. The calculated deviation from Bragg's incidence using this approach is given by [65]:

$$\Delta\theta_B = \theta - \theta_B = \frac{-\gamma_0 + \sqrt{\gamma_0^2 - (\gamma_0 - \gamma_h)\sqrt{1-\gamma_0^2}\chi_0/sin2\theta_B}}{\sqrt{1-\gamma_0^2}} \quad (3.30)$$

This shows a finite limit equal to critical angle of total external reflection, α_c, for deviation from Bragg's angle when the incidence angle tends towards zero. Furthermore, the value of deviation depends on mass density of the material via χ_0. This implies that one can deduce the surface density variation of a crystal via monitoring the different deviation value for an identical glancing angle γ_0. Fig. 3.4a shows the variation of Bragg shift with incidence angle, calculated for typical three values of χ_0 for Si (331) reflection at $Cu\ K\alpha$ radiation.

Variation of the Darwin width for a grazing incidence

The angular width of the total reflection domain, or Darwin width, is determined by the angle between the normals of the crystal surface which are tangent to the two branches of the dispersion surface, respectively. This remark was used by Rustichelli [66] to calculate this width when the two spheres of centres O and H and with radii nk cannot be approximated by their tangential planes.

$$\mathbf{2\delta_{oc}} = \frac{\mathbf{2\delta_o}\sqrt{|\boldsymbol{\gamma}|}\,\boldsymbol{\alpha_i}}{\sqrt{(\boldsymbol{\alpha_i})^2 - \boldsymbol{\alpha_i}\boldsymbol{\chi_0}\,\mathbf{tan}\boldsymbol{\theta_B} - \boldsymbol{\chi_0}}} \quad (3.31)$$

where $2\delta_o = \frac{\sqrt{\chi_h\chi_{\bar{h}}}}{sin2\theta_B}$ is the Darwin width for symmetrical reflecion. It can be seen that the widths of the rocking curves is tends toward zero as incidence angle tends toward Zero. It passes through a maximum equal to $\mathbf{2\delta_o}\sqrt{|\boldsymbol{\gamma_h}|}/\sqrt{\mathbf{2}\alpha_c}$ for incidence angle equal to critical angle [63]. Fig 3.4b shows the variation of Darwin width with incidence angle, calculated for Si (331) reflection at $Cu\ K\alpha$ radiation.

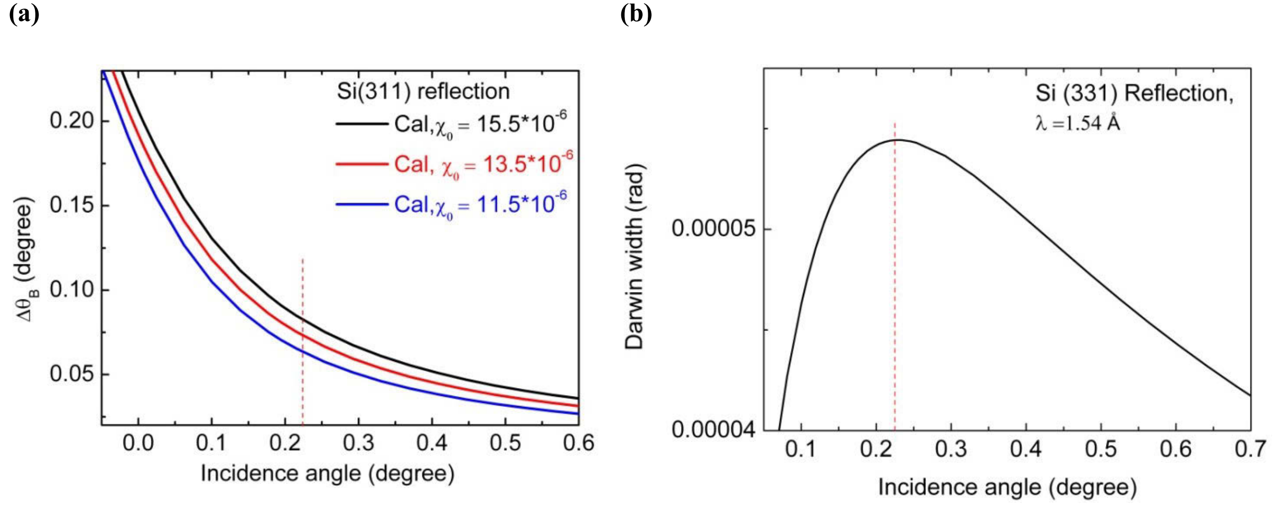

Figure 3.4: (a) The calculated dynamical Bragg peak shifts ($\Delta\theta_B$) versus α_i for the Si at Si (331) reflection at non-coplanar scattering geometry for χ_0 =15.5 × 10^{-6} (black), χ_0 =13.5 × 10^{-6} (red), and χ_0 =11.5 × 10^{-6} (blue). Decreasing in χ_0 results in less deviation from Bragg's angle. (b) The calculated Darwin width (DW) variation with incidence angle (α_i) for RCs of Si (331) reflection at non-coplanar geometry using $Cu\ K\alpha$: χ_0^{Si} = 15.5 × 10^{-6} and χ_h^{Si} = 0.5162 × 10^{-5} . The vertical dashed lines show the position of the critical angle.

Shape of the rocking curve

Shape of the rocking curve is asymmetric and was studied by Bucksch *et al.* [67]. The asymmetry is due to the anomalous absorption effect: on the small-angle side, the reflected intensity is associated with wavefield belonging to branch 1 of the dispersion surface which undergoes an absorption smaller than normal, while on the high-angle side it is associated with wavefield belonging to branch 2 with an absorption higher than normal. The amount of asymmetry depends on the asymmetry ratio γ (see Fig. 3.7c) and on the values of the Fourier coefficient of the imaginary part of the plarizability, χ_{io} and χ_{ih}.

3.3 Experimental realization

All scattering experiment can be interpreted as the measurement of intensities along certain paths, or surfaces, in reciprocal space. The resulting accessible range of RS is shown in Fig. 3.5a. In any

scattering measurement, the momentum transfer is limited to $|\boldsymbol{Q}| = Q = 2k = 4\pi/\lambda$, as indicated by the outer half-sphere. Due to the smaller absorption length of X-ray, $k_{iz} \leq 0$, $k_{if} \geq 0$ and consequently $Q_z \geq 0$, therefore only the upper half-sphere $Q < 2k$ is accessible. Furthermore, the small two half-spheres on the left and right contain points that cannot be accessed in reflection because the incident beam would enter from below the crystal surface for the former case and the diffracted beam exits through the crystal in the later case. These two regions so-called *Laue zones* are accessible in transmission. Only the region between these Laue zones and the outer half sphere is accessible to the scattering experiments. The most general scattering geometry is illustrated in Fig. 3.5a, where the incident wave $\boldsymbol{k}_i$ hits the sample under an incidence angle α_i, and the scattered radiation is measured in the direction $\boldsymbol{k}_f$, under an exit angle α_f with respect to the surface, and an in-plane scattering angle 2θ. The momentum transfer is defined by theses angles and is shown in parallel and vertical parts $Q_{\parallel} = (Q_x, Q_y, 0)$ and $Q_{\perp} = (0,0,Q_z)$, respectively.

Fig. 3.5b shows the accessible range of RS included with the reciprocal space map showing the position of the a few measured Bragg peaks in Si (001) using $Cu\ k_{\alpha}$. The figure is drawn with the crystallographic [001] direction along the z-axis and for a sample azimuth with the [110] crystallographic direction along the incident beam ($k_{i\parallel} \parallel [110]$).

In general, the possible scattering geometries can be divided into five parts:
(I) If only vicinity of the origin of reciprocal space (000) is investigated, the coplanar X-ray reflectivity (XRR) is measured; (II) If this is not case, the geometry is called grazing incidence small angle X-ray scattering (GISAXS); (III) Measurements around Bragg reflection (hkl) other than (000) are usually named as X-ray diffraction (XRD) in coplanar geometry, or (IV) grazing incidence diffraction (GID) for Bragg reflection (hkl) with $l = 0$; (V) The remained geometry is non-coplanar XRD.

The scattering in the geometries of GISAXS and GID (II and IV) have be already reported in our group [68]. In this work we applied XRR and XRD in coplanar and non-coplanar geometries (I, III and V).

XRR in Reciprocal space

Due to the coplanar geometry, only two coordinates of Q are considered. The incidence angle α_i is commonly referred to as ω and the exit angle is $\alpha_f = 2\theta - \omega$. The accessible in-plane wavevector transfer $|Q_{\parallel}| = Q_x$ is limited by the laue zones. The reciprocal space coordinates are determined as:

$$Q_x = 2\pi/\lambda(cos(2\theta - \omega) - cos(\omega)) \quad (3.32)$$

$$Q_z = 2\pi/\lambda(sin(2\theta - \omega) + cos(\omega)) \quad (3.33)$$

As the scattered intensity usually drops quite fast as a function of Q_z , the range of lateral momentum transfer is limited.

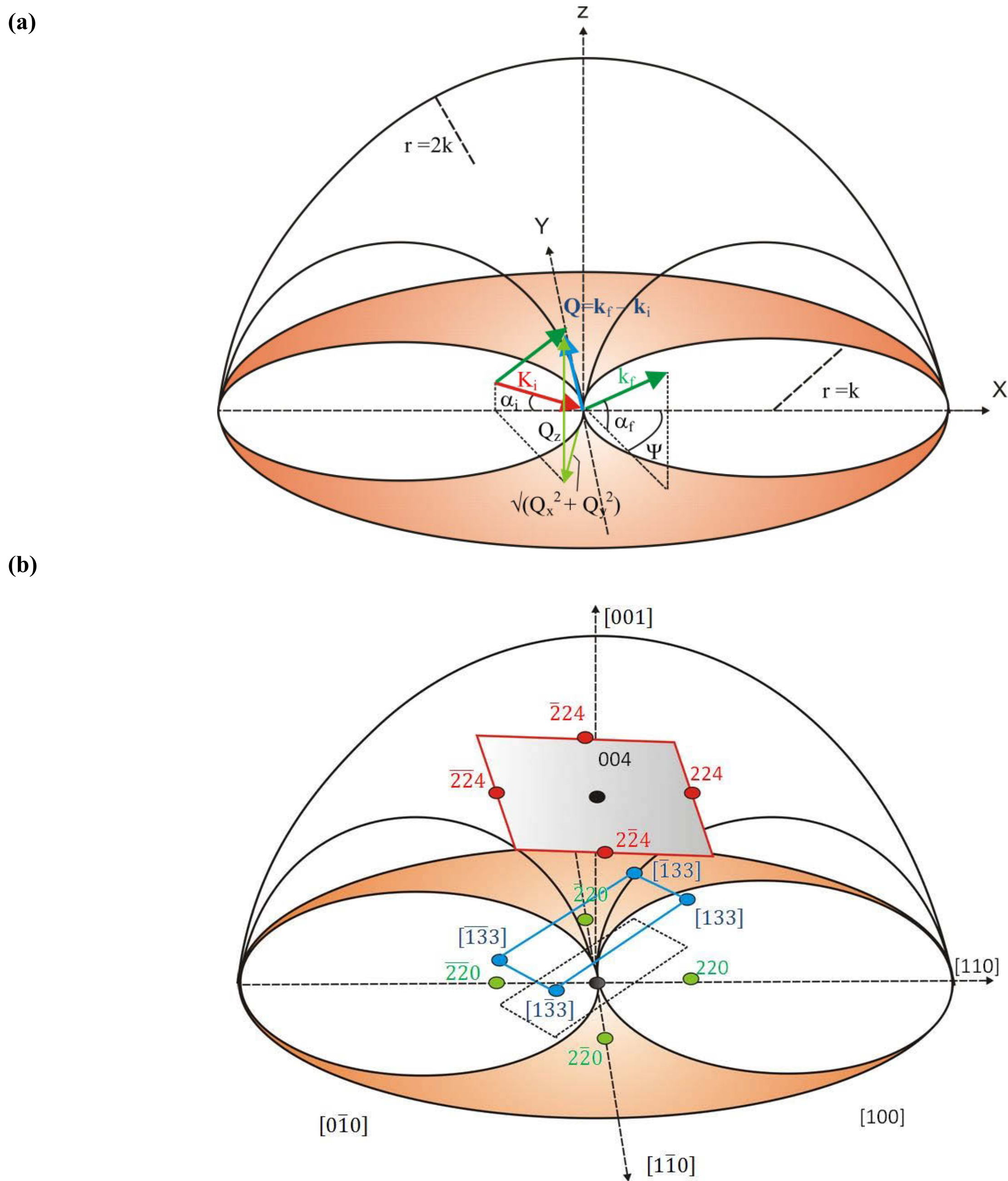

Figure 3.5: (a) Sketch of the reciprocal space (RS) regions that are accessible in coplanar scattering geometry. Because of limitation of momentum transfer by $|\boldsymbol{Q}| \leq 2k$, the space beyond the large half-sphere cannot be accessed. Since the incident and scattered beams cannot penetrate through the investigated samples, the so-called Laue zones (inside the smaller two half-spheres) are inaccessible as well. (b) Location of some Bragg peaks of Si(001) in RS. For $Cu\ k_{\alpha}$ radiation while Si 004 and 224 reflections are accessible, Si 133 reflection remains in Laue zones.

Coplanar high angle X-ray diffraction (XRD)

The XRD setup is from the geometry point of view equivalent to the XRR setup. The vicinity of a certain reciprocal lattice point (RLP) of (hkl) with $l \neq 0$ is probed. In coplanar geometry k_i , k_f and surface normal n_0 lie in same plane. Si 004 and 224 Bragg reflections using $Cu\ k_\alpha$ radiation (see Fig. 3.5b) are measured in this setup. The XRD setup is sensitive to in-plane and vertical component of the crystal lattice. A disadvantage of this geometry is that the incidence and exit angles cannot be chosen independently of the scattering angles. Usually these angles are much larger than the critical angle for total external reflection, and thus the radiation usually penetrates deep into the substrate, giving an unfavorable ratio of scattering intensity from surface layers and crystal bulk.

3.3.1 Surface-sensitive extremely asymmetrical X-ray diffraction (EAD)

EAD is very sensitive to small variations of the mass density as well as to strain components close to the surface. This technique combine some advantages of grazing incidence diffraction (GID) and XRD, namely sensitivity to the near-surface due to the small incidence angle, and the finite vertical momentum transfer Q_z, making the geometry sensitive for vertical strain components. There is two approaches for realization, the first is based on variation of the diffraction geometry which can be achieved with conventional laboratory X-ray sources, and the second is based on synchrotron radiation with the possibility to change the wavelength at fixed diffraction geometry.

Non-coplanar EAD with changing the scattering geometry

The non-coplanar geometry adds an additional degree of freedom for choosing the incidence and exit angles of X-rays with respect to the sample surface [69]. In this geometry the diffraction plane (hkl), i.e., the plane scanned by k_i and k_f, is inclined by φ angle with respect to the surface and can be rotated around its reciprocal lattice vector $Q(hkl)$ (Fig. 3.6a). In coplanar diffraction an asymmetric lattice plane is accessible by rotation of the sample by φ providing incidence angle $(\theta + \varphi)$ and exit angle $(\theta - \varphi)$, for example. In contrast to this, in EAD geometry one can access any angle of incidence/exit by rotation of the sample by angle ψ, where

both incidence and exit angle describe a cone around the lattice vector $Q(hkl)$, (See Fig. 3.6a). The diffraction condition for (hkl) will be fulfilled for each azimuth-angle ψ (rotation angle around Q) leading to a variation of incident and exit angles, α_i and α_f of the X-ray beam with respect to the surface given by:

$$sin\,\alpha_i = sin\,\theta_B\,cos\,\varphi - cos\,\theta_B\,sin\varphi\,cos\,\psi = sin\Theta sin\chi \quad (3.34)$$

$$sin\,\alpha_f = sin\,\theta_B\,cos\,\varphi + cos\,\theta_B\,sin\varphi\,cos\,\psi = sin(2\Theta - \Theta)sin\chi \quad (3.35)$$

The right hand side of Eqs. 3.34-35 define the incidence and exit angle in the coordinate system of a four circle diffractometer (assuming the SPEC notation: 2Θ, Θ, χ , and φ) defining $\chi = 90°$ if the diffraction plane perpendicular to the sample surface and $\chi = 0$ if the diffraction plane parallel to the sample surface. The reciprocal space coordinates can be derived from the goniometric angles as (Fig. 3.6b):

$$Q_x = k(cos\alpha_f\,cos\,\psi - cos\,\alpha_i) \quad (3.36)$$

$$Q_y = k(cos\alpha_f\,sin\,\psi) \quad (3.37)$$

$$Q_z = k(sin\alpha_f + sin\alpha_i) \quad (3.38)$$

In fact, these coordinates are general coordinates that can be applied for all 5 possible scattering geometries (see subsection 3.3) by choosing the appropriate value for rotations angles. For instance, for XRR condition by using $\psi = \varphi = 0°$, and for grazing incidence diffraction (GID) condition via $\varphi = 90°$ and $\psi = 2\theta$, the corresponding reciprocal space coordinates are reproduced.

(a)

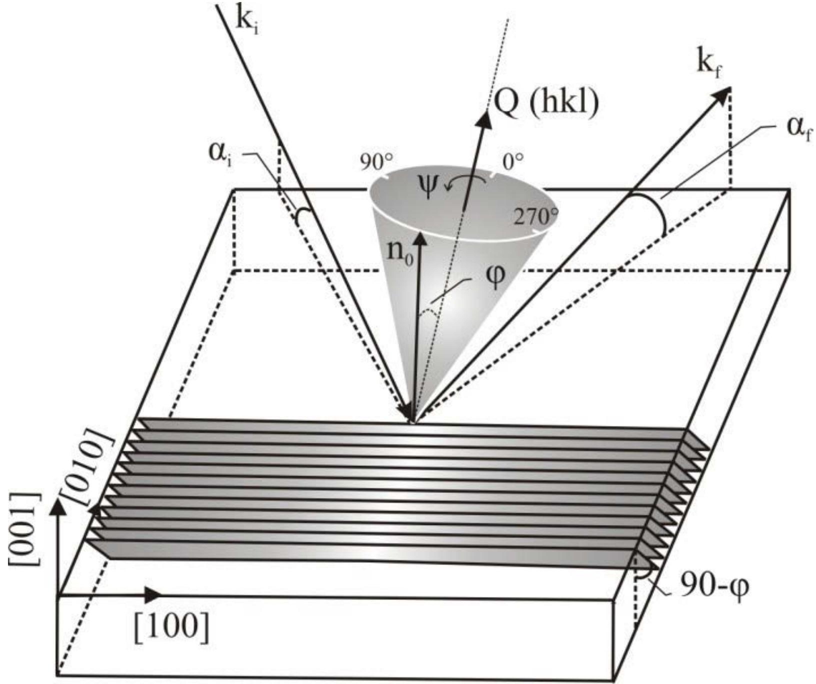

(b)

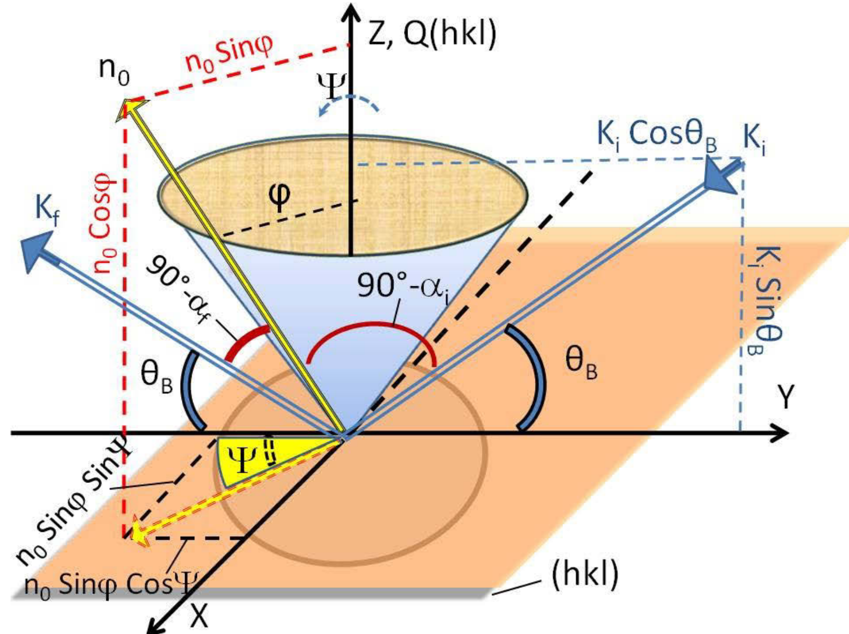

Figure 3.6: (a) The non-coplanar EAD geometry. The shaded planes are parallel to the lattice planes; φ is their angle with the crystal surface. The incident angle α_i is chosen independent of the diffraction vector $\mathbf{Q} = \mathbf{k_f} - \mathbf{k_i}$ by rotating the diffraction plane (spanned by incident scattered wav vector $\mathbf{k_i}$ and $\mathbf{Q}$) around $\mathbf{Q}$. The cone with vertex angle of φ generated by an equivalent rotation of surface normal $\mathbf{n_0}$ around $\mathbf{Q}$ illustrates the different azimuthal orientation for an asymmetric reflection (ψ cone). (b) EAD geometric angles to extract the reciprocal space coordinate. The lattice planes (hkl) lying oblique to the surface at the φ angle.

For α_i below or close the critical angle, the scattering geometry becomes surface sensitive. It is also obvious that a very small α_i can not be selected for an arbitrary RLP, there is a minimum value of α_i which is exactly the value for coplanar, steep exit geometry. Consequently , the RLPs allowing to tune α_i to angles below the critical angle are those which lie within the laue zones and are inaccessible in coplanar geometry, as e.g., the (202), (331), (531) RLPs for Si(001) and $Cu\ k_\alpha$ radiation.

According to Eqs. 3.34-35, By variation of ψ for a Si(001) wafer ([001] || n_0), to obtain the Si (331) reflection using $Cu\ k_\alpha$ radiation both α_i and α_f can be varied from -8.33° (condition of grazing incidence in coplanar scattering geometry at $\psi = 0°$) via 25.17° (this is the pseudo symmetric case at ψ = 90° or 270°) to 84.69° (grazing exit condition at ψ = 180°). As negative values of incidence and exit angles cannot be accessed, the useful variation of ψ is limited to a range between 41.75° and 138.24° or 221.75 and 318.24° with respect to the [010] direction, corresponding to a variation of α_i from 0° to 58.3° or 58.3° to 0°, respectively (Fig. 3.7a).

Since the penetration depth of X-ray depends on α_i, it can be controlled by the appropriate choice of ψ. Fig. 3.7b (black curve) shows the variation of the penetration depth versus ψ and α_i calculated for the Si (331) reflection in non-coplanar EAD geometry using Eq. 3.6. It can be seen that by reducing α_i from 1° to 0° the penetration depth decreases from several microns down to around 6 nm.

Coplanar EAD with changing the wavelength,

The alternative method for reducing a penetration depth of X-ray on surface accompanied by simultaneously full filled Bragg condition is variation of wavelength at fixed scattering geometry [70]. This method is based on coupling between wavelengths with the incidence and scattered angels induced by crystal [62]. In fact, the wavelength and angles diffracted by the crystal must obviously satisfy Bragg's law, and duMond realized that a plot of wavelength versus incidence angle would show the diffraction geometry of the crystal reflection. This is shown in Fig. 3.7d and is obviously part of a sin curve. Instead of changing the scattering geometry, it is possible to record the scattering profile by changing the wavelength at constant incidence angle and consequently fixed penetration depth.

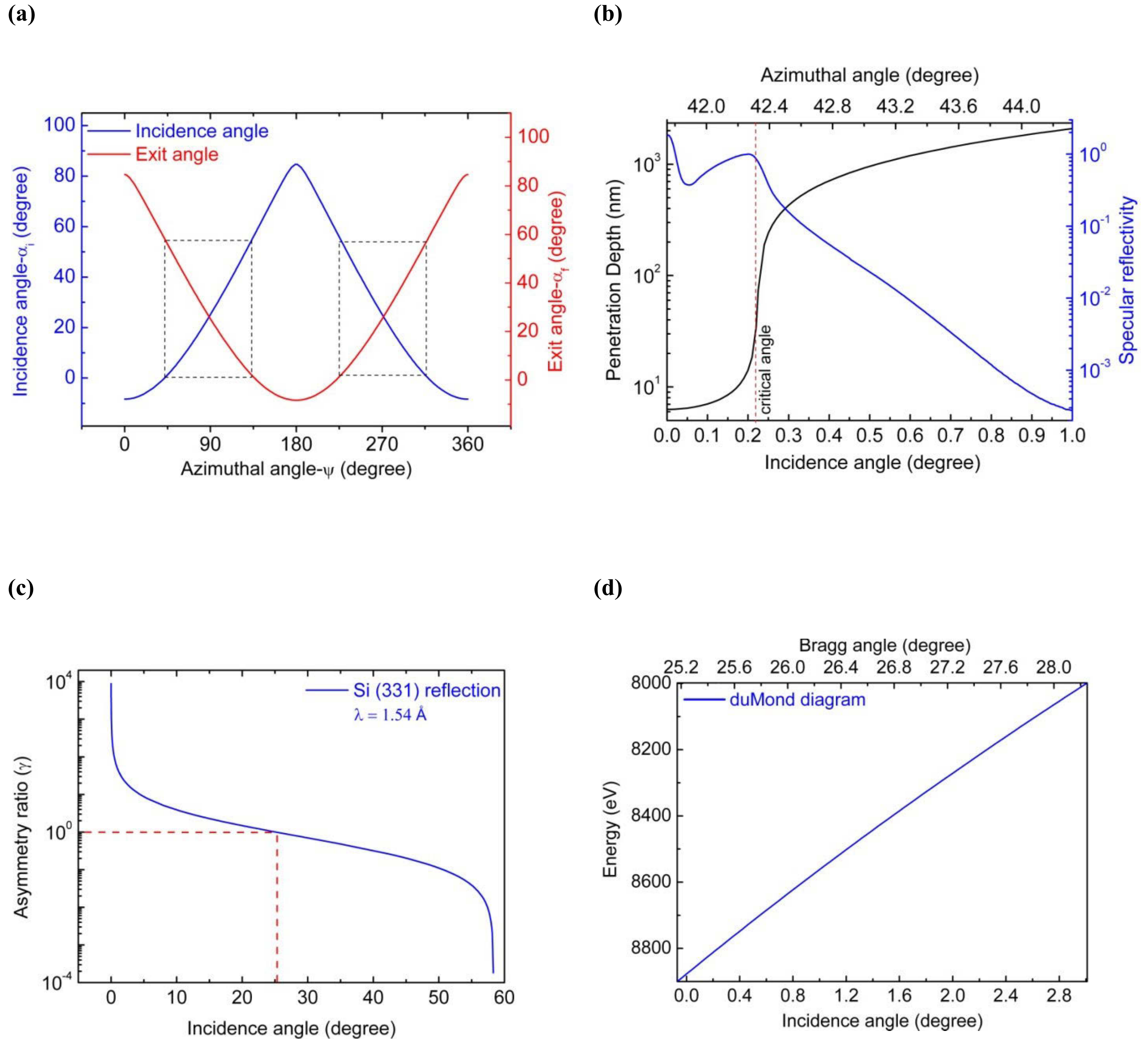

Figure 3.7: (a) Azimuthal angle dependence of incidence angle (blue) and exit angle (red). When ψ varies from 0° to 360°, incidence angle, α_i , and exit angle, α_f , vary in the ranges from -8.33° to 84.69°. Dashed rectangles show the accessible areas for satisfying the Bragg conditions. (b) Calculated penetration depth of X-rays (λ = 1.54 Å) into silicon as a function of angle of incidence (black curve) and measured reflectivity of X-rays (blue curve). (c) the variation of calculated asymmetry ration (γ) as function of incidence angle for Si 331 reflection at non-coplanar geometry. Dashed line shows the position of quasi-symmetric condition at α_i = 25.17° for that $\gamma = 1$. (d) duMond diagram showing the wavelength-angle coupling imposed by the Bragg law.

3.4 X-ray absorption methods

Physical principle

When a beam of X-ray photons passes through a material, the incident intensity, $\boldsymbol{I}$, decreases by an amount that is determined by the absorption characteristics of the material being irradiated. For the path length $\boldsymbol{dx}$ of the radiation through the material the decrease $\boldsymbol{dI}$ is given by [51]:

$$\boldsymbol{dI = -\mu(E)Idx} \tag{3.39}$$

with the liner absorption coefficient $\boldsymbol{\mu(E)}$ a function of photon energy. Integration over the total thickness $\boldsymbol{x}$ yields *Lambert's law*,

$$\boldsymbol{I_t = I_0 e^{-\mu(E)x}} \tag{3.40}$$

At most X-ray energies, the absorption coefficient $\boldsymbol{\mu(E)}$ is a smooth function of energy, with a value that depends on the sample density $\boldsymbol{\rho}$, the atomic number $\boldsymbol{Z}$, atomic mass $\boldsymbol{A}$, and the X-ray energy $\boldsymbol{E}$ roughly as [71]

$$\boldsymbol{\mu \approx \frac{\rho Z^4}{AE^3}} \tag{3.41}$$

Photoelectric absorption

When the incoming photons have energy equal to that of binding energy of a core-level electron cause to excite an electron to a vacant excited state or to the continuum with kinematic energy given by [71]:

$$KE = h\nu - BE - \phi \tag{3.42}$$

where $h\nu$ is the energy of the photon, BE is the binding energy of the orbital from which the electron originated, and ϕ is the spectrometer work function. This process is called photoelectric

absorption (see Fig. 3.8a). Following a photoelectric absorption event, the atom will be in an excited state. The excited state will decay within a few femtoseconds of the absorption event via two mechanisms. The first by X-ray fluorescence (Fig. 3.8b-left), in which a higher energy core-level electron fills the dipper core hole and leads to eject an X-ray. The fluorescence energies emitted in this way are characteristic of the atom. The second process for de-excitation of the core hole is the Auger effect (Fig. 3.8b-right), in which an electron drops from a higher electron level and a second electron is emitted into the continuum (and possibly even out of the sample). For X-ray energy regime $> \mathbf{2KeV}$, X-ray fluorescence is more likely occur than Auger emission, but for lower energy of X-ray absorption, Auger process dominates.

The binding energy may be regarded as the energy difference between the initial and final states after the photoelectron has left the atom. Variation in the elemental binding energies (the chemical shifts) arise from differences in the chemical potential and polarizability of the compounds. This chemical shift can be used to identify the chemicals state of the materials being analyzed using X-ray photoelectron spectroscopy.

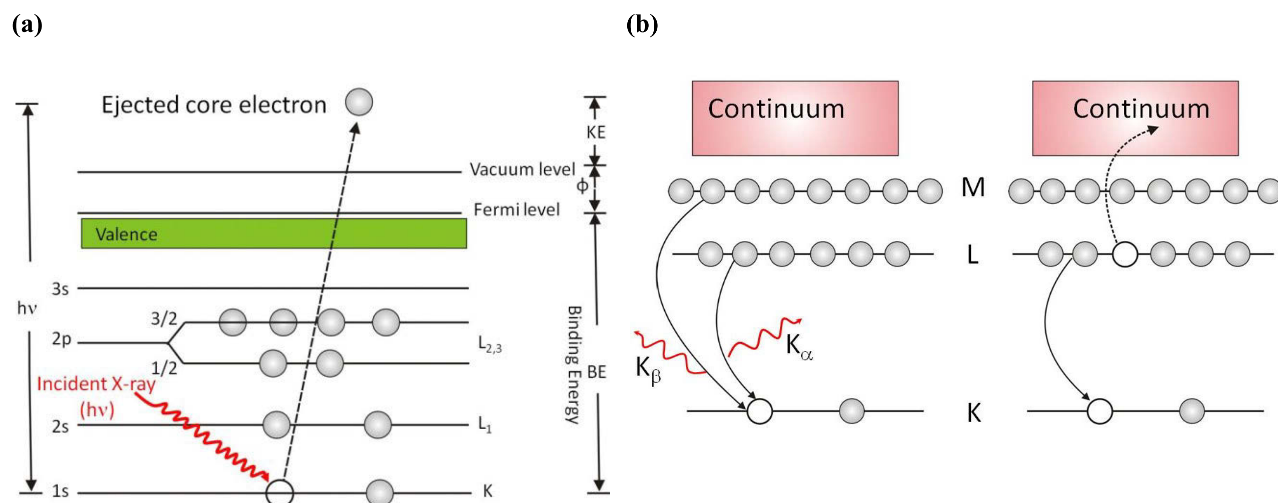

Figure 3.8: (a) Schematic diagram of the photoelectric absorption process, showing photoionization of an atom by ejection of a 1s electron. (b) Decay of the excited state: X-ray fluorescence (left) and the Auger effect (right). In both cases, the probability of emission (X-ray or electron) is directly proportional to the absorption probability.

3.4.1 X-ray Photoelectron Spectroscopy (XPS)

Surface analysis by XPS is accomplished by irradiation a sample with mono-energetic X-rays $Mg\ k\alpha$ (1253.6 eV) or $Al\ k\alpha$ (1486.6 eV), as usual. Theses photons have limited penetrating power in a solid on the order of 1-10 micrometers. They interact with the atoms in the surface region; causing electrons to be emitted by the photoelectron effect (see Fig. 3.9a). While ionization occurs to a depth of a few micrometers, only those electrons that originate within tens of angstroms below the solid surface can leave the surface without energy loss. These electrons produce the peaks in the spectra and the electrons that undergo inelastic loss processes before emerging form the background. The intensity of electron (I) emitted from all depths greater than d in a direction normal to the surface is given by the *Beer-Lambert relationship* [71]:

$$I = I_0 \exp(-d/\lambda cos\theta) \qquad (3.43)$$

were I_0 is the initial intensity, d is analysis depth, λ is attenuation depth and θ is angle of emission measured with respect to the surface normal. A appropriate analysis of the above equation shows that for $= 0°$, some 65% of the signal in electron spectroscopy will originate from depth of less than 1λ, 85% from a depth of $d < 2\lambda$, and 95% from a depth of $d < 3\lambda$, as illustrated in Fig. 3.9b. The values of the attenuation depth is of the order of a few nanometres, thus the depth from which information can be derived is a few nanometers. The Beer-Lambert equation can be manipulated in a variety of ways to provide information about over-layer thickness and to provide a non-destructive depth profile.

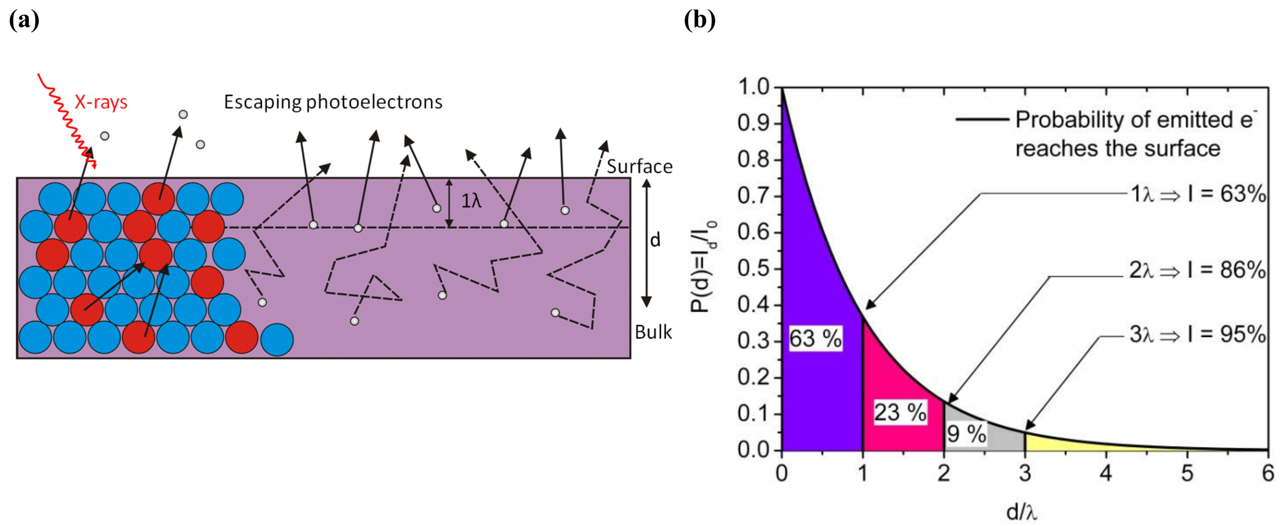

Figure 3.9: (a) Schematic of X-ray photoelectron spectroscopy, the horizontal dashed line indicates a distance from the surface of the attenuation length, λ. (b) The variation of electron intensity with analysis depth.

The depth of analysis in electron spectroscopy

The depth of analysis in XPS varies with the kinetic energy of the electron under consideration. It is determined by a quantity known as the attenuation length (λ) of electrons, which is related to the inelastic mean free path length (IMFP). In general, the attenuation length is about 10 percent less than the IMFP. A relationships which relate λ to electron energy and material properties was proposed by Seah and Dench [72] as:

$$\lambda = \frac{538a_A}{E_A^2} + 0.41a_A(a_A E_A)^{0.5} \tag{3.44}$$

where E_A is the energy of the electron in eV, a_A^3 is the volume of the atom in nm^3 and λ is in nm. The calculated attenuation length of electrons vs. electron energy for Silicon is illustrated in Fig. 3.10a showing an increasing attenuation length of electron with electron energy for energy of above 50 eV.

Non-destructive depth profiling methods

XPS can provide compositional information as a function of depth. This can be achieved by manipulating the Beer-Lambert equation either to increase or to decrease the integral depth of analysis non-destructively by changing the geometry of the experiment. As the depth of analysis depends on the angle of emission via $d = 3\lambda cos\theta$ (see Eq. 3.43), at high value of θ a spectrum is recorded with extremely surface sensitivity. As normal electron emission is approached ($\theta = 0°$), the analysis depth move towards the limiting value of ~ 3λ. The variation of sampling depths at different emission angles are illustrated schematically in Fig. 3.10b.

An alternative method for depth profiling is the variation of analysis depth via tuning energy of the emitted electron. This method can be carried out using synchrotron radiation providing variable X-ray photon energies. The variation of attenuation depth with kinetic energy, giving a possibility to obtain a degree of depth selectivity, $d = 3\lambda$, is shown in Fig. 3.10c.

(a)

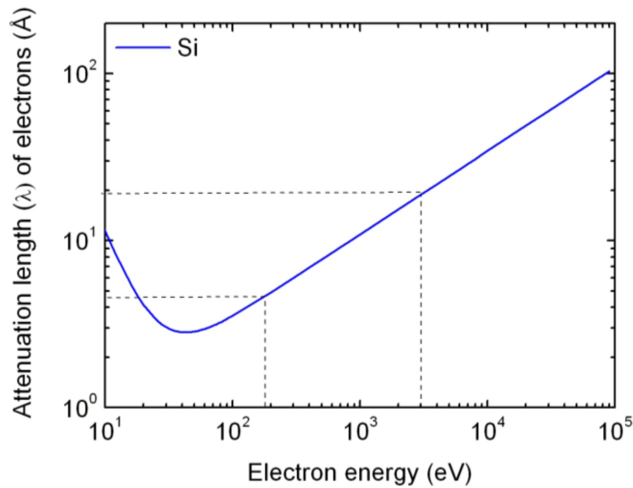

Figure 3.10: (a) Calculated variation of attenuated length of electron Vs. energy of electron in Si. (b) Angular electron emission: sampling dept ($d = 3\lambda cos\theta$) at different emission angles. The widths of the shaded areas represent the proportion of the detected electron emitted as a function of depth. The horizontal dashed line indicates a distance from the surface of the attenuation length (λ). (c) Depth profiling by means of X-ray photon energy variation.

(b)

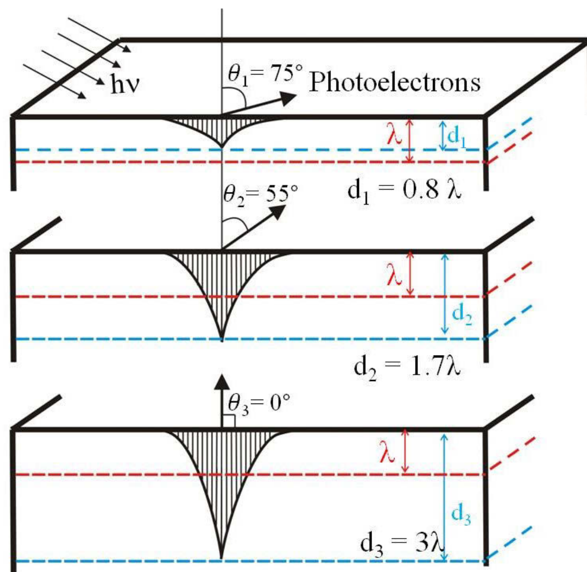

(c)

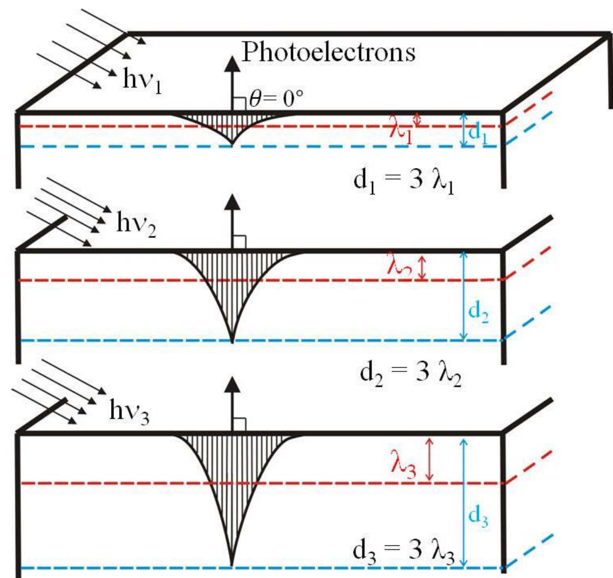

3.4.2 X-ray absorption spectroscopy (XAS)

The lack of an extensive regular structure in amorphous material, limits the amount of unambiguous structural information which can be gained from conventional structural techniques such as X-ray diffraction. This problem is particularly severe for those systems which have small

percentages of impurity atoms. XAS is a technique which can probe the structure of atoms surrounding each species of atom in the material simply by tuning the X-ray energy to the absorption edge of that element [73]. Importantly, crystallinity is not required for XAS measurements, making it one of the few structural probes available for non-crystalline and highly disordered materials. The X-ray absorption spectrum is typically divided into two regimes: X-ray absorption near edge spectroscopy (XANES) and extended X-ray absorption fine-structure spectroscopy (EXAFS). XANES is strongly sensitive to formal oxidation state and coordination chemistry of the absorbing atom, while the EXAFS is used to determine the distance, coordinate number, and species of neighbours of the absorbing atom.

EXAFS and near-edge structure

The photoelectric absorption process leads to a sharp rise in the absorption intensity. This sharp rise is denoted as absorption edge (E_0). For EXAFS, we are concerned with the intensity of $\boldsymbol{\mu}$ as a function of energy, near and at energies just above the $\boldsymbol{BE}$ of a known core level of a known atomic species defined by [74]:

$$\chi(E) = \frac{\mu(E) - \mu_0(E)}{\Delta\mu_0(E)} \tag{3.45}$$

EXAFS can be measured either in transmission or fluorescence geometries. The energy dependence of the absorption coefficient $\boldsymbol{\mu(E)}$ is measured either in transmission as

$$\mu(E) = \log\,(I_0/I) \tag{3.46}$$

Or in X-ray fluorescence as

$$\mu(E) \propto I_f/I \tag{3.47}$$

where, $\boldsymbol{I_f}$ is the monitored intensity of a fluorescence line associated with the absorption process. EXAFS is best understood in terms of the wave behaviour of the photon-electron created in the absorption process. It is common to convert the X-ray energy to $\boldsymbol{k}$, the wavevector of the photoelectron,

$$\boldsymbol{k} = \sqrt{\frac{2m(E-E_0}{\hbar^2}} \tag{3.48}$$

with $\boldsymbol{k}$ the wavevector, $\boldsymbol{m}$ the electron mass and $\boldsymbol{h}$ Plank's constant ($\hbar = \boldsymbol{h}/2\boldsymbol{\pi}$). The primary quantity for EXAFS is then $\boldsymbol{\chi}(\boldsymbol{k})$, the oscillation as a function of photoelectron wave vector and decay quickly with $\boldsymbol{k}$. To emphasize the oscillations, $\boldsymbol{\chi}(\boldsymbol{k})$ is often multiplied by a power of $\boldsymbol{k}$ typically $\boldsymbol{k}^2$or $\boldsymbol{k}^1$.

The different frequency apparent in the oscillations in $\boldsymbol{\chi}(\boldsymbol{k})$ corresponded to different near-neighbor coordination shells which can be described and modelled according to the EXAFS equation.

Theoretical outline

EXAFS is best understood in terms of the wave behaviour of the photoelectron created in the absorption process. Quantum mechanically the outgoing photoelectron can be represent as a spherical wave with wavelength $\boldsymbol{\lambda_e}$ define as $\boldsymbol{\lambda_e} = 2\boldsymbol{\pi}/\boldsymbol{k_e}$, (Fig. 3.11a) that scatters at neighbouring atoms (e.g., electron density), producing a backscattered wave (Fig. 3.11b). The outgoing and backscattered waves interfere, causing an interference pattern varying between total construction and total destruction. Since the path lengths of both waves define their final phases, it can be seen that the distance to the neighbouring atoms determine the interference pattern. The absorption coefficient exhibits a fine structure because the final wave state function is modulated due to the interference pattern.

Fig. 3.11c shows a photoelectric effect, in which an X-ray is absorbed by a core-level with BE, and a photoelectron with wave number $\boldsymbol{k}$ is created and propagates away from the atom. When a neighbouring atom is included in the Fig. 3.11d, the photoelectron can scatter from the electrons of this neighbouring atom, and the scattered photo-electron can return to the absorbing atom. Since the absorption coefficient depends on whether there is an available electronic state (that is whether there is an electron at the location of the atom and at the appropriate energy and momentum), the presence of the photoelectron scattered back from the neighbouring atom will alter the absorption coefficient. This is the origin of XAFS.

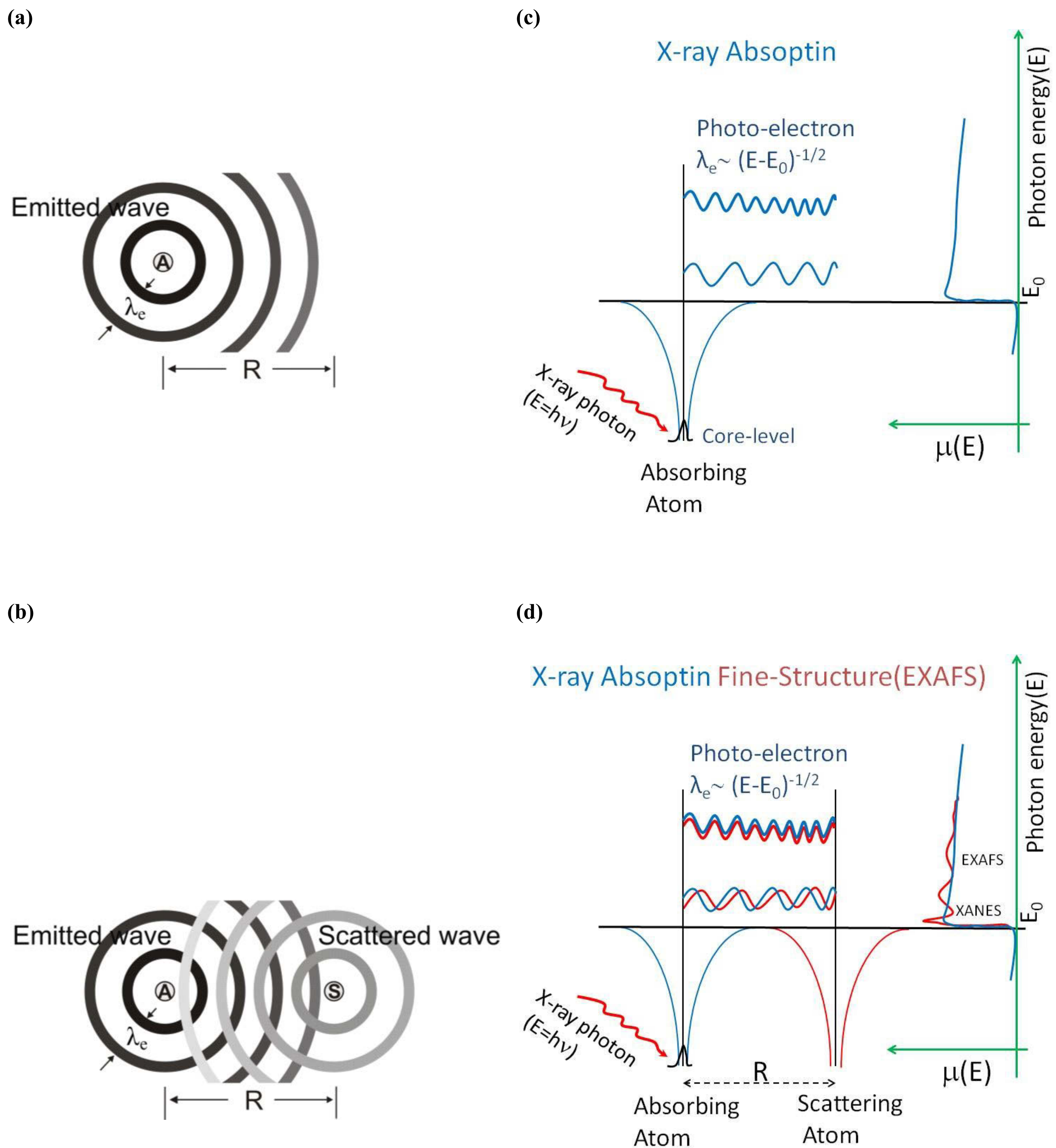

Figure 3.11: (a) cartoon of X-ray absorption effect in terms of outgoing photoelectron from absorber atoms A , represented as a spherical wave with wavelength $\boldsymbol{\lambda_e}$. (b) schematic illustration of backscattered photoelectron from neighbouring atom S about the absorber atom A. (c) absorption coefficient $\mu\ (E)$, in absence of neibouring atoms. (d) XAFS occurs because the photo-electron can scatter from a neighboring atom. The scattered photo-electron can returne to the absorbing atom, modulating the amplitude of the photo-electron wave-function at the absorbing atom. This is turn modulates the absorption coefficient $\mu\ (E)$, causing the EXAFS.

Since X-ray absorption is a transition between two quantum state, we describe $\boldsymbol{\mu(E)}$ with *Fermi's Golden Rule* [75]:

$$\boldsymbol{\mu(E) \propto |\langle i|\mathcal{H}|f\rangle|^2} \quad (3.49)$$

where $\boldsymbol{\langle i|}$ represent the initial state (an X-ray, a core electron, and no photon-electron), $\boldsymbol{|f\rangle}$ represent the final state (no X-ray, a core hole, and a photo-electron), and $\boldsymbol{\mathcal{H}}$ is the interaction term. Since the core-level electron is very tightly bound to the absorption atom, the initial state will not be altered by the presence of the neighbouring atom. The final state, on the other hand, will be affected by the neighbouring atom because the photo-electron will be able to see it. We can expand $\boldsymbol{|f\rangle}$ into two pieces, one that is the "bare atom" portion ($\boldsymbol{|f_0\rangle}$), and one that is the effect of the neighbouring atom ($\boldsymbol{|\Delta f\rangle}$) as

$$\boldsymbol{|f\rangle = f_0\rangle + |\Delta f\rangle} \quad (3.50)$$

$$\boldsymbol{\mu(E) = \mu_0(E)[1 + \chi(E)]} \quad (3.51)$$

$$\boldsymbol{\mu_0 = |\langle i|\mathcal{H}|f_0\rangle|^2} \quad (3.52)$$

Interference between theses two final-state causes the observed fine-structure in X-ray absorption spectra that can be written as:

$$\boldsymbol{\chi(E) \propto |\langle i|\mathcal{H}|\Delta f\rangle|} \quad (3.53)$$

Several authors have given derivation for the EXAFS theory [74, 76-78]. Theories of EXAFS based on scattering of the ejected photoelectron by atoms in the immediate vicinity of the absorbing atom give an expression for $\boldsymbol{\chi(k)}$ of the form

$$\boldsymbol{\chi(k) = \sum_j^{Shells} \left(\frac{N_j f_j(K)\, exp\left(-2k^2\sigma_j^2\right)}{kR_j^2}\right) sin\left[2kR_j + 2\delta_j(k)\right]} \quad (3.54)$$

where $\boldsymbol{f(k)}$ and $\boldsymbol{\delta(k)}$ are scattering properties of the atoms neighboring the excited atom, $\boldsymbol{N}$ is the number of neighboring atoms, $\boldsymbol{R}$ is the distance to the neighboring atom, and $\boldsymbol{\sigma^2}$ is the

disorder in the neighbour distance. The EXAFS equation allows us to determine $\boldsymbol{N}$, $\boldsymbol{R}$, and $\boldsymbol{\sigma^2}$ knowing the scattering amplitude $\boldsymbol{f(k)}$ and phase-shift $\boldsymbol{\delta(k)}$. Furthermore, since theses scattering factors depend on the Z of the neighbouring atom, EXAFS is also sensitive to the atomic species of the neighbouring atom [79, 80].

3.5 Experimental procedure

Synchrotron radiation sources

In a conventional tube, X-ray are generated if energetic electrons are stopped by impact with a metal target. The brightness of X-ray in this process is limited by thermal properties of solids. When electrons are confined to a circular orbit in a storage ring by a magnetic field, electromagnetic radiation is emitted due to the acceleration towards the center of the circle. At relativistic velocities, the emission becom strong in the forward direction and tangentional to the electron orbit. In a storage ring designed for production of synchrotron radiation, the orbit is not circular but consists of dipole bending magnets separated by straight sections. Beamlines are constructed to extract the beam from tangent points of the bending magnets or from insertion devices within the straight sections. In the latter, the electron beam is deflected in a small radius of curvature by a succession of dipole magnets of alternating sense: wigglers, in which the amplitude of oscillation is larger with respect to that of emitted radiation, and undulator in which it is small. General properties on synchrotron facilities are introduced in [81].

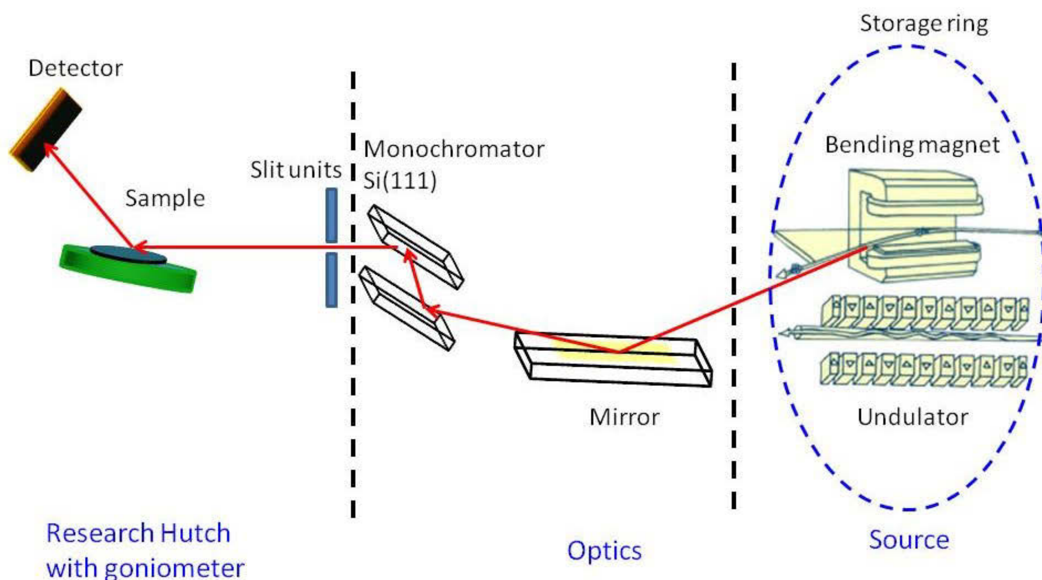

Figure 3.12: Schematic diagram of an electron storage ring and optics of synchrotron radiation: X-rays are created in the synchrotron storage ring and extracted into beamline. A Si (111) monochromator is used to select a certain wavelength out of the spectrum of source and mirrors guide and focus the beam further to the sample position. The energy of the beam is changed by changing the angle between the monochromator craytal and the incident beam.

Fig. 3.12 depicts schematically an experimental setup of measurements. Synchrotron radiation from the storage ring is monochromatized with either double crystal or a curved mirror monochromator.

Experimental setup

Most of the experiments at this work were done using synchrotron radiation at:

DELTA (1.5 GeV synchrotron radiation facility at TU-Dortmund)

Surface sensitive GI-XAS experiments were performed at beamline BL8 [82] at the superconducting asymmetric wiggler at DELTA [83] in the fluorescence mode. The emitted fluorescence radiation was recorded by a Si pin-diode detector placed at 90° with respect to the incident beam. For the XAS measurements, the excitation energy was varied in steps of 0.5 eV from -50 to 1000 eV across the Fe K-edge located at 7.112 keV using a Si(111) double crystal monochromator. The incident beam intensity was monitored by a N_2-gas filled ionization chamber, and the fluorescence data were recorded using a multi-channel analyzer and a digital processor. The energy scale of the monochromator was calibrated simultaneously for each sample by measuring an iron foil which was equipped between the second and a third ionization chamber in transmission mode. Due to the grazing incidence condition, the footprint of the incident beam with size of 50 μm × 5 mm (vertical × horizontal) was about 8 mm along the beam pass, matching the whole length of the samples. The experimental setup is shown in Fig. 3.13a. The measured absorption spectra have been analyzed with the software ATHENA which is included in the IFEFFIT program package for X-ray absorption spectroscopy analysis [84]. This includes normalization of all spectra and calibration with respect to the Fe K-edge.

The XPS experiments were carried out at the soft X-ray undulator beamline BL-11 of the DELTA storage ring [85] using a hemispherical electron energy analyzer. A variation of the excitation energies were used for compositional depth profiling. The Si 2p and Fe 3p core levels as well as the valence band (VB) distributions were used to evaluate the formed silicides in different stoichiometries using the energy of the C 1s peak (284.8 eV) as reference for the

binding energy (BE) scale. Each spectrum was fitted by a Shirley type background and Gaussian peak functions using the Fityk software [86]. Experimental setup is shown in Fig. 3.13b.

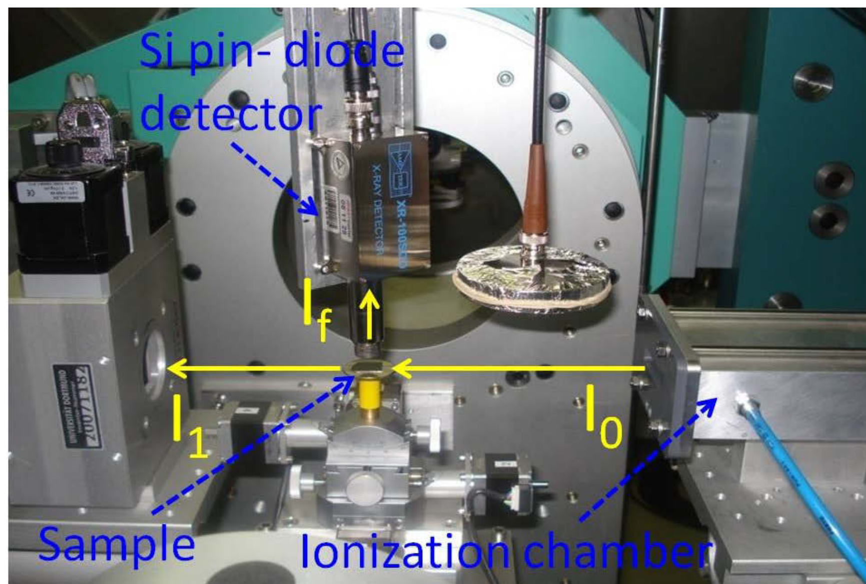

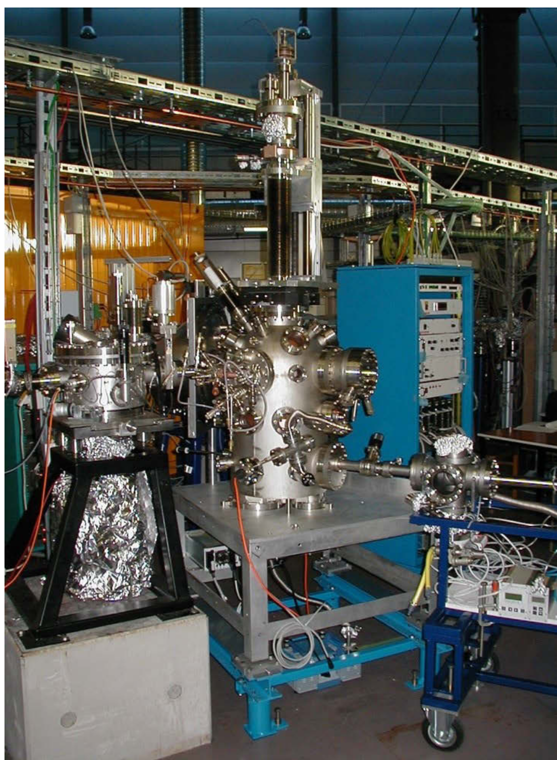

Figure 3.13: (a) The setup for a fluorescence grazing incidence X-ray absorption spectroscopy (GI-XAS) experiment at BL8 at DELTA. The incident beam intensity (I_0) and the reflected beam intensity (I_1) are measured by the ionization chambers. The emitted fluorescence radiation (I_f) was recorded by a Si pin-diode detector placed at 90° with respect to the incident beam. (b) A picture of the whole experimental X-ray photoelectron spectroscopy (XPS) setup at beamline 11 at DELTA.

ANKA (Synchrotron radiation facility at Karlsruhe institute of technology)

Surface sensitive EAD experiments with tuning wavelength were performed at beamline PDIFF at ANKA using 4-circle geometry Kappa-diffractometer equipped with Vantec-1 PSD Detector. The beam from 1.5T bending magnet source focuses on sample position using horizontally & vertically focusing mirror system (cut-off energy 21 keV). Depth profiling was carried out by energy tuning from 8500 eV to 8900 eV using a Si(111) double crystal monochromator. A sketch of the experimental set up is shown in Fig. 3.14

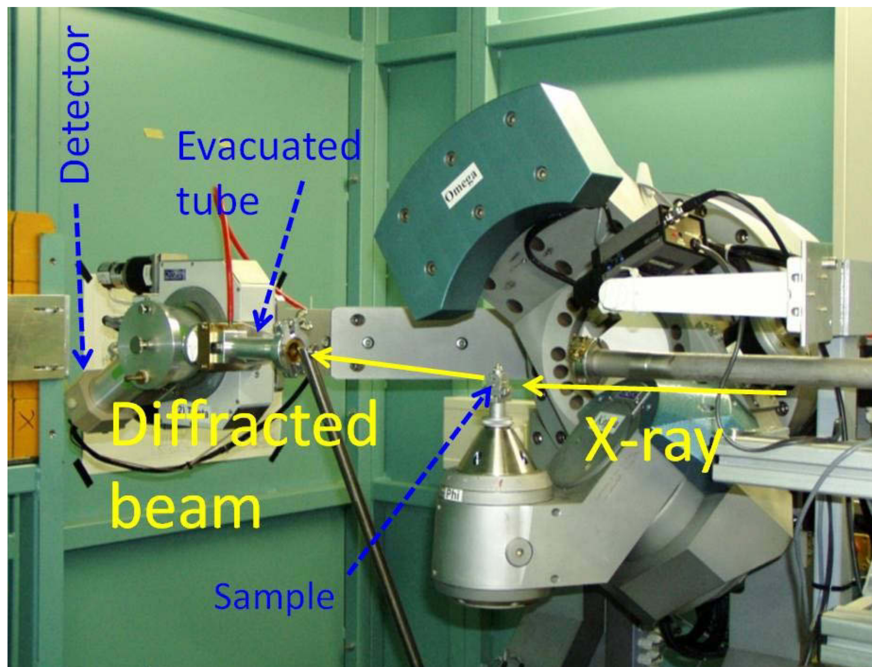

Figure 3.14: Experimental setup at BL-PDIF at ANKA: The 4-circle Kappa-goniometer equipped with a Vantec-1 PSD behind an evacuated tube. The photon energy was changed in the range of 8750 and 8900 eV to achieve Si(311) reflection in coplanar extremely asymmetry geometry. The incidence and diffracted beam direction were shown by yellow arrows. The sample state so that the surface normal [001] be perpendicular to incoming beam direction.

ESRF (European synchrotron radiation facility at Grenoble, France)

The annealing process was performed at beamline BM20 at ESRF using heating system Anton paar DHS 900. The temperature was selected in the range between room RT and 800°C in steps of 100°C. The heating rate was kept ~ 5°C/min. The selected samples were analyzed by coplanar grazing incidence X-ray diffraction (GI-XRD) using monochromatic beam of 11.5 KeV using a Si(111) double crystal monochromator and beam size of 0.15 mm × 0.5 mm (vertical × horizontal). The GI-XRD measurements were performed at a fixed incidenc angle (α_{in}) with a step size of 0.1° for maesurement during thermal annealing and 0.05° for measurements during depth profiling. The scattered beam was detected using a linear position sensitive detector. The setup of measurement is illustrated at Fig. 3.15.

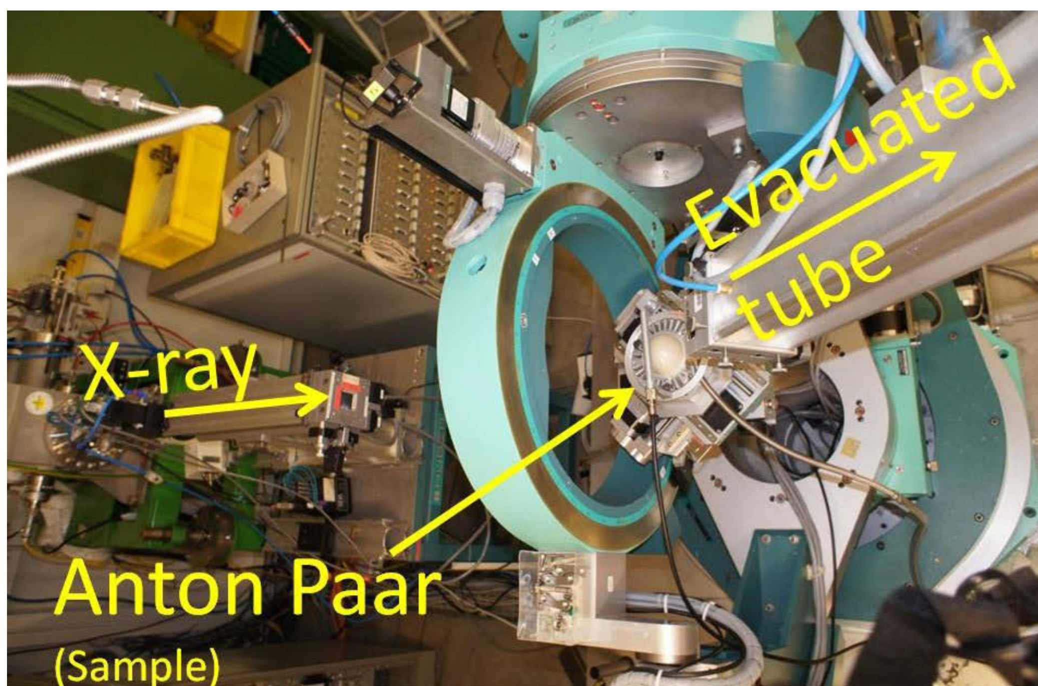

Figure 3.15: Experimental setup at BL-ROBL (BM20) at ESRF. A top view of 6-circles Huber goniometer equipped with one-dimensional linear position sensitive detector (PSD-50m-ASA, M. Braun with opening $50 \times 10\ (mm)$ at end of evacuated tube preventing scattering and absorption of the X-rays between sample and detector. Symmetric and asymmetric reflections together with grazing incidence X-ray diffraction (GI-XRD) were used to crystalline structure investigation and Fe-silicide formation during annealing process. The annealing was performed using Anton Paar DHS 900.

Home-lab setup

The XRR measurements have been performed with a high-resolution diffractometer GE HR-XRD 3003 with $Cu\ k\alpha$ radiation by laboratory setup. Some of XRR was measured using a 2D focussing Goebel mirror and sufficient small detector slits. The experimental XRR curves were simulated using the software RC_REF_SIM_win [17] which is based on the dynamical theory of X-ray reflection using the matrix approach [18] and roughness is considered following the Névot-Croce algorithm [19].

To achieve higher sensitivity and to evaluate the effect of implantation on the density of the damaged surface region, EAD in non-coplanar geometry was applied using the same instrument. A Bartels type monochromator was used to obtain $cu\ k\alpha 1$ radiation.

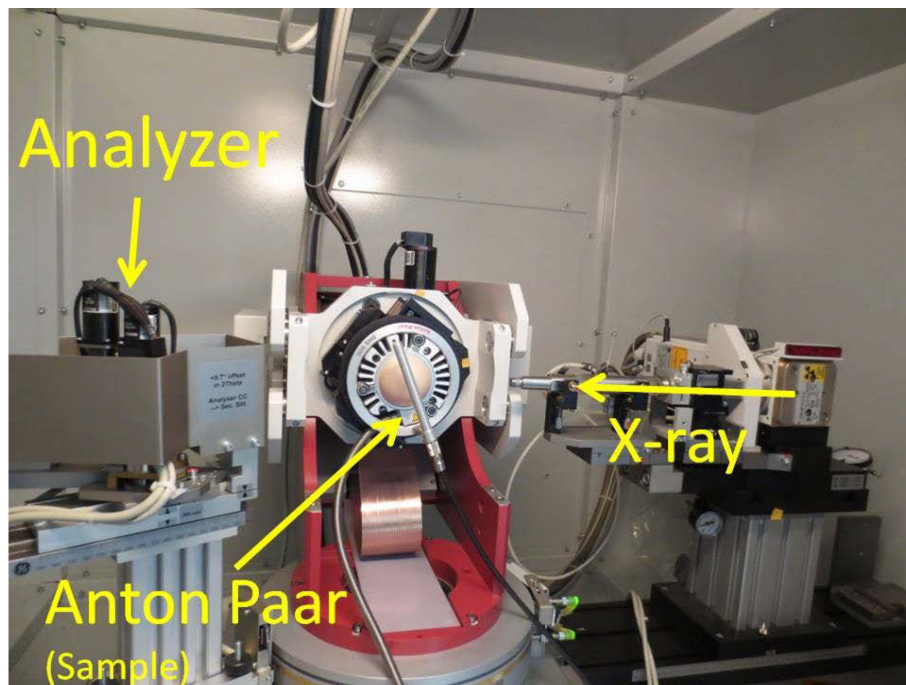

Figure 3.16: Experimental setup at hom-lab. A high-resolution diffractometer (GE HR-XRD 3003) with $cu\ k\alpha$ radiation and a 4-circle goniometer equipped with a PSD, analyzer and monochromator was used for X-ray reflectivity measurement and Si(331) reflection at extremely asymmetry non-coplanar geometry.

The measurements have been performed using a beam size of 1.5 × 1.5 mm² and an open detector without the use of an analyzer crystal. Rocking curves (RCs) of the Si (331) reflection were recorded at different fixed incidence angles in the range from 0° up to 1° using the HKL mode of SPEC [20]. For data evaluation, RCs of the Si (331) reflection were calculated using the GID-Sl code from *Sergey Stepanov* X-ray server base on dynamical diffraction theory (http://sergey.gmca.aps.anl.gov/). The setup of measurement is illustrated at Fig. 3.16.

The surface morphologies were analyzed ex-situ using a multimode atomic force microscope (Veeco) in tapping mode at HZDR and a Dimension 3000 system with Nanoscope IIIa controller from VEECO (former DIGITAL INSTRUMENTS) operating in Tapping Mode at IOM-leipzig. The AFM images presented in this report have a resolution of 512 × 512 pixels or higher and were performed using Si probes with (nominal) tip radii smaller than 7 nm. The roughness is extracted from the spatial height distribution. For the AFM processing WSxM was used [87].

In order to analyze locally the microstructure and the surface morphology of the Fe-irradiated Si samples as function of depth, cross-sectional transmission electron microscopy (TEM) investigations were performed using an image-corrected Titan 80-300 microscope (FEI) in HZDR. Employing a Gatan Imaging Filter 863, energy-filtered TEM (EFTEM) was used to study the chemical composition of the near-surface region of the samples. In particular, the Three-Window-Method was applied to extract the Fe and Si distributions. Classical cross-sectional TEM specimens were prepared by sawing, grinding, dimpling, and final Ar ion milling. Prior to each TEM analysis, the specimen mounted at a double tilt analytical holder was placed into a Model 1020 Plasma Cleaner (Fischione) for 45 s to remove organic contamination.

In addition, some of samples have been investigated by Rutherford backscattering spectrometry (RBS) and secondary ion mass spectrometry (SIMS) in HZDR and IOM-Leipzig. In particular, depth profiles of the atomic composition were obtained using dual beam time-of-flight secondary ion mass spectrometry (TOF-SIMS). 0.5 keV O_2^+ was used for erosion and 15 keV Ga^+ for analysis. The analysis area was 40 × 40 μm^2. According to the etching times and the final depths of the etched regions (determined by white light interferometry) depth profiles were obtained. The RBS measurements were performed at the nanoprobe LIPSION (the ion beam facility of the University of Leipzig) with a 2.0 MeV He^+ beam. The backscattered ions were

detected at an angle of 170° with a CANBERRA Annular (passivated implanted planar silicon) PIPS detector. For the data analysis the RUMP-code was applied [88].

4 Pattern formation on direct off-normal Fe ion irradiated Si(100) surfaces

In this chapter, we report on nanopattering on Si(100) surfaces under an off-normal irradiation process with energetic Fe ions. Depth resolved investigations using nondestructive X-ray methods were carried out to find out the effective parameters influencing the pattern formation mechanism. In section 4.1, the experimental parameters of the prepared sample are given. In section 4.2, the morphologies of the surfaces and interfaces under different irradiation parameters (ion energy and ion fluence), revealed by atomic force microscopy (AFM) and transition electron microscopy (TEM), are reported. In section 4.3, the ion beam induced variations in surface density using X-ray reflectivity (XRR) and extremely asymmetric diffraction (EAD) methods are represented.

4.1 Sample preparation

For this work, series of the samples have been prepared using the Danfysik 1050 low energy ion implanter at Helmholtz-Zentrum Dresden-Rossendorf. Two sides polished Si(100) wafers (nominally without miscut) with a size of (10 × 10 mm^2) and thickness of 500 µm were irradiated homogeneously with a scanned Fe^+ beam of 5 mm diameter. The irradiation parameters are summarized in table 4.1.

Table. 4.1 The parameters of ion energy, E_{ion}, ion fluence, φ_{ion}, ion incidence angle, α_{ion}, at Fe ion irradiation process on Si(100) surfaces.

Samples	E_{ion} (KeV)	Samples	E_{ion} (KeV)	φ_{ion} (ions cm^{-2})	α_{ion} (°)
1A	5	1B	20	1×10^{16}	65
2A	5	2B	20	5×10^{16}	65
3A	5	3B	20	1×10^{17}	65
4A	5	4B	20	5×10^{17}	65

4.2 Surface and interface morphology analysis

AFM analysis

The AFM analysis demonstrates the formation of variety of topographies on Si surfaces under Fe ion irradiation process. Figs. 4.1(a-d) show the AFM images of oblique bombarded Si surfaces with 5 KeV Fe ions (series A samples) with fluence of 1×10^{16} ions cm^{-2} (sample 1A), 5×10^{16} ions cm^{-2} (sample 2A), 1×10^{17} ions cm^{-2} (sample 3A), and 5×10^{17} ions cm^{-2} (sample 4A), respectively. While the surface remains smooth for the lower fluence (1A), the morphologies of the other samples changes from oriented chains (2A) over irregularly oriented ripples (3A) to short-distance ripples (4A). The extracted height histograms from AFM images of patterned samples are illustrated in Fig 4.1e from left to right hand side corresponding to samples 2A, 3A and 4A, respectively. The average height increases from 0.64 nm for the sample 1A to 4.41, 7.12 and 21.09 nm for the samples 2A, 3A, and 4A, respectively (Fig. 4.1e). For the height variation analysis of the resulted surface topographies, a statistically root mean square (RMS) parameter can be calculated from the height profiles from the AFM images by [89]:

$$\langle \boldsymbol{w} \rangle_{N} = \left\{ \frac{1}{N} \sum_{i=1}^{N} [\boldsymbol{h}_i - \langle \boldsymbol{h} \rangle_N]^2 \right\}^{0.5} \tag{4.1}$$

where $\langle \boldsymbol{h} \rangle$ is the average surface height, and N is the number of measured points.

It can be assumed that there is a correlation between the RMS roughness and the amplitude of the topographical features in surface topography with one dimensional length scale. The extracted RMS roughnesses from the AFM images are calculated to be σ_{1A} = 0.2 nm, σ_{2A} = 0.98 nm, σ_{3A} = 2.4 nm and σ_{4A} = 4.65 nm for the sample 1A, 2A, 3A, and 4A, respectively.

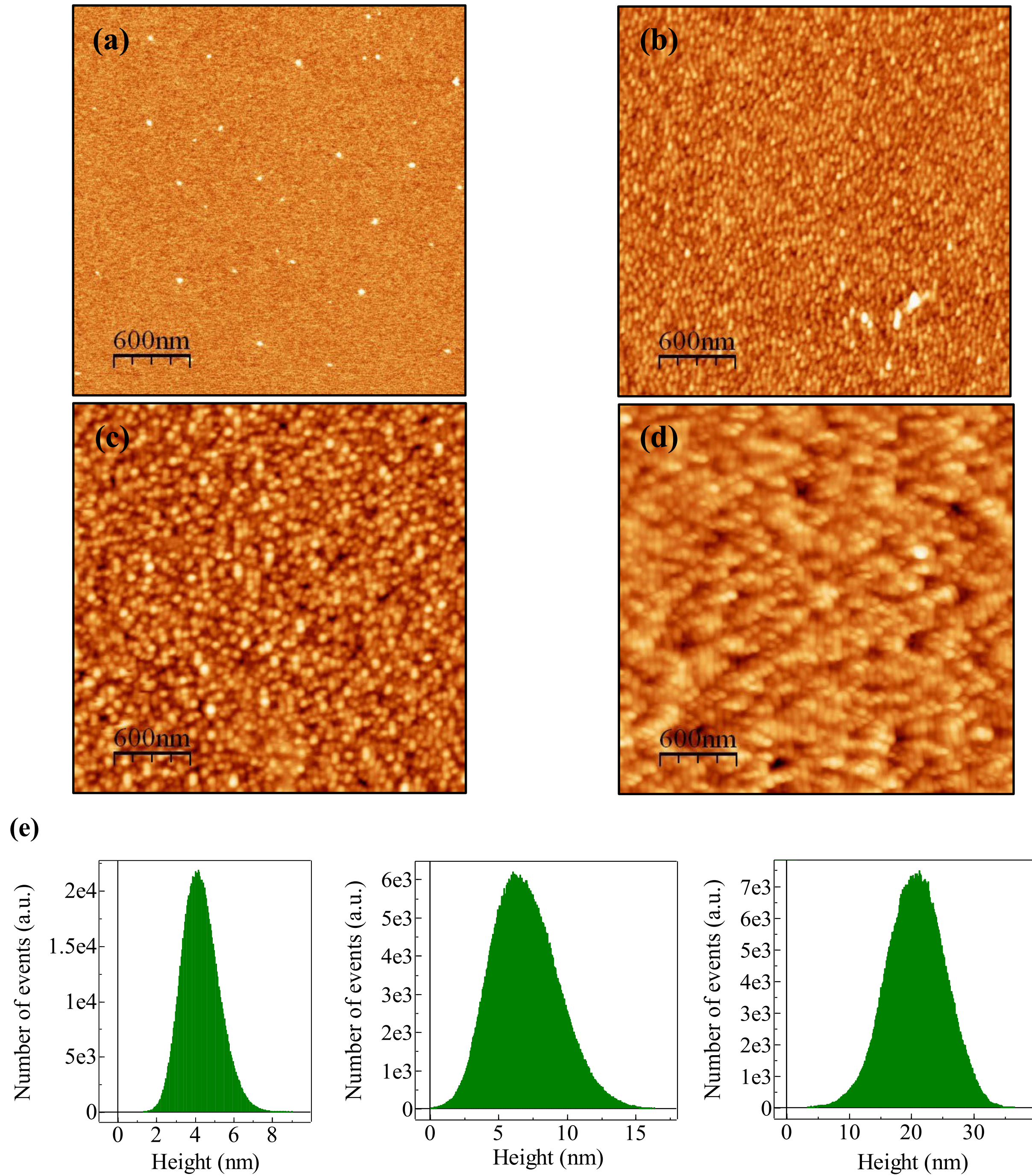

Figure 4.1: AFM images of Si surfaces irradiated with 5 keV Fe ions at 65° incidence angle with respect to the surface normal at different fluencies: (a) Sample 1A (z_{max} = 5.09 nm, RMS = 0.2 nm) at 1 × 10^{16} ions cm^{-2}. (b) Sample 2A (z_{max} = 14.65 nm, RMS = 0.98 nm) at 5 × 10^{16} ions cm^{-2}. (c) Sample 3A (z_{max} = 17.7 nm, RMS = 2.4 nm) at 1 × 10^{17} ions cm^{-2}. (d) Sample 4A (z_{max} = 41.39 nm, RMS = 4.65 nm) at 5 × 10^{17} ions cm^{-2}. The z is the height difference corresponding to the colour scale range. The images size is 3 × 3 μm^2. (e) Corresponding height histograms extracted from AFM images, ordered from left to right hand side for the samples 2A, 3A, and 4A.

The surface morphologies of the series B samples bombarded with 20 KeV Fe ions with fluences similar as series A samples are shown in Figs. 4.2(a-d). While for sample 1B the surface remains smooth, increasing the ion fluence for other samples causes modulation of surface morphologies in different way as shown in samples A, so that the surface morphologies change from random ripple like for the sample 2B over short range oriented ripples for the sample 3B to columnar like oriented nanodots for the sample 4B. The extracted RMS roughnesses from height profile of AFM images are σ_{1B} = 0.2 nm for the sample 1B, σ_{2B} = 2.3 nm for the sample 2B, σ_{3B} = 7.39 nm for the sample 3B, and σ_{4B} = 17.28 nm for the sample 4b.

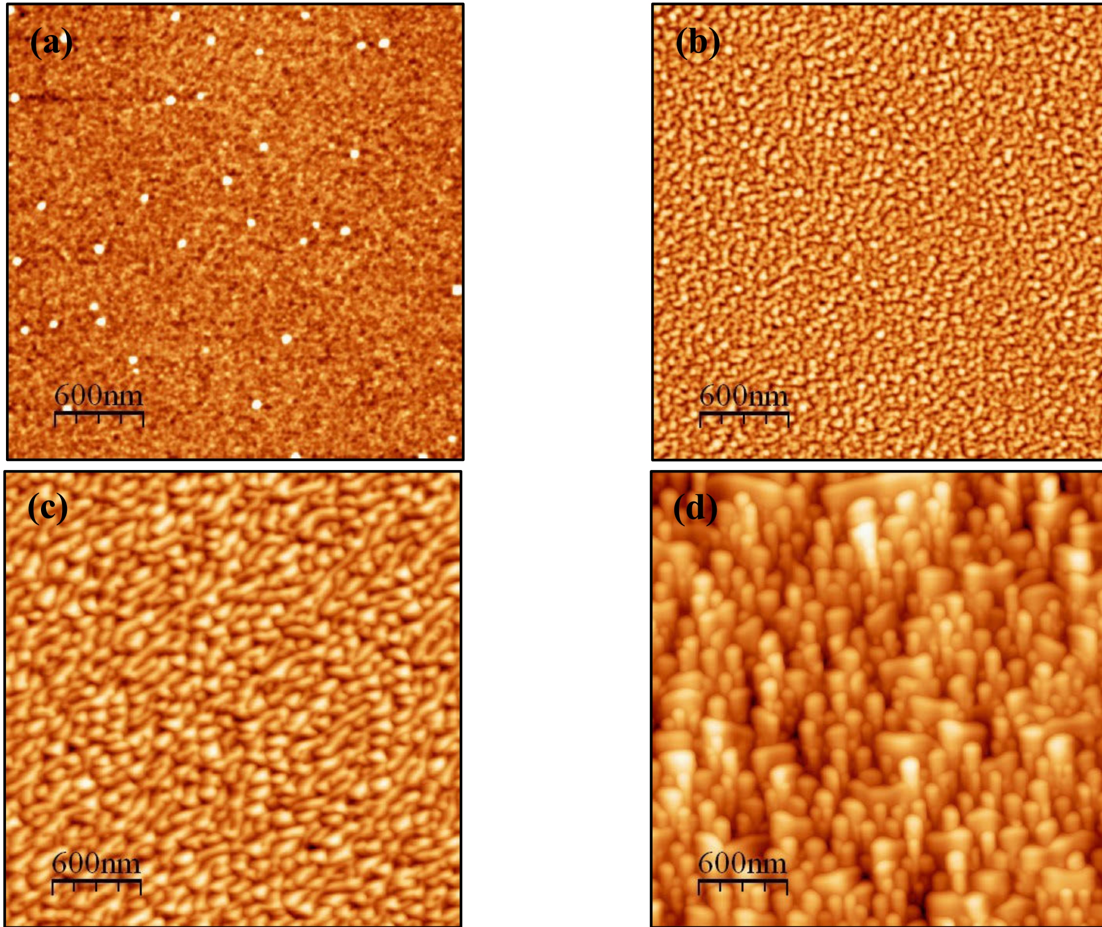

Figure 4.2: AFM images of Si surfaces irradiated with 20 keV Fe ions at 65° incident angle with respect to the surface normal at different fluencies: (a) Sample 1B (z_{max} = 2.5 nm, RMS = 0.2 nm) at 1 × 10^{16} ions cm^{-2}. (b) Sample 2B (z_{max} = 17.35 nm, RMS = 2.3 nm) at 5 × 10^{16} ions cm^{-2}. (c) Sample 3B (z_{max} = 53.52 nm, RMS = 7.39 nm) at 1 × 10^{17} ions cm^{-2}. (d) Sample 4B (z_{max} = 131.4 nm, RMS = 17.28 nm) at 5 × 10^{17} ions cm^{-2}. The z is the height difference corresponding to the colour scale range. The imagines size is 3 × 3 μm^2.

Fig. 4.3a shows the comparison between extracted RMS roughness as a function of ion fluence for the samples A (blue curve) and B (red curve). While for both series of the samples an onset of ion fluence for pattern formation is above the 1×10^{16} ions cm^{-2}, by increasing ion fluence the pattern amplitude increases exponentially for both series of the samples till ion fluence of 1×10^{17} ions cm^{-2} and after that the amplitude increases linearly with trend to saturation at higher ion fluences. This saturation can be attributed to dominant nonlinear effects at higher ion fluence and can not be predicted by BH model (see subsection 2.3). Furthermore, for the higher ion energy the pattern amplitude becomes larger at all ion fluences.

Fig. 4.3b shows the variation of average height with ion energy for ion fluences of 5×10^{16} ions cm^{-2} (black triangle line), 1×10^{17} ions cm^{-2} (red circle line), and 5×10^{17} ions cm^{-2} (blue rectangular line). It can be seen that the variation of the average height of the patterns at higher ion fluence strongly depends on ion energy. Therefore, the surface patterning process depends on ion fluence and ion energy as well.

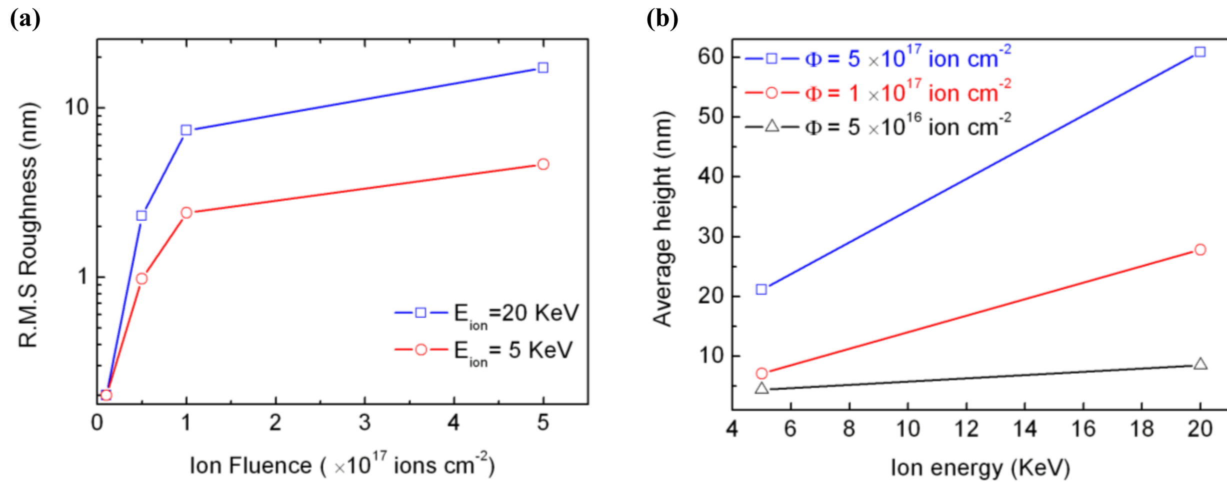

Figure 4.3: Root mean square (RMS) roughness as a function of ion fluence for the samples series A (blue) and series B (red). (b) Fluctuation of average height with ion energy at ion fluence 5×10^{16} ions cm^{-2} (black triangle line), 1×10^{17} ions cm^{-2} (red circle line), and 5×10^{17} ions cm^{-2} (blue square line).

As the RMS roughness is a first order statistical quantity which only reflects the properties of the individual points which give no information on lateral dimension of the patterns. For this, the second order statistical quantity as called the power spectral density (PSD), is used to characterize the relationship of two points or frequency properties of the topography on the surface. The PSD function is obtained by performing two Dimensional Fast Fourier Transform (2D-FFt) of the height profile from the AFM image. For instance, the FFT diagram corresponding to AFM image of sample 2B is illustrated in Fig 4.4a. The appeared rings indicate the existence of periodic component in the topography. From the position of first lighter rings at FFT image, characteristic frequency of periodic elements (the inverse of the separation of the features in the real space) can be obtained. The separation will be considered to be wavelength in the case of ripple and the mean size in the case of dots pattern. The width of the spots is related to the homogeneity and spatial correlation of features. To facilitate the quantification of the information presented in the FFT diagram, the calculated PSD function from the FFT image is shown in Fig. 4.4b. The position of the peak indicates the characteristic spatial frequency of the ripples in the real space (1/wavelength of the ripples) and provides quantitative information about height and lateral distributions.

Fig. 4.4c shows the calculated wavelength of surface pattern as a function of ion fluence for the series A (red) and B (blue) samples. It can be seen that the wavelength increases from 83 nm to 195 nm for the samples A and from 45 nm to 65 nm for the samples B when ion fluence increases from 5×10^{16} ions cm^{-2} to 5×10^{17} ions cm^{-2}.

Fig. 4.4d shows the variation of pattern wavelength versus ion energy for ion fluences of 5×10^{16} ions cm^{-2} (black triangle line), 1×10^{17} ions cm^{-2} (red circle line), and 5×10^{17} ions cm^{-2} (blue rectangular line). It seen that variation of pattern wavelength is more pronounced at 20 KeV ion energy compared to 5 KeV. The dependence of the lateral size of the ripples and dots pattern on ion energy and fluence represents a capability of pattern size controlling by means these ion parameters.

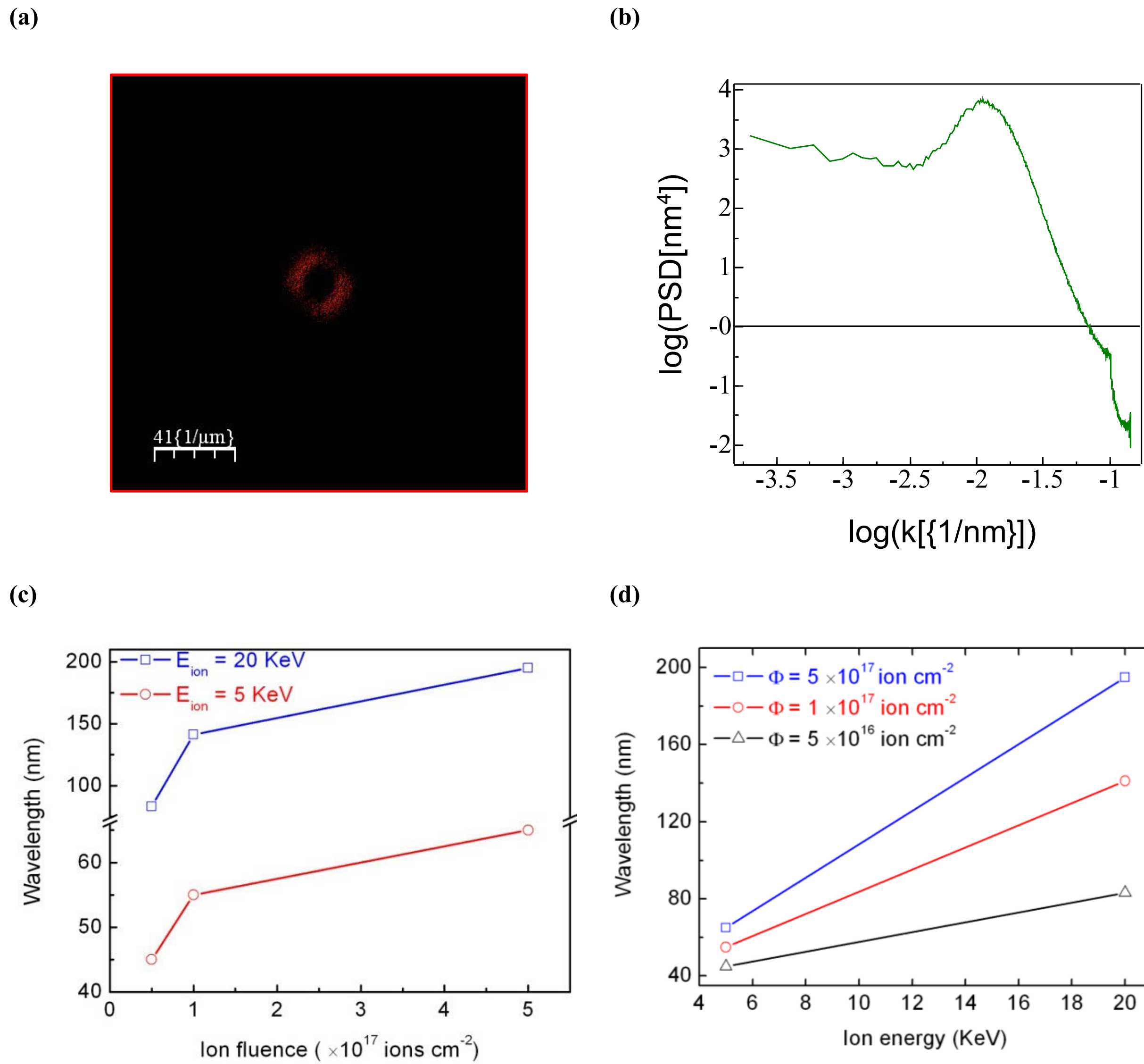

Figure 4.4 (a) Fast fourier transform (FFT) image corresponding to the sample 2B. (b) Power spectral density (PSD) diagram corresponded to FFT image of sample 2B. K is spetial frequency. (c) The variation of wavelength with ion fluence for ion energy of 5 KeV (samples series A-red) and 20 KeV KeV (samples series B-blue). (d) The variation of wavelength with ion energy at fluence of 5×10^{16} ions cm^{-2} (black), 1×10^{17} ions cm^{-2} (red), and 5×10^{17} ions cm^{-2} (blue).

TEM analysis

TEM analysis was applied to investigation of interface morphologies and evaluation of cross section of pattern geometries. Fig. 4.5 shows TEM images intersection of the sample series A ordering from top to down as increasing ion fluence from sample 1A to 4A, respectively. It can be seen while the surface remains smooth for the sample 1A irradiated with lower ion fluence, ripples form on surface for increasing ion fluence accompanied by increasing ripple wavelength, as shown by dashed vertical lines, from 45 nm for the sample 2A to 65 nm for the sample 4A over 55 nm for the sample 3A. It can be seen that the wavelength and amplitude of the ripples increase by increasing the ion fluence as were shown from AFM analysis.

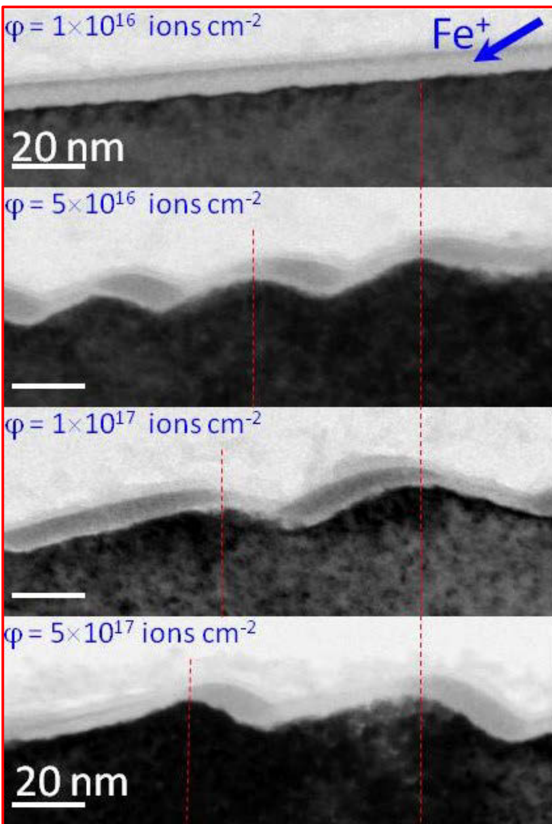

Figure 4.5: The cross-sectional TEM images of the Si surfaces after irradiation with 5 keV Fe ions at incidence angle of 65° with respect to the surface normal with a fluence of 1×10^{16} ions cm^{-2} (sample 1A), 5×10^{16} ions cm^{-2} (sample 2A), 1×10^{17} ions cm^{-2} (sample 3A), and 5×10^{17} ions cm^{-2} (sample 4A), from top to down, respectively. The dashed vertical lines show the variation of ripple wavelength with ion fluences. The blue array shows the direction of incoming Fe ions.

Fig. 4.6a shows a zero-loss filtered image of sample 1A. Directly below the glue, which is used for TEM sample preparation, an approximately 2 nm thick Si oxide surface layer (marked by two white dashed lines) is visible followed by a dark layer of 2 nm thickness which is marked by two dashed yellow lines. This is an Fe-rich film as confirmed by the Fe elemental map shown in Fig. 4.6b. Below this Fe-rich layer, the Fe concentration is decreasing towards the bulk. The structure of this 5 nm thick layer is still amorphous. Fig. 4.6c shows the Si element map of the sample 1A from same field of view as Fig. 4.6a. It can be seen that for low ion fluence the Si surface remains flat.

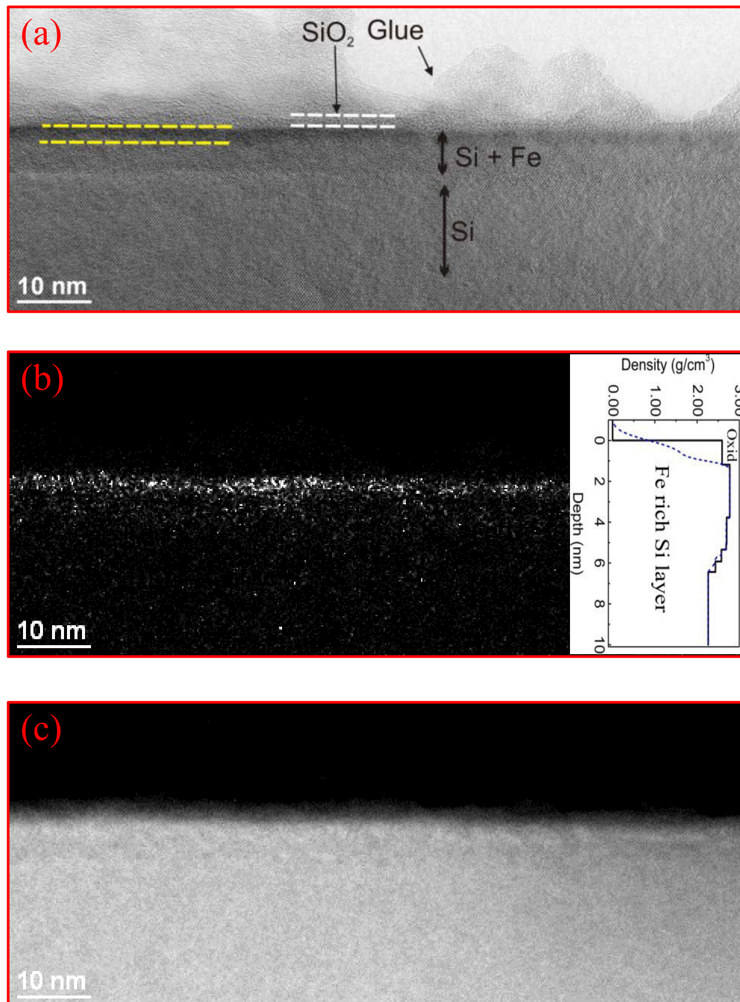

Figure 4.6: (a) The cross-sectional zero-loss filtered TEM images of the Si surface after irradiation with 5 keV Fe ions at incidence angle of 65° with respect to the surface normal with a fluence of 1×10^{16} ions cm^{-2} (sample 1A). Corresponding element map of (b) Fe and (c) Si from the same field of view. The inset shows the obtained depth density profile from X-ray reflectivity (see Fig. 4.8b).

Fig. 4.7a shows the cross-sectional zero-loss filtered image of sample 4A confirming the formation of ripples with an amplitude of ~ 10 nm on the Si(100) surface. Covered by glue from TEM sample preparation, the layer with bright contrast, which is marked by two white lines in Fig. 4.7a, corresponds to amorphous Si oxide. The dark ellipsoidal shaped areas at the front slopes of the ripples can be attributed to Fe-rich amorphous Fe-Si which is accompanied by few nanometer amorphous buried areas with decreasing Fe concentration towards the crystalline bulk Si (Figs. 4.7b-c). Derived from Fig. 4.7a, the ripple cross section shows an asymmetrical triangle with side angles of about 32° and 10° at the front slope, facing the incoming beam, and at the rear slope, respectively.

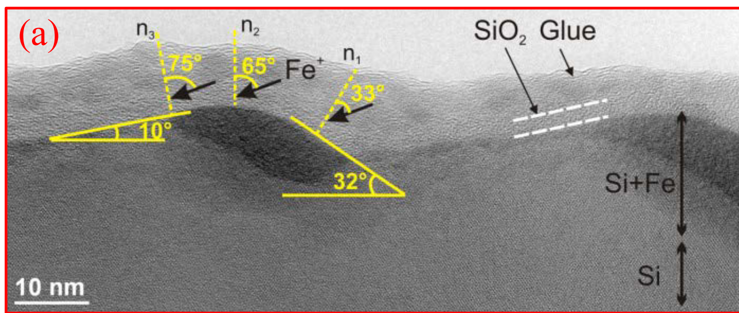

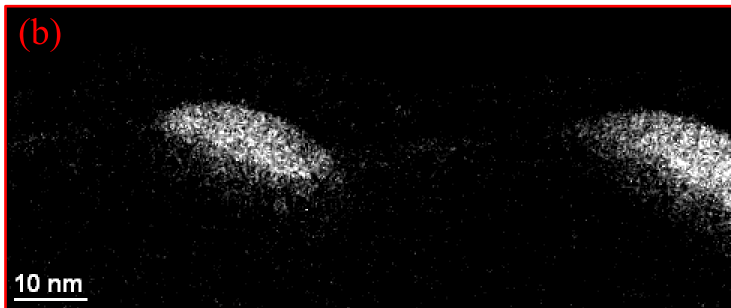

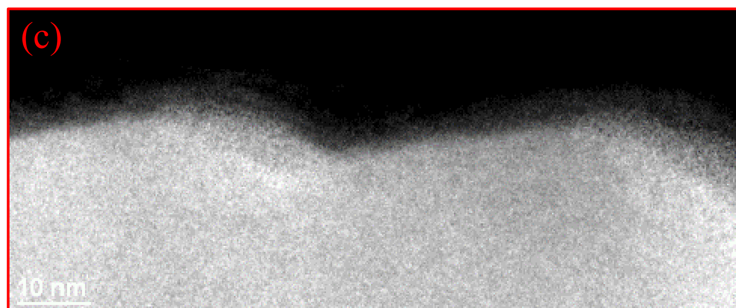

Figure 4.7: (a) The cross-sectional zero-loss filtered TEM images of the Si surface after irradiation with 5 keV Fe ions at incidence angle of 65° with respect to the surface normal with a fluence of 5×10^{17} ions cm^{-2} (sample 4A). Corresponding element map of (b) Fe and (c) Si from the same field of view.

The ion incident angle with respect to normal of the flat surface (n_2 in Fig 4.7a) is α_{ion} = 65°. From the ripple geometry, the local ion incidence angles with respect to the the normal of the front slope (n_1 in Fig. 4.7a) and rear slope (n_3 in Fig. 4.7a) are $\Theta_f = \alpha_{ion}$ - 32° =33° and $\Theta_r = \alpha_{ion}$ + 10° = 75°, respectively. The ion beam hitting the local surface at the front slope under 33° will penetrate deeper in the bulk than ions hitting the rear slope under 75°. Consequently, the Fe concentration is much higher at the thicker front slope compared to the thinner rear slope. By increasing the ion fluence, Fe atoms are accumulated in the crest of the ripples.

4.3 Depth density profiling of Si(100) after irradiation with Fe ions

4.3.1 X-ray reflectivity

The density profiles perpendicular to Fe ions irradiated Si surfaces were investigated using XRR. Fig. 4.8a shows the measured XRR curves of the samples 1A (black curve), 2A (red curve), 3A (blue curve), 4A (olive curve), and the non-irradiated Si (gray curve). For angles $\alpha_i > \alpha_c^{Si}$ = 0.23° (critical angle of Si at $Cu\ K\alpha$ radiation), the reflectivity of the sample 1A decreases with oscillations superimposed indicating a layering close to the surface. This layering is still visible for sample 2A but hard to see for the samples 3A and 4A. The mean density profile of the sample 1A in the direction of the surface normal was analyzed quantitatively by XRR. Fig. 4.8b shows the simulation of XRR curve of the sample 1A providing the relative density profile as a function of depth. To this end, the near surface region was divided into a number of thin lamellae with constant electron density. Both thickness and density of each lamella were varied until a coincidence between measured and simulated curves was reached.

The inset of Fig. 4.8b shows the fitted mean density profile as a function of depth. Close to the surface the mean density is found to be increased with respect to the non-irradiated silicon (2.33 g/cm^3), showing the incorporation of Fe ions close to the surface. The density reaches its maximum in a depth of 2 nm below the surface, while the total thickness of the layer with enhanced Fe atoms reaches 6 nm. The mean density of the irradiated region amounts to about 2.7 g/cm^3. The evaluated density profile is in qualitative agreement with TRIDYN calculations [90]. For an irradiation fluence that is larger than 1×10^{16} ions cm^{-2}, TRIDYN reveals a 3 nm sub-surface layer with an Fe concentration of 10 at % followed by a slow drop reaching zero value at

a depth of 10 nm. TRIDYN shows that above a certain fluence ($> 5\times10^{15}$ ions/cm^2) the Fe concentration saturates and is reaching a stable value. The onset of pattern formation should be above this threshold. However, TRIDYN does not take into account a surface roughening or pattering, while only the sputtering effect itself is taken into account. Note that this small ion penetration depth of a few nanometres only is comparable to the amplitude of surface corrugations induced by the ion beam processes at larger fluences found for samples 2-4A.

Fig. 4.8c shows the measured XRR curves of samples 1B (black curve), 2B (red curve), 3B (blue curve), 4B (olive curve), and the non-irradiated Si (gray curve). The reflectivity of sample 1B contains oscillations with less number and lower amplitude compared to the sample 1A consequently thinner layering close to surface with less density variation. Fig. 4.8d shows the simulated XRR curve of sample 1B providing the relative density profile as a function of depth. The inset of Fig. 4.8d shows the fitted density profile as a function of depth. The density reaches its maximum in a depth of 1 nm below the surface, while the total thickness of the layer with enhanced Fe atoms reaches 4 nm. The mean density of the irradiated region is calculated amounts to about 2.36 g/cm^3 that is in the range of the non-irradiated Si. An obtained smaller mean density for sample 1B compared to sample 1A can be attributed to the larger sputtering yield at sample 1B compared to sample 1A. The calculated sputtering yield using SRIM 2008 (www.SRIM.org) shows that the sputtering yield increases from 9.2 at 5 KeV ion energy (sample 1A) to 13.54 at 20 KeV ion energy (sample 1B). This 48% increasing at total sputtering yield can be related to smaller mean density at sample 1B.

For the XRR experiment, the larger surface roughness of the patterned samples series A and B leads to a strong reduction of the reflected intensity making a precise determination of the compositional profile and layer thickness impossible. In addition, the lateral height modulation counterweights the local increase in density due to the Fe incorporation, and no significant changes in (laterally averaged) surface mass density are observed. This is shown by the inset in Fig. 4.8a, showing the region around the critical angle in linear scale for samples A. Except for some small absorption effects and considering the experimental resolution of 0.005° there is no pronounced variation of the critical angle at different ion fluences. The same results at the vicinity of critical angles are observed for samples B, too. It shows that the densities averaged

over a depth of 34 nm (penetration depth of X-rays at α_c^{Si}) for the patterned surfaces are almost constant.

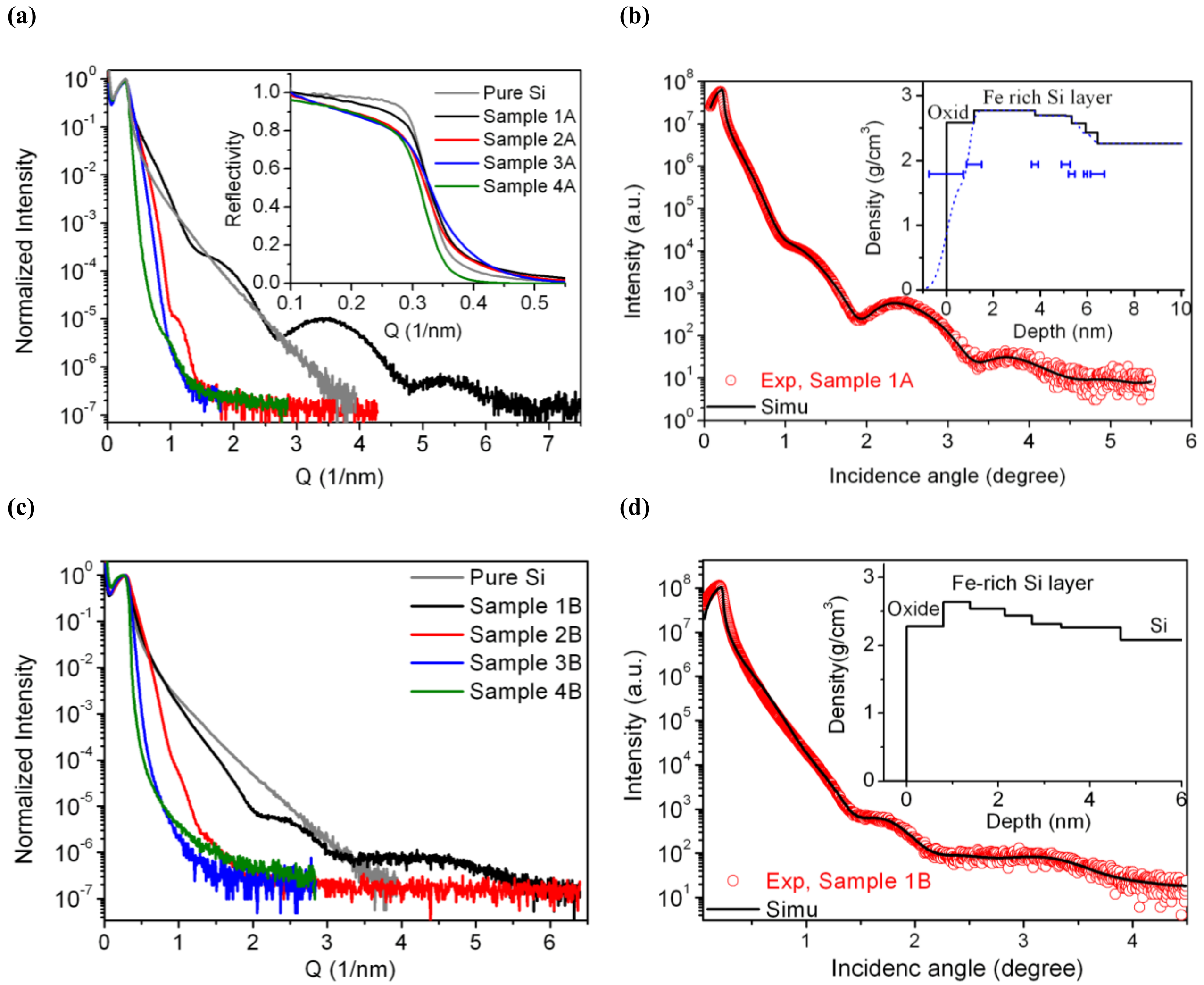

Figure 4.8: (a) The measured specular X-ray reflectivity (λ = 1.54 Å) of the samples 1A (black), 2A (red), 3A (blue), 4A (olive), and non-irradiated Si (gray). For clarity, a magnification of the region α_i < 0.4° on the linear scale considered by footprint correction is shown in the inset, where the critical angles of the samples are visible. (b) The measured (open circles) and calculated (solid line) specular X-ray reflectivity of the sample 1A. The insert shows the density profile (box model) as a function of depth; the blue dotted curve shows this profile taking into account the interface/surface roughness (horizontal blue lines). (c) The measured specular X-ray reflectivity of the samples 1B (black), 2B (red), 3B (blue), 4B (olive), and non-irradiated Si (gray). (d) The measured (open circles) and calculated (solid line) specular X-ray reflectivity of the sample 1B. The insert shows the density profile as a function of depth.

Obviously, the density variations caused by the ion beam irradiation are limited to a very thin surface layer which thickness is much smaller than the minimum penetration depth of XRR. In the next section we will show that the EAD method (see 3.3.3) can be applied to achieve a higher sensitivity to clarification of different critical angles and evaluation of variation in surface densities.

4.3.2 Extremely asymmetric diffraction with changing scattering geometry

The method (see subsection 3.3.3) is demonstrated at the samples 1A and 1B with smooth surfaces, and the sample 4A and 4B with pattern surfaces and for a non-irradiated Si as a reference. Rocking curve (RC) measurements have been performed at the asymmetric Si (331) reflection in non-coplanar scattering geometry with α_i varying between 0° and 1°. Due to the small incidence angles, the X-ray beam simultaneously illuminates the surface of the sample as well as the sample's edge, leading to splitting of the RC in a reflection signal originating from the edge, and a separate signal from the surface of the sample, which is affected by refraction effects according to Eq. 3.30.

Fig. 4.9a shows the RCs for the sample 1A at $\alpha_i = 0.46$ ° (olive), $\alpha_i = 0.2$° (blue), α_i = 0.06° (red) and $\alpha_i = 0.02$° (black). Each RC shows two peaks: the intense sharp peak at the left side which corresponds to a Si (331) reflection where the X-ray beam penetrates through the edge of the sample and a broader peak at the right side which corresponds to the reflection from the surface. The increasing peak separation with decreasing α_i is due to the increase of dynamical Bragg peak shift. Since the refraction effects for the "edge peak" are small and constant, this peak stays fixed and can be used as a reference for the evaluation of the measured shift of the surface peak. It can be seen that simultaneously with the deviation of the Bragg peak from the kinematical position, the intensity of the surface peaks drops exponentially by reducing α_i due to an exponentially reduction of the penetration depth and hence the probed volume (see Fig. 3.7b). As discussed in subsection 3.2.2, the deviation from the kinematic Bragg angle position tends towards α_c when the incidence angle approaches zero. This can be seen in Fig. 4.9b, showing the map of corresponding RCs versus α_i and Bragg shifts ($\Delta\theta_B$) for sample 1A.

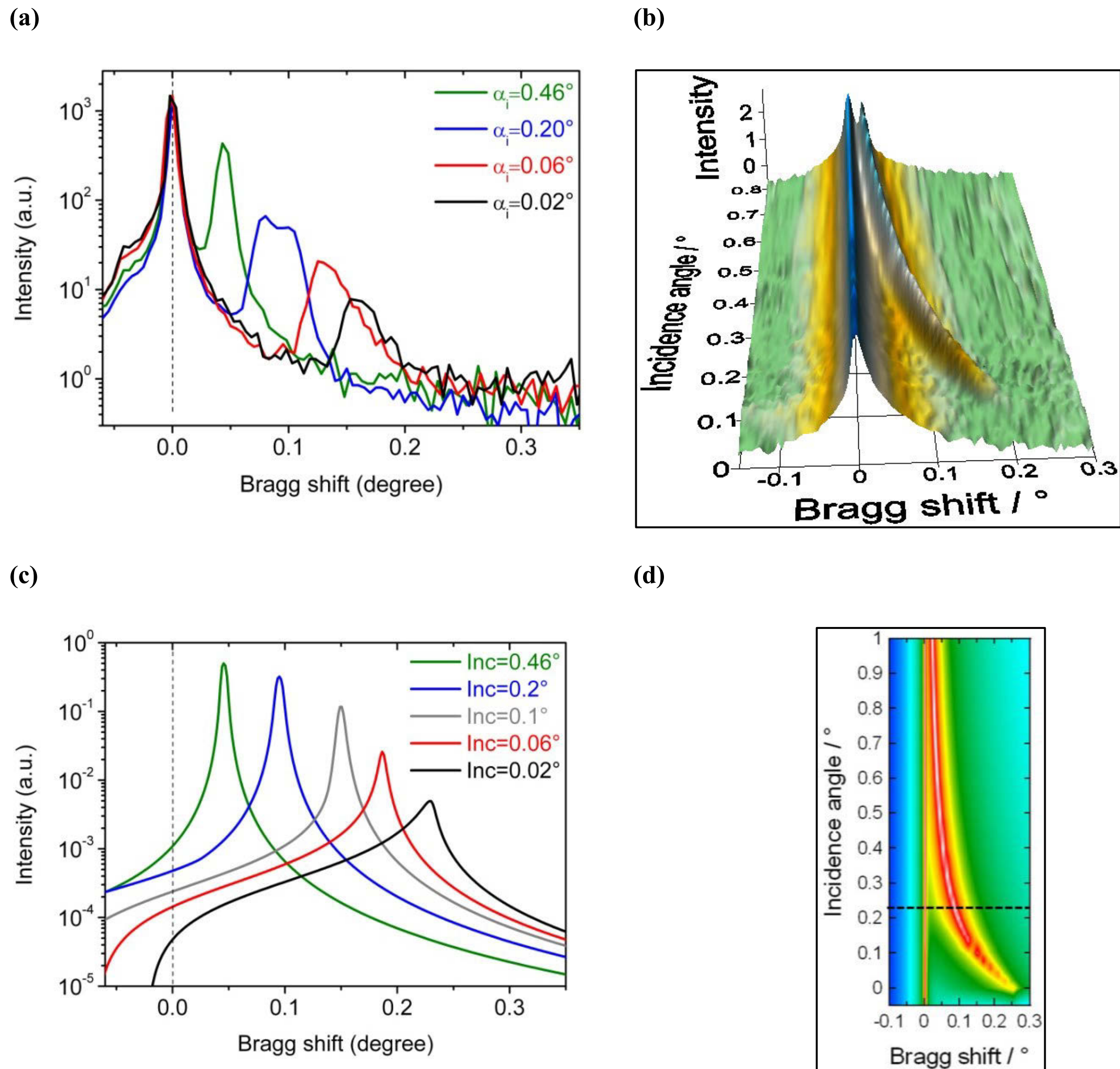

Figure 4.9: Deviation from Bragg's angle of Si (331) reflection in non-coplanar scattering geometry using $Cu\ K\alpha$: (a) The measured Rocking curves (RCs) of Si (331) reflection versus Bragg peak shift ($\Delta\theta_B$) for the sample 1A at different incidence angles of α_i = 0.46° (olive), α_i = 0.2° (blue), α_i = 0.06° (red) and α_i = 0.02° (black). (b) The corresponding map of the measured RCs versus α_i and $\Delta\theta_B$. (c) The calculated RCs of Si (331) reflection versus Bragg peak shift ($\Delta\theta_B$) for pure Si at different incidence angles ranging from 0° to 0.46°. (d) The projection of the map of the calculated RCs versus α_i and $\Delta\theta_B$. The dashed horizontal line shows the position of critical angle of total external reflection for Si ($\alpha_c^{Si} = 0.22°$). The RCs were calculated using *Sergey Stepanov* X-ray server.

The intense sharp straight peak fixed at the zero position of Bragg shift corresponds to the edge reflections and the broader line with increasing peak separation corresponds to the reflections

from the surface. It can be seen that by reducing α_i from 1° towards 0°, Bragg shift is increasing accordingly and tends to α_c =0.22°

Fig. 4.9.c shows the calculated RCs of Si (331) reflection at λ = 1.54 Å for pure Si(100) using *Sergey Stepanov* X-ray server base on dynamical theory of X-ray diffraction. The calculated RCs α_i = 0.46 ° (olive), α_i = 0.2° (blue), α_i =0.06° (red) and α_i = 0.02° (black) are in good agreement with measured ones (Fig. 4.9.a). A vertical dashed line at zero position of Bragg shift is corresponded to the position of calculated quasi-symmetric Si (331) reflection indicating the "edge peak". Corresponding RCs map in Fig 4.9d shows a variation of Bragg peak position with respect to the fixed edge peak as a function of incidence angle. When $\alpha_i \rightarrow 0°$, then $\Delta\theta_B \rightarrow \alpha_c$.

Qualitatively, all the samples show the same behaviour, but the amount of peak separation differs as a function of irradiation parameters. Particularly in the case of low ion energy, these differences become measurable if α_i becomes smaller than α_c. Fig. 4.10a shows a comparison between the RCs for the sample 1A (red), 4A (blue) and non-irradiated Si (black) at incidence angle of α_i =0.02°. It can be seen that the deviation from the Bragg peak position decreases from the non-irradiated Si over sample 1A to sample 4A. Following Eq. (3.30), this different shift can be attributed to a reduction of the density (represented by χ_0) caused by the increasing irradiation fluence. These findings are supported by our calculations in terms of advanced dynamical theory (see Fig. 3.4a). For a quantitative analysis of the density variations we fitted the measured Bragg peak shifts according to Eq. (3.30).

Fig. 4.10b shows the measured (open circle) and calculated (solid lines) dynamical Bragg peak shifts ($\Delta\theta_B$) versus α_i for samples 1A (red), 4A (blue) and non-irradiated Si (black). Note that the data differ only significantly for $\alpha_i < \alpha_c$ and hence for very small penetration depths. The fitting of the Bragg peak shifts for incidence angles below the critical angle reveals the polarizabilities of χ_0^{1A}= 13.5 × 10^{-6} and χ_0^{4A} = 11.5 × 10^{-6} for the samples 1A and 4A, respectively. These values correspond to a surface density of ρ_{1A}= 2.11 g/cm^3 and ρ_{4A}= 1.79 g/cm^3, which are 13% and 26% smaller than the measured value for non-irradiated Si with χ_0^{Si} = 15.5 × 10^{-6} and ρ_0= 2.32 g/cm^3.

Fig. 4.13c shows the variation of the full width of half maximum (FWHM) of RCs as a function of α_i for the samples 1A (red), 4A (blue) and the non-implanted Si (black). According to the advanced dynamical theory, in EAD geometry, Darwin width (DW) increases with decreasing incidence angle and passes through a maximum when $\alpha_i \rightarrow \alpha_c$ (see Eq. 3.31). The different positions of the peak maximum can be attributed to different surface densities caused by the ion irradiation. The maximum of the FWHM shifts by about 0.02 (10%) degree for sample 1A and 0.04 (20%) degree for sample 4A compared to α_c = 0.22° for the non-implanted Si. These values are in good agreement with the observed dynamical Bragg peak shifts.

Both approaches demonstrate that in all samples density modifications are present very close to the surface. This modified surface density is only accessible for incidence angles $\alpha_i < \alpha_c^{Si}$ (bulk silicon). Only at these small incidence angles a variation of the Bragg peak shift as a function of the ion-fluence was found. For $\alpha_i > \alpha_c^{Si}$ all samples behave in similar way, i.e. there is no variation of the Bragg peaks shift.

The access to very small incidence angles makes the EAD method extremely surface sensitive. This is in contrast to XRR where the average electron density value can be directly extracted from the angular position of α_c. However this value is averaged over the penetration depth that is not well defined at α_c (see Fig.3.7b). In an experiment, the correct determination of α_c is quite complicated. Considering the relation $\alpha_c \approx \sqrt{2\delta}$, 10% inaccuracy in the determination of α_c leads to a roughly 20% inaccuracy in the value of the material density. Diffraction, on the other hand, takes place also at very shallow angles providing sensitivity for tiny changes in the refractive index even at very low penetration depths. Here, the electron density value follows directly from the Bragg peak shift $\Delta\theta_B$ measured as a difference with respect to the angular position of the quasi non-shifted “edge peak” providing a much higher accuracy of density determination compared to XRR on an absolute scale.

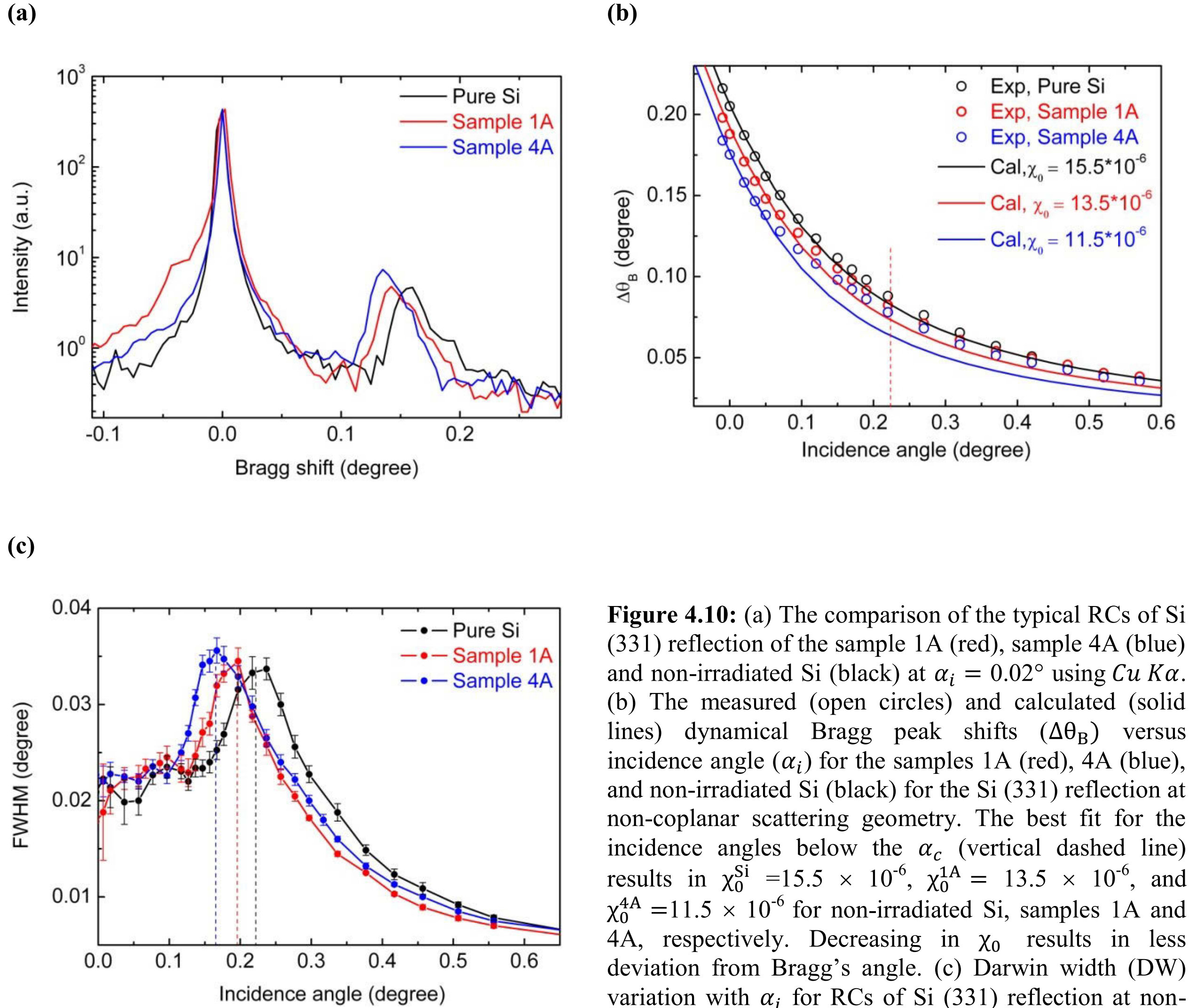

Figure 4.10: (a) The comparison of the typical RCs of Si (331) reflection of the sample 1A (red), sample 4A (blue) and non-irradiated Si (black) at $\alpha_i = 0.02°$ using $Cu\ K\alpha$. (b) The measured (open circles) and calculated (solid lines) dynamical Bragg peak shifts ($\Delta\theta_B$) versus incidence angle (α_i) for the samples 1A (red), 4A (blue), and non-irradiated Si (black) for the Si (331) reflection at non-coplanar scattering geometry. The best fit for the incidence angles below the α_c (vertical dashed line) results in $\chi_0^{Si} = 15.5 \times 10^{-6}$, $\chi_0^{1A} = 13.5 \times 10^{-6}$, and $\chi_0^{4A} = 11.5 \times 10^{-6}$ for non-irradiated Si, samples 1A and 4A, respectively. Decreasing in χ_0 results in less deviation from Bragg's angle. (c) Darwin width (DW) variation with α_i for RCs of Si (331) reflection at non-coplanar geometry: The variation of measured (dot-line) FWHM of RCs with α_i for the non-irradiated Si (black), sample 1B (red), sample 4B (blue). The vertical dashed lines show the position of the critical angles.

In the presented case, the density reduction at the sample surface that increases with ion fluence can be explained by the high surface roughness induced by the pattern formation. From AFM analysis we know that the amplitudes of the patterns increase with increasing ion energy and ion fluence (see Fig. 4.3). This leads to a reduction of the laterally averaged density in the surface

layer, although a considerable amount of Fe is incorporated. The observed net reduction of the surface density of sample 1A leads to the conclusion that the process of pattern formation could be already started at a Fe fluence of ~ 10^{16} ions cm^{-2}. At this early stage of pattern formation surface roughening and the amorphization of silicon, that is also known to reduce the density further by about 2% [91], are the main effects.

The net reduction of the surface density was examined for the samples irradiated with low ion energy of 2 KeV with low ion fluences of 5×10^{14} ions cm^{-2} (less than 1ML) and 5×10^{16} ions cm^{-2}, named as samples 1C and 4C.

Fig. 4.11(a-b) shows the AFM images of the samples 1C and 4C, respectively. The RMS roughness varies from 0.2 nm for the sample1C to 0.96 nm for the samples 4C.

Fig. 4.11c shows a comparison between the RCs of Si(331) reflection for the samples 1C (red curves) and 4C (blue curves) at typical incidence angles of 0.45° (square-line), 0.2° (triangle-line) and 0.02° (circle-line). It can be seen that by decreasing incidence angle the deviation from the Bragg peak position decreases from the sample 1C to sample 4C.

Fig. 4.11d shows the variation of the measured Bragg shift as a function of incidence angle for the sample 4C (open blue circles) and samples 1C (open red circles) and non-irradiated Si (open black circles). For the sample 1C with smooth surface, variation of the Bragg shift with incidence angle is almost the same as non-irradiated Si. This implies that there is a threshold value of ion fluence for surface density modulation. For the sample 4C, the amount of Bragg shift is smaller than non-irradiated Si when the incidence angles falls below the critical angle. The fit of the calculated solid curve (blue curve) for angles below the critical angles give raise to χ_0^{4c} = 12.47×10^{-6} for the sample 4C which is correspond to a surface density of ρ_{4C}= 1.95 g/cm^3 (16 % smaller than non- irradiated Si with ρ_0= 2.32 g/cm^3).

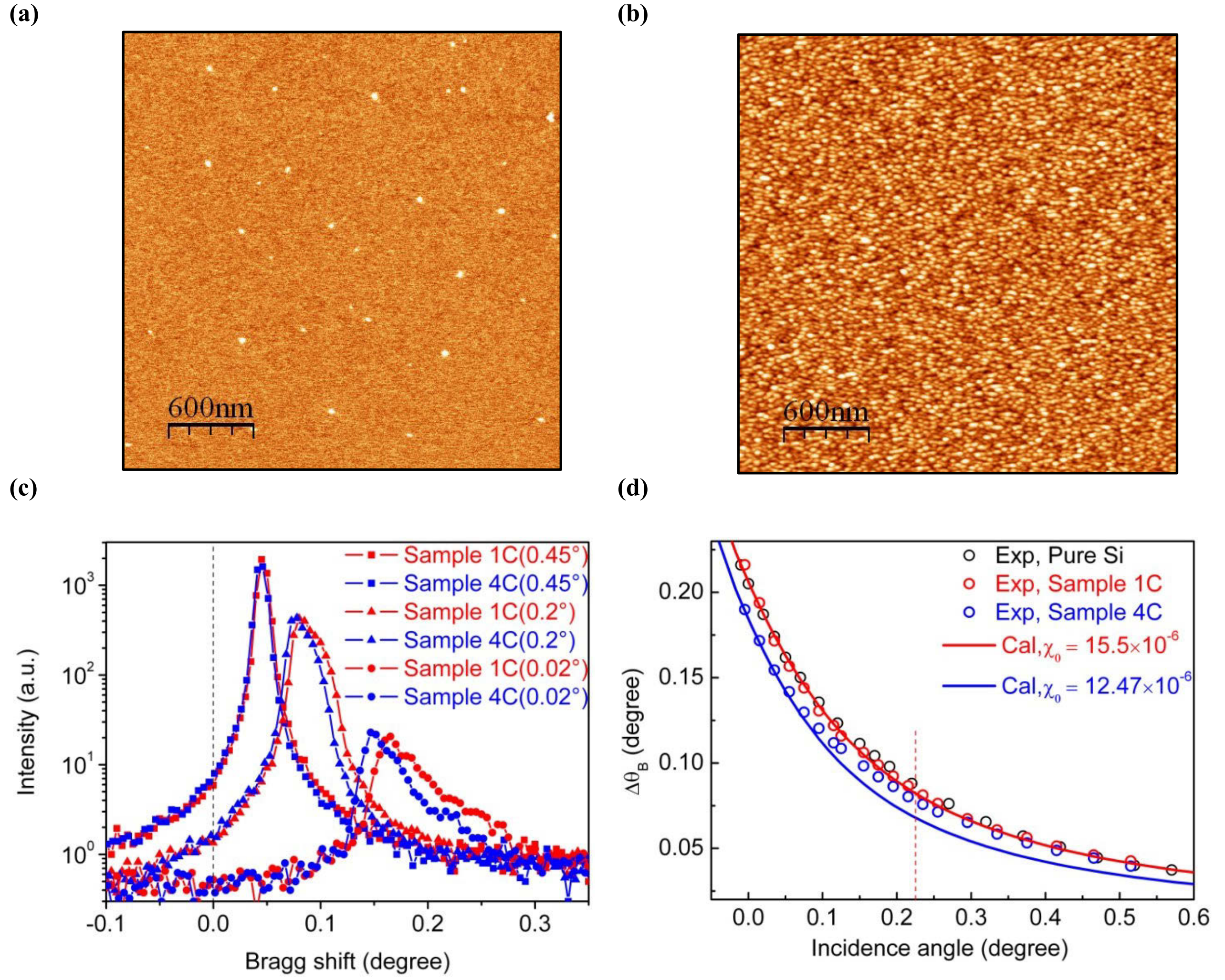

Figure 4.11: AFM images of Si surfaces irradiated with 2 keV Fe ions at 65° incident angle with respect to the surface normal at different fluences: (a) Sample 1C (z_{max} = 4.0 nm, RMS = 0.28 nm) at 5 × 10^{14} ions cm^{-2}. (b) Sample 4C (z_{max} = 8.2 nm, RMS = 0.96 nm) at 5 × 10^{16} ions cm^{-2}. The z is the height difference corresponding to the color scale range. The imagines size is 3 × 3 μm^2. (c) The comparison of the typical RCs of Si (331) reflection of the sample 1C (red), sample 4C (blue) at $\alpha_i = 0.45°$ (cubic-line), $\alpha_i = 0.2°$ (triangle-line), and $\alpha_i = 0.02°$ (circle-line) using $Cu\ K\alpha$. (d) The measured (open circles) and calculated (solid lines) dynamical Bragg peak shifts ($\Delta\theta_B$) versus α_i for the samples 1C (red), 4C (blue), and non-irradiated Si (black) for the Si (331) reflection at non-coplanar scattering geometry. The best fit for the incidence angles below the α_c (vertical dashed line) results in χ_0^{Si} = χ_0^{1C} =15.5 × 10^{-6}, and χ_0^{4C} =12.47 × 10^{-6} for non-irradiated Si, samples 1C and 4C, respectively. Decreasing in χ_0 results in less deviation from Bragg's angle.

4.3.3 Extremely asymmetric diffraction with changing the wavelength

The alternative method to achieve EAD is tuning the photon energies at fixed coplanar scattering geometry (see subsection 3.3) [92]. This method also was applied for the samples 1A, 4A and non-irradiated Si as a reference. In order to get Si (311) reflection in EAD geometry, the photon energies have been chosen in the range of 8550 eV up to 8875 eV providing the incidence angle of X-ray on the surface between 1° and 0°. Due to the small incidence angles, the X-ray beam simultaneously illuminates the surface of the sample as well as the sample's edge. Fig. 4.12a shows the RCs for the sample 4A at $h\nu$ = 8715 eV (black), $h\nu$ = 8810 eV (magenta), $h\nu$ = 8840 eV (olive), $h\nu$ = 8860 eV (red) and $h\nu$ = 8875 eV (blue). Each RC consist of an intense sharp peak at zero position of Bragg shift axis which corresponds to a Si (311) reflection where the edge of the sample is illuminated and a broader peak at the right side which corresponds to the reflection from the surface. With increasing photon energy consequently decreasing α_i (see Fig. 3.7d), the surface peak starts to shift from kinematical Bragg angle and tends towards α_c at higher energies due to the increase of dynamical Bragg peak shift (Eq. 3.30). The "edge peak" is used as a reference for the evaluation of the measured shifts of the surface peaks. Concurrent with the deviation from Bragg's angle, the intensity of the surface peaks drops exponentially by increasing photon energy due to an exponentially reduction of the penetration depth (Fig. 3.7b).

Fig. 4.12b shows the map of corresponding measured RCs versus wavelength and the shift in z component of scattering vector (ΔQ_z) for sample 1A. The intense sharp straight peak fixed at the zero position of ΔQ_z corresponds to the "edge peak" and the broader line with increasing peak separation corresponds to the reflections from the surface. It can be seen that by decreasing wavelength from λ = 1.45 nm ($h\nu$ = 8550 eV) to λ = 1.397 nm ($h\nu$ = 8875 eV) resulting in a decrease in incidence angle from 1° to 0°, ΔQ_z increases accordingly. When the wavelength becomes smaller than λ = 1.408 nm ($h\nu$ = 8805 eV), incidence angle becomes below the critical angle (α_c^{Si} = 0.22°), as shown by vertical dashed line, and ΔQ_z becomes measurable. Fig. 4.12c shows the calculated RCs of Si (331) reflection at λ = 1.4238 nm ($h\nu$ = 8715 eV) to λ = 1.407 nm ($h\nu$ = 8810 eV), λ = 1.4027 nm ($h\nu$ = 8840 eV), λ = 1.3995 nm ($h\nu$ = 8860 eV), for pure Si(100) using *Sergey Stepanov* X-ray server base on dynamical theory of X-ray diffraction with black, magenta, olive, red, and blue curves, respectively.

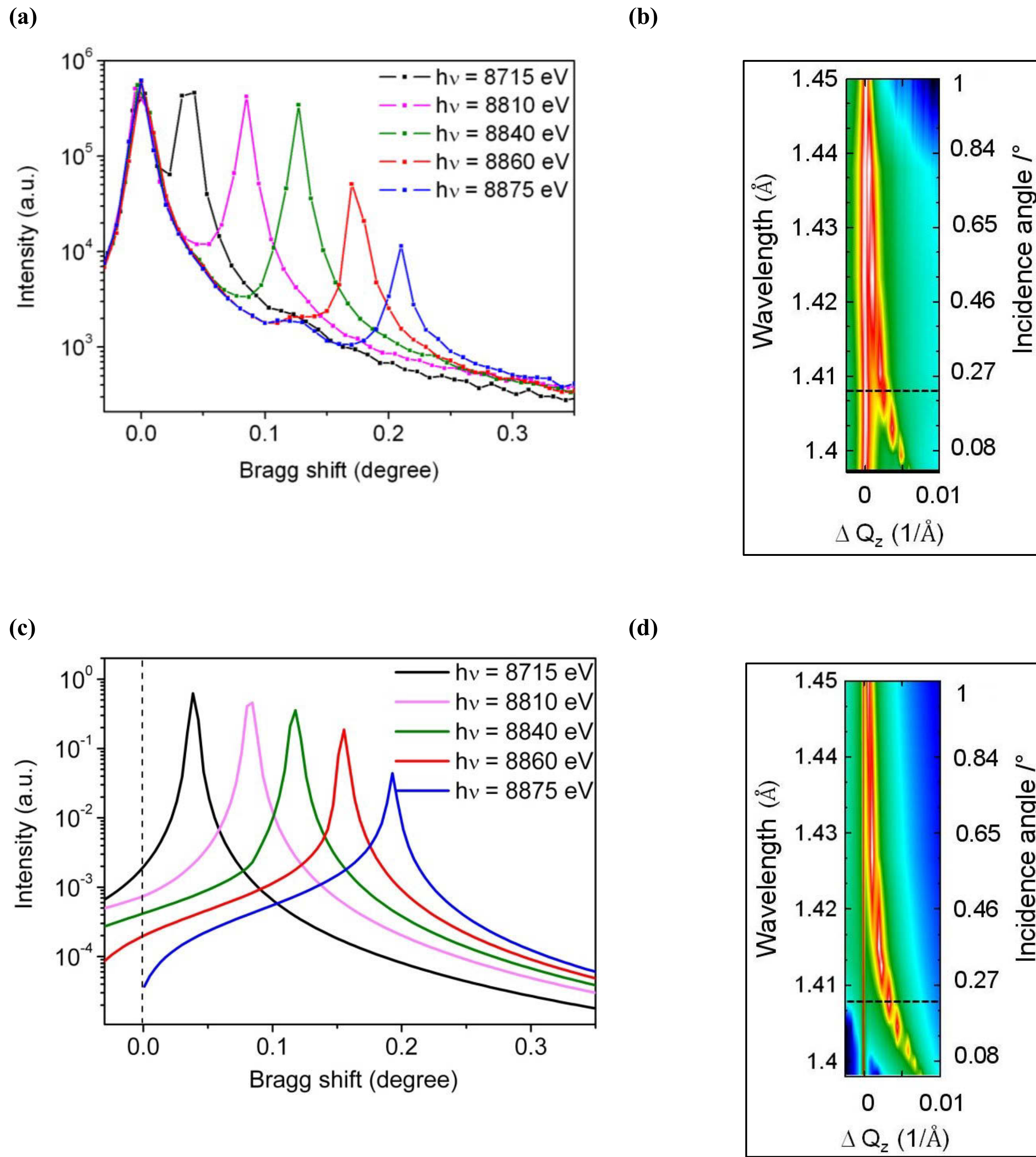

Figure 4.12: Deviation from Bragg's angle of Si (311) reflection in coplanar scattering geometry by changing X-ray wavelength: (a) The measured rocking curves (RCs) of Si (311) reflection versus Bragg peak shift ($\Delta\theta_B$) for sample 1A at different photon energies of $h\nu = 8715$ eV (black), $h\nu = 8810$ eV (magenta), $h\nu = 8840$ eV (olive), $h\nu = 8860$ eV (red), and $h\nu = 8875$ eV (blue). (b) The corresponding map of the measured RCs versus wavelength/incidence angle and z component of scattering vector (Q_z). (c) The calculated RCs of Si (311) reflection versus Bragg peak shift ($\Delta\theta_B$) for Si at different photon energies ranging from 8715 eV to 8875 eV as inset using *Sergey Stepanov* X-ray server base on dynamical diffraction theory. (d) The corresponding map of the calculated RCs versus wavelength/incidence angle and z component of scattering vector (ΔQ_z).

A vertical dashed line at the left side is corresponded to position of edge reflection. It can be seen that there is a good agreement between calculated curves and measured ones (Fig. 4.12.a).

The Fig. 4.12d shows the map of corresponding calculated RCs versus wavelength and the shift in z component of scattering vector (ΔQ_z) for pure Si at 311 reflections. The dashed line fixed at the zero position of ΔQ_z corresponds to the “edge peak” position and the broader line with increasing peak separation corresponds to the reflections from the surface. By decreasing wavelength (reducing α_i), ΔQ_z increases and when the wavelength becomes closer to value correspond to critical angle (λ = 1.408 Å) ΔQ_z becomes pronounced.

Fig. 4.13a shows a comparison between the measured RCs for the samples 1A (red), 4A (blue) and non-irradiated Si (black) at $h\nu$ =8840 eV (α_i = 0.08°). It can be seen that the deviation from the Bragg peak position decreases from the non-irradiated Si over sample 1A to sample 4A caused from reduction of the surface density. Quantitatively, these density variations can be determined by fitting the measured Bragg peak shifts according to Eq. (3.30). Fig. 4.13b shows the measured (open circle) and calculated (solid lines) dynamical Bragg-peak shifts ($\Delta\theta_B$) versus X-ray wavelength/incidence angle for the samples 1A (red), 4A (blue) and non-irradiated Si (black). After calibrated to $Cu\,K\alpha$ radiation, the fitting of the peak shifts reveals the polarizabilities of χ_0^{1A} = 13.49 × 10^{-6} and χ_0^{4A} = 11.48 × 10^{-6} for the samples 1A and 4A, respectively. These values are in good agreement with obtained results for the samples using EAD at non-coplanar scattering geometry for Si (331) reflection (see subsection 4.3.2).

Fig. 4.13c shows a comparison between the measured RCs for the samples 1C (red) and 4C (blue) and non-irradiated Si (black) at $h\nu$ =8875 eV (α_i = 0.02°). While there is no pronounced change in Bragg shift deviation of sample 1C compared to non-irradiated Si, this deviation becomes considerable for the sample 4C because of a surface density reduction. Fig. 4.12d shows the measured (open circle) and calculated (solid lines) dynamical Bragg-peak shifts ($\Delta\theta_B$) versus X-ray wavelength/incidence angle for the samples 1C (red), 4C (blue) and non-irradiated Si (black). The fitting of the peak reveals a polarizability of χ_0^{4C} = 12.47 × 10^{-6} for the samples 4C. This value is in good agreement with obtained results for the samples using EAD at non-coplanar scattering geometry for Si (331) reflection (see subsection 4.3.2).

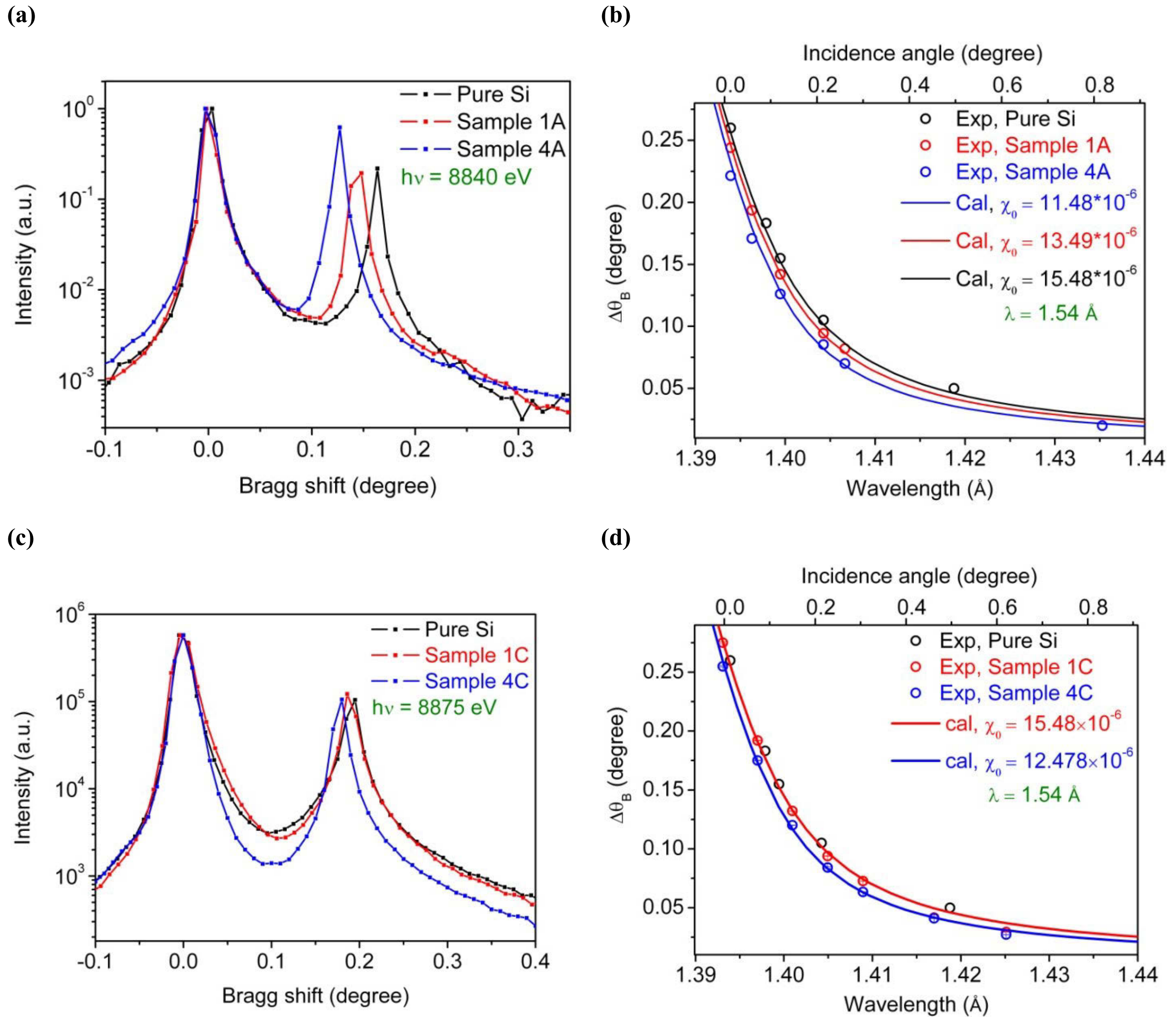

Figure 4.13: (a) The comparison of rocking curves (RCs) of Si (311) reflection for the samples 1A (red), 4A (blue), and non-irradiated Si (black) at $h\nu$ = 8840 eV (α_i = 0.08°). (b) The measured (open circles) and calculated (solid lines) dynamical Bragg peak shifts ($\Delta\theta_B$) versus wavelength/incidence angle for the samples 1A (red), 4A (blue) and non-irradiated Si (black). (c) The comparison of rocking curves (RCs) for the samples 1C (red), 4C (blue), and non-irradiated Si (black) at $h\nu$ = 8875 eV (α_i = 0.02°). (d) The measured (open circles) and calculated (solid lines) Bragg peak shifts ($\Delta\theta_B$) versus wavelength/incidence angle for the samples 1C (red), 4C (blue) and non-irradiated Si (black). The best fit for incidence angles below the α_c (vertical dashed line) results in χ_0^{Si} = 15.48 × 10^{-6}, χ_0^{1A} = 13.49 × 10^{-6}, χ_0^{4A} = 11.48 × 10^{-6} , χ_0^{1C} = 15.48 × 10^{-6} , and χ_0^{4C} = 12.48 × 10^{-6} for the non-irradiated Si, samples 1A and 4A, 1C, and 4C at λ = 1.54 Å, respectively.

Summary and discussion

In this chapter we reported on the pattern formation on Si surfaces under direct Fe ion bombardment at 5 and 20 keV ion energies and at a 65° incidence angle with respect to the surface normal with ion fluences ranging from 1×10^{16} to 5×10^{17} ions cm^{-2}. The morphologies of the surfaces were investigated by AFM and TEM measurements showing that the ripple formation occurs if the ion fluences exceeds 1×10^{16} ions cm^{-2} and the specific properties of the formed ripples (wavelength and amplitude) on the surfaces vary by variation of ion beam parameters (ion fluence and ion energy). In order to understand the mechanism of the pattern formation, nondestructive X-ray methods were applied to identify the active material parameters affecting the pattering mechanism. The surface density variation as a function of ion beam parameters was investigated.

To this aim the conventional X-ray reflectivity (XRR) method was used. It showed the formation of a few nm sub-surface layers with incorporated Fe ions in the case of smooth surfaces. For the patterned surfaces the strong decay in the reflected intensity makes a detailed evaluation impossible and with no pronounced variation at the critical angle and hence surface density is observed, due to the competing effects from surface roughness and metal incorporation.

In order to improve the surface sensitivity, the extremely asymmetric X-ray diffraction (EAD) method was applied. The access to very small incidence angles of X-ray (α_i) even below the critical angle makes the EAD method extremely surface sensitive. Depth profiling was achieved by measuring X-ray rocking curves as a function of the decreasing incidence angles down to zero degrees in non-coplanar scattering geometry using $Cu\ K\alpha$ radiation, and in coplanar geometry scattering by varying wavelengths using synchrotron radiation. The density information was extracted from the variation of the dynamical Bragg peak shift with α_i, and different critical angles were extracted from the variation of the peak widths with α_i. In contrary to the XRR, the EAD revealed a net reduction of the surface density as a function of ion fluence and ion energy.

The density reduction at the patterned surfaces increases with ion fluence, which can be explained by the high surface roughness, induced by the pattern formation. This leads to a reduction of the laterally averaged density in the topmost layer, although a considerable amount of Fe is incorporated. The observed net reduction of the surface densities at the smooth surfaces

leads to the conclusion that the process of pattern formation could be already started at Fe fluence of $\sim 10^{16}$ ion cm^{-2}. This conclusion was tested for a lower ion fluence (5×10^{14} ion cm^{-2}) confirming that there is a threshold for ion fluences leading to surface density modulation. Thus, it can be concluded that systematical variation of surface density with irradiation parameters can be considered as the important parameter related to the patterning mechanism.

5 Near surface silicide formation after off-normal Fe ion irradiation of Si(100) surfaces

In this chapter, we report on Fe-silicide formation in various stoichiometries below the amorphized surface of crystalline Si(100) after irradiation with 5 keV Fe ions under off-normal incidence. We examined the samples prepared with ion fluences of 0.1×10^{17} (sample 1A) and 5×10^{17} ions cm^{-2} (sample 4A) with both respectively exhibiting flat and patterned surface morphologies. Whereas the iron is found across the whole surface of the flat sample, its distribution on the patterned surface shows a lateral periodicity; iron is found only on top of the rippled surface.

In section 5.1, the depth resolved analysis of the chemical states of Si and Fe atoms in the near surface region performed by X-ray photoelectron spectroscopy (XPS) using energy-tunable synchrotron radiation is reported. The chemical shift and the line shape of the Si 2p, Fe 3p core levels and valence bands were measured and associated with the formation of silicide bonds of different stoichiometric composition changing from an Fe-rich silicide (Fe_3Si) close to the surface into a Si-rich silicide ($FeSi_2$) towards the inner interface to the Si(100) substrate. To support this finding in section 5.2, the XAS analysis at the Fe K-edge showing a change in chemical environment and near order atomic coordination of the Fe atoms in the region close to surface is represented.

5.1 X-ray photoelectron spectroscopy analysis

Survey XPS spectra

Depth profiling of the chemical states of the Si and Fe atoms has been performed by XPS using excitation energies of 180 eV, 350 eV, 650 eV and 1040 eV providing an electron escape depth increasing from about 1 nm to 4 nm in a flat Si sample [93]. XPS survey scans of sample 1A (blue) and sample 4A (red) were taken in the CAE mode with 23.42 eV pass energy for excitation energies of 180 eV, 350 eV and with 58.55 eV pass energy for an excitation energy of 650 eV. These survey scans are shown in Fig. 5.1a in the binding energy (BE) range between $0 < BE < 140$ eV. The measured BEs of about 100 eV, 55 eV and 25 eV are assigned to Si 2p, Fe 3p and O 2s core levels, respectively. It was shown that the XPS spectra of SiO_2 always show a sharply

pronounced O 2s peak [94, 95], which also appears in our survey spectra for all excitation energies demonstrating the formation of a thin SiO_2 layer on the surface.

Valence band (VB) spectra

The three peaks between 0-20 eV located at BE of about 1.5 eV, 7 and 11.5 eV named A, B, and C, respectively, correspond to the VB distribution (see Fig. 5.1a). Fig. 5.1b shows the high resolution VB spectra of samples 1A (blue) and 4A (red) for an excitation energy of 180 eV. The formation of oxidation states causes the increase in the intensity of peaks B and C [94, 95]. Peak B can be attributed to the 2p band of oxygen chemically adsorbed at the Si surface to form SiO_2 [94, 96-98], and is more pronounced for sample 4A, indicating a higher degree of oxidation due to the larger surface area. Furthermore, peak A which is absent in pure Si (not shown) can be attributed to a modified Fe 3d density of states caused by silicide formation [99]. This broad peak covering a BE interval between 0.6 and 2 eV can be used as a fingerprint of Fe-rich silicide bonds formed close to the surface area [100-104]. Consequently, the amount of Fe-rich silicide bonds at the top part of the surface is larger for sample 2 compared to sample 1, indicating a higher amount of iron silicide in the surface of sample 4A. It was shown that Fe_3Si starts to form only after a critical dose of the deposited Fe exceeds a thickness of ≈ 0.43 nm [100, 102]. Thus, the thickness of Fe rich layers in samples 1A and 4A (see Figs. 4.6-7) are already higher than this threshold value. Furthermore, although the two presented valence band spectra in Fig. 5.1b are overall quite similar, the higher intensity of peak A for sample 4A suggests a larger amount of Fe-silicide formation for this sample, which agrees qualitatively with the results of the RBS measurements.

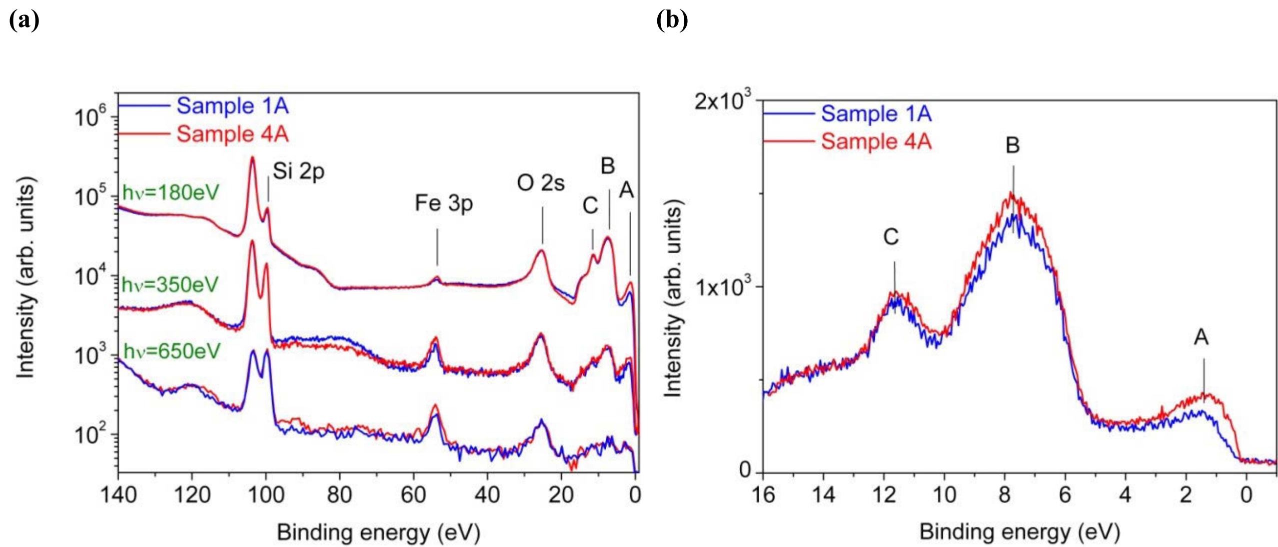

Figure. 5.1:(a) Wide-scan X-ray photoemission spectra of Si(100) irradiated with 5 keV Fe ions incident at 65° with respect to the surface normal at different fluences of 1×10^{16} ions cm^{-2}, sample 1A (blue), and 5×10^{17} ions cm^{-2}, sample 4A (red), for excitation energies of 180 eV, 350 eV and 650 eV from top to bottom, respectively. The pass energy for survey scan is 23.42 eV with spectrometer resolution ca. 0.5 eV. (b) XPS valence band spectra of the sample 1A (blue) and sample 4A (red) at hν = 180 eV. The pass energy is 2.33 eV with spectrometer resolution less than 0.1 eV. See text for explanation of peaks A, B and C.

Si 2p XPS spectra

It is known that the Si 2p core levels in Fe-silicides are shifted towards higher binding energies with respect to pure silicon for increasing Fe concentration [105]. This functional behavior was applied to evaluate high resolution XPS measurements taken in the vicinity of the Si 2p core level for samples 1A and 4A using different excitation energies.

Figs. 5.2a-d show the Si 2p core level spectra of sample 1A (full points) and sample 4A (open circles) for excitation energies of 180 eV, 350 eV, 650 eV and 1040 eV, respectively. Each spectrum was fitted by a Shirley type background and Gaussian peak functions of different energy and FWHM. In particular the FWHM of the Si $2p_{3/2}$ and Si $2p_{1/2}$ core levels are estimated to be about 0.6 eV, 0.7 eV, 1.2 eV and 1.6 eV for excitation energies of 180 eV, 350 eV, 650 eV and 1040 eV, respectively.

The measured profiles can be fitted by four peaks (red and blue curves in Fig. 5.2). The two peaks at about 103.8 eV and 102.5 eV are assigned to SiO_2 and a silicon suboxide SiO_{2-x}, respectively [106]. Those compounds will always form due to the air exposure of the samples after removal from the irradiation chamber. The other two peaks close to 100 eV can be ascribed to the spin-orbit splitted levels of Si $2p_{3/2}$ and Si $2p_{1/2}$. In the case of silicide bond formation these two peaks experience a peak shift with respect to pure Si expected at 99.4 eV and 100.1 eV, respectively. For both samples, the intensity of the peaks assigned to SiO_2 increases with decreasing excitation energy, while that attributed to Si 2p decreases, indicating the formation of SiO_2 on top of the surfaces. While the position of the SiO_2 peak is independent from the excitation energy, the peak intensity is higher for sample 4A compared to sample 1A indicating a higher degreee of oxidation due to the rippled surface of sample 4A. This is in agreement with the valence band peak B of both samples (see Fig. 5.1b).

The measured Si $2p_{3/2}$ and Si $2p_{1/2}$ core levels peaks are originating from photoelectrons of pure silicon and various silicides. In order to quantify the contribution of silicides, both peaks were fitted by Gaussians. Compared to pure silicon the peak maxima of the fitted Gaussians always show a shift towards higher BE with a larger amount for sample 1A (fitted red curves) compared to sample 4A (fitted blue curves) at excitation energies of 180 eV, 350 eV and 650 eV. The inset of Fig. 5.2a shows the magnification of Si $2p_{3/2}$ and Si $2p_{1/2}$ core levels for sample 1A (red curves) and sample 4A (blue curves) for an excitation energy of 180 eV. It highlights a smaller peak shift of sample 4A compared to sample 1A which is accompanied by a larger intensity of the Si $2p_{3/2}$ and Si $2p_{1/2}$ core level peaks due to the higher amount of Fe-silicide as revealed from valence band spectra (see Fig. 5.1b). Qualitatively similar shifts are observed for excitation energies of 350 eV and 650 eV but with decreasing magnitude. The peaks of both samples nearly coincide for an excitation energy of 1040 eV. Comparing the four excitation energies, the determined BEs of Si $2P_{3/2}$ core levels are 99.65 eV, 99.83 eV, 99.89 eV and 99.63 eV for sample 1A and 99.49 eV, 99.63 eV, 99.71 eV and 99.60 eV for sample 4A using excitation energies of 180 eV, 350 eV, 650 eV and 1040 eV, respectively, measured from the peak maxima of the fitted Gaussians.

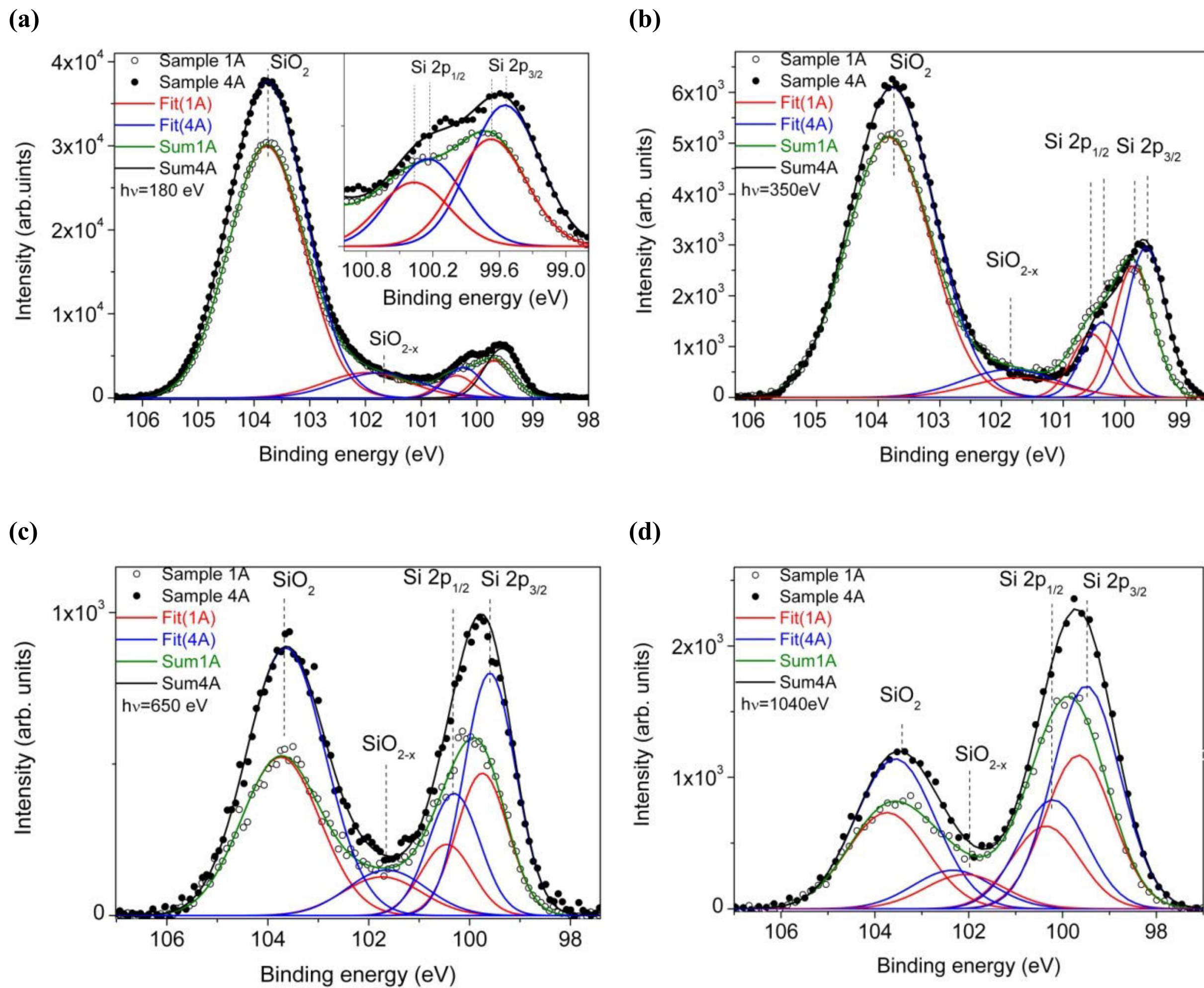

Figure. 5.2. Comparison of Si 2p core level spectra of Si(100) irradiated with 5 keV Fe ions incident at 65° with respect to the surface normal at different fluences of 1×10^{16} ions cm^{-2}, sample 1A, with measured data (open circles) fitted by a Shirley type background (continuous red curves), and 5×10^{17} ions cm^{-2}, sample 4A, with measured data (full circles) fitted by a Shirley type background (continuous blue curves): at hν = 180 eV (a), hν = 350 eV (b), hν = 650 eV (c), and hν = 1040 eV (d). The inset in (a) shows the magnification of the Si 2p core level spectra in the vicinity of silicide bond for both samples.

Fig. 5.3 shows the variation of the BE of Si $2p_{3/2}$ core levels of sample 1A (red) and sample 4A (blue) as a function of excitation energies and the respective electron escape depth. For comparison the BE of various silicides and pure silicon are shown as well (horizontal dashed lines). The top axis indicates the photo electron escape depth as estimated for pure silicon in case

of a flat surface. The measured peak shift is maximum for excitation energies between 350 eV and 650 eV.

Considering the increase of the electron escape depth for increasing excitation energies (see subsection 3.4.2), the measured shifts for sample 1A follows qualitatively the decreasing Fe content from top towards the bulk. This becomes understandable assuming nearly uniform distribution of Fe along the flat surface. The situation is much different for sample 4A where the silicides are accumulated at the top of the ripples. Although the integral Fe content is higher compared to sample 1A (higher peak intensities), the measured peak shift is always smaller (by about 0.15eV). The striking argument for the reduction of BE in sample 4A is an inhomogeneous distribution of Fe across the surface seen in Fig. 4.7a. So, the measured photoelectrons are originating simultaneously from the Fe-rich silicon ridges and almost pure silicon in the side-walls and valleys. As the BE of Si 2p core levels in pure Si is lower than those of most of the Fe-silicides [105], the contribution of Si atoms from side-walls and valleys leads to a systematic reduction in BE of sample 4A with respect to sample 1A for excitation energies up to 650 eV. Therefore qualitatively the blue curve in Fig 5 can be interpreted in similarly to sample 1A, i.e. in the silicide regions the Fe content decreases from surface towards the bulk. For the highest excitation energy (1040 eV) the contribution of underlying bulk Si dominates for both samples independently from the surface pattern but is still influenced by the iron which is in good agreement with results of Sánchez-García *et al*. reporting a similar chemical state for Si $2p_{3/2}$ using a $Mg\ K\alpha$ X-ray source (1253.6 eV) [107].

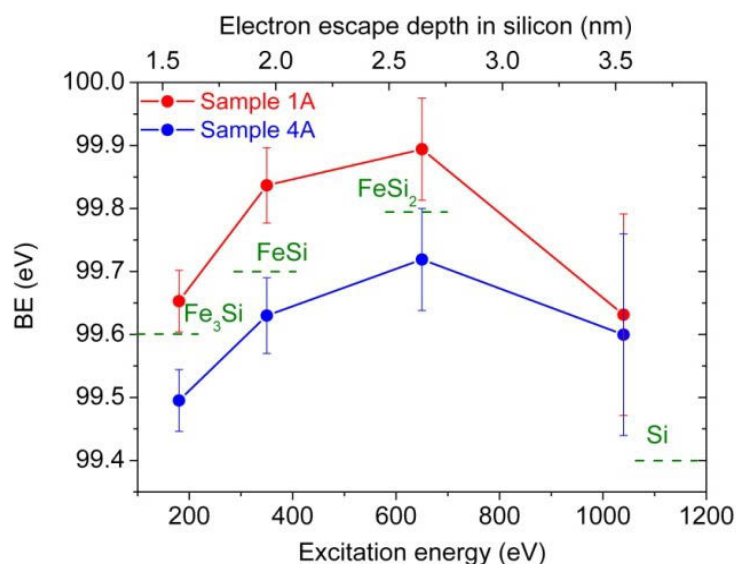

Figure. 5.3. Binding energies of Si $2p_{3/2}$ core level as a function of excitation energies and electron escape depth (upper x-axis assuming a pure Si surface) in Si(100) irradiated with 5 keV Fe ions incident at 65° with respect to the surface normal at different fluences of 1×10^{16} ions cm^{-2}, sample 1A (red), and 5×10^{17} ions cm^{-2}, sample 4A (blue). Olive dashed horizontal lines indicate the reported BE of Si $2p_{3/2}$ core levels for Fe_3Si (99.6 eV), FeSi (99.7 eV), $FeSi_2$ (99.8 eV) and Si (99.4 eV) [105].

Fe 3p XPS spectra

The kind of chemical bonding between Si and Fe atoms can also be deduced from both the line shape and the shift of the Fe 3p core levels [105, 108]. It was shown that the modulation in the VB due to the formation of different stoichiometric composition of Fe-silicides has a direct influence on the shape and energetic position of the Fe 3p peaks [109, 110].

The BE of the Fe 3p core levels were measured at different excitation energies. Because of the formed SiO_2 layer on top of the surface the intensity of the Fe 3p photoelectron peak at 180 eV is very low (see Fig. 5.1a). Thus high resolution Fe 3p core levels spectra of samples 1A and 4A are measured at excitation energies of 350 eV and 650 eV and are compared in Figs. 5.4a-d. All spectra look asymmetric with a wider slope towards higher BEs. This is attributed to the contribution of silicides with different Fe content that are enhanced close to the surface. Following this assumption, the Fe 3p core level spectra were decomposed into two contributions of Fe-Si bonds. The fitted peaks located at BE = 53.75 eV (red curves) can be attributed to

silicides with high Fe contents such as Fe_3Si [109, 111]. The Gaussian width (≈ 1.7 eV) of this peak was kept fixed and the remaining part of the experimental curves were fitted by a second Gaussian (green curves), approximating the BE of the other stoichiometry, such as FeSi and $FeSi_2$.

It turns out that the photoelectron intensity taken from sample 4A is higher compared to sample 1A which refers to the higher content of implanted Fe. In addition, the relative contribution of Fe_3Si to the photoelectron peak is larger in sample 4A. This means that in the ridges of the rippled surface a higher part of Fe atoms is bond in this Fe rich stoichiometry which could be easily explained by the lateral periodicity of the iron concentration. On the other hand, the asymmetry of the photoelectron peak towards higher BE is always larger for 650 eV excitation energy compared to 350 eV which reflects the silicide distribution with decreasing Fe amount towards the depth.

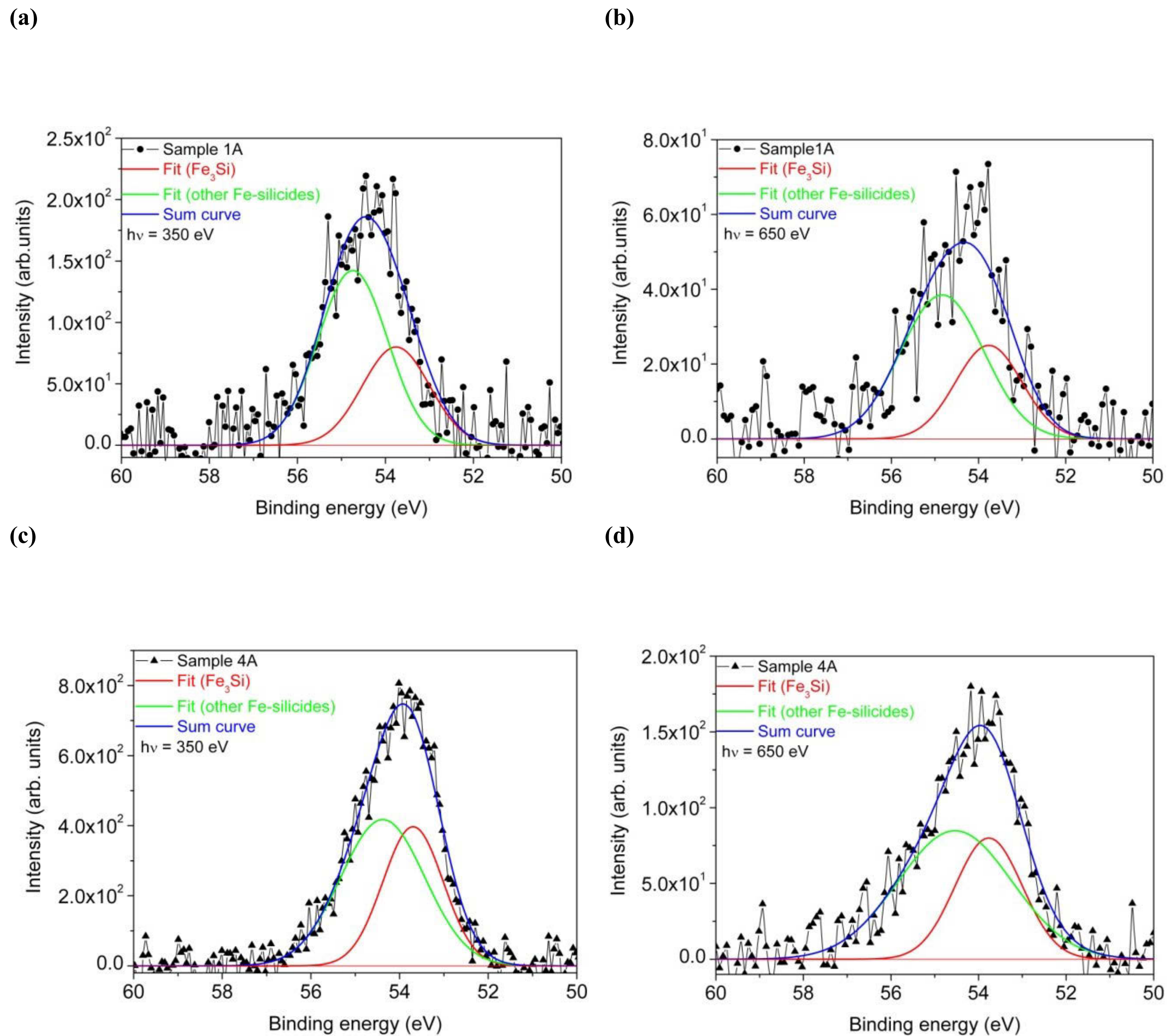

Figure. 5.4. The measured Fe 3p core level spectra of Si(100) irradiated with 5 keV Fe ions incident at 65° with respect to the surface normal at different fluences of 1×10^{16} ions cm^{-2} (sample 1A) and 5×10^{17} ions cm^{-2} (sample 4A) at different excitation energies: (a) sample 1A (dot-line) at hν = 350 eV , (b) sample 1A (dot-line) at hν = 650 eV, (c) sample 4A (triangle-line) at hν = 350 eV , and (d) samples 4A (triangle-line) at hν = 650 eV. After substraction of a Shirley type background, the measured data were fitted by two Gaussians (blue sum curves). The obtained red curves correspond to the Fe_3Si and the green curves correspond to the other Fe-silicides.

5.2 X-ray absorption spectroscopy (XAS) analysis

For a depth resolved characterization of the chemical state and the atomic near order of the Fe atoms XAS measurements have been performed in the vicinity of the Fe K-edge at 7112 eV. The penetration depth was tailored by varying the incidence angle of X-ray beam (α_{in}) from 0.01° < α_c = 0.22° to 0.5° > α_c (critical angle of total external reflection of Si) with respect to the sample surface. Magnified views of the X-ray absorption near edge structure (XANES) of the samples 1A and 4A are presented in Figs. 5.5a-b. For comparison, XANES reference spectra of Fe_3Si, FeSi, $FeSi_2$, are shown in Fig. 5.5c. As characteristic feature, they display a shift of the absorption maximum towards lower photon energy for increasing Fe concentration in the silicide, i.e. from Fe_3Si over FeSi to $FeSi_2$. Qualitatively, similar shifts are observed for sample 1A and 4A where the feature of Fe_3Si is more pronounced at sample 4A compared to sample 1A. The measured spectrum taken at α_{in} = 0.01° (black curves in Figs. 5.5a-b) shows its maximum at a lower photon energy compared to the spectrum taken at α_{in} = 0.5° (blue curve). Because a lower α_{in} corresponds to a lower average X-ray penetration depth, this observation is an additional proof for the appearance of Fe-rich silicides in the near surface region, and the dominance of a Si-rich silicide for larger depth. More details of the data evaluation of XANES are presented elsewhere [112].

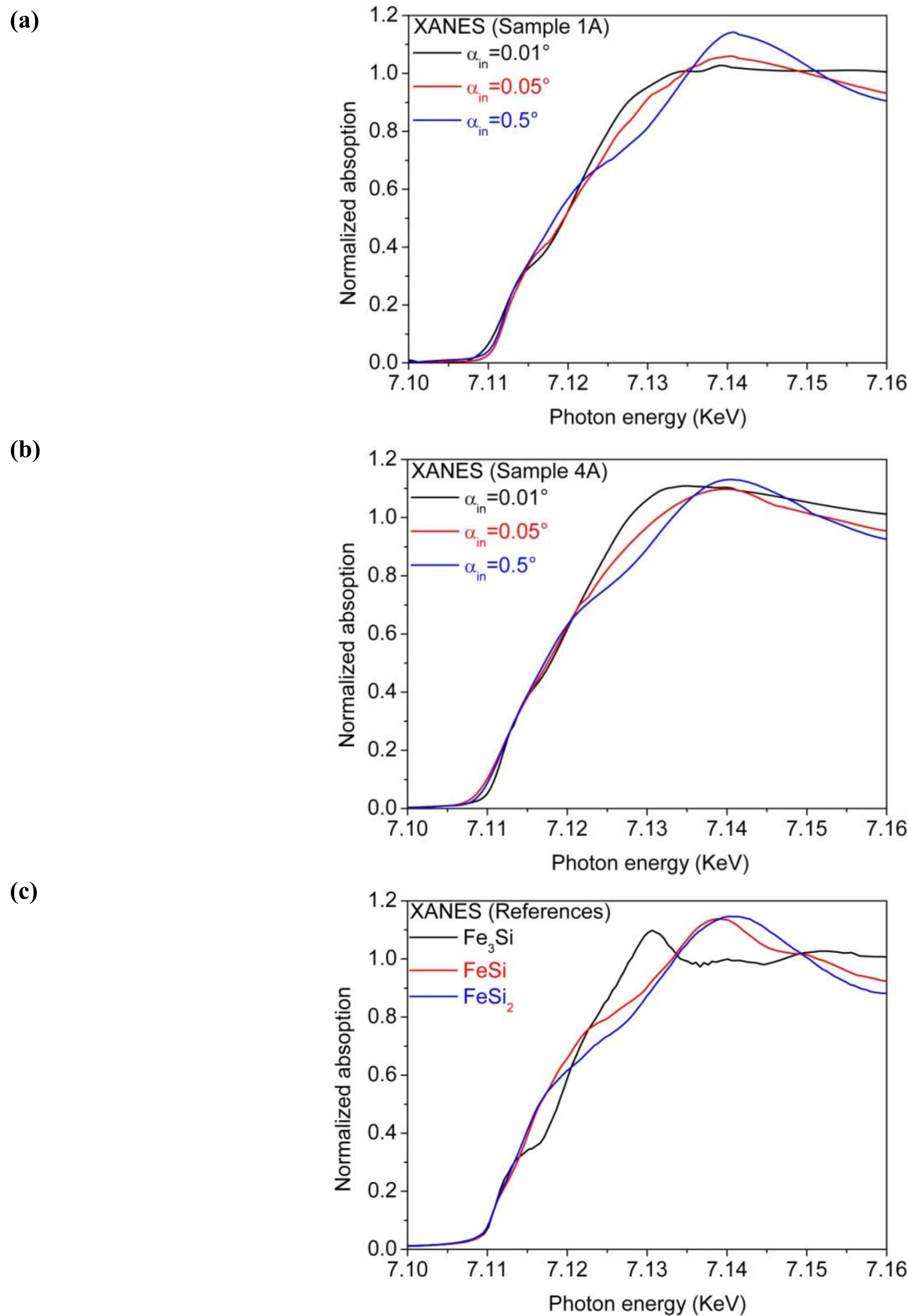

Figure. 5.5: Comparison of normalized Fe K-edge XANES spectra at different X-ray incidence angles of 0.01° (black) , 0.05° (red) and 0.5° (blue) in Si(100) irradiated with 5 keV Fe ions incident at 65° with respect to the surface normal at different fluences of (a) 1×10^{16} ions cm^{-2} (sample 1A), and (b) 5×10^{17} ions cm^{-2} (sample 4A). (c) Comparison of the normalized XANES spectra at Fe K-edge of reference powder samples; Fe_3Si (black), FeSi (red) and $FeSi_2$ (blue).

Fig. 5.6a shows a comparison of normalized extended X-ray absorption fine structure (EXAFS) spectra of sample 1A at α_{in} = 0.01° (black curve) and α_{in} = 0.5° (blue curve) with spectra of sample 4A, (olive and gray curves), respectively. Reference spectra of Fe_3Si, FeSi and $FeSi_2$ are shown in Fig. 5.6b. The peak maxima of both spectra located at 7.140 keV, 7.190 keV and 7.255 keV coincide well with those of the $FeSi_2$ reference spectrum (blue curve in Fig. 5.6b). In other words, the $FeSi_2$ formation is dominant for larger depths for both samples independently of their surface morphologies. By reducing the incidence angle to 0.01° the EXAFS spectrum of sample 1A fits closer to the Fe_3Si reference spectrum (black curve in Fig. 5.6b) accompanied by a pronounced shift towards lower photon energy in the edge region for sample 4A. This can be attributed to an enhanced tendency to form Fe_3Si silicide close to the surface at sample 4A.

For simulating the EXAFS spectra we assumed that the investigated samples consist of a mixture of three reference compounds. Therefore we fitted the measured spectra by a linear combination of Fe_3Si, FeSi and $FeSi_2$ reference spectra. The phase fractions were varied until best agreement between the experimental and calculated spectra was achieved. Fig. 5.7(a-c) shows selected fit results for sample 1A (red) and 4A (blue) for incidence angles of α_{in} = 0.05°, α_{in} = 0.2° and α_{in} = 0.5°, respectively. For the fits, the energy scale of the EXAFS spectra were transformed to a wave number (k) scale of the emitted photoelectrons by $k = \sqrt{2m(E-E_0)} / \hbar$ where E E is the actual photon energy, E_0 the edge energy, m the electron mass, and $\hbar=h$ $\hbar = \frac{h}{2\pi}$ $/2\pi$ Planck's constant. The X-ray absorption fine structure $\chi(k)$ was extracted from the experimental data by subtracting a smooth background function above the edge, and the data were weighted by k^2 in order to compensate the k-dependent fast decay of $\chi(k)$.

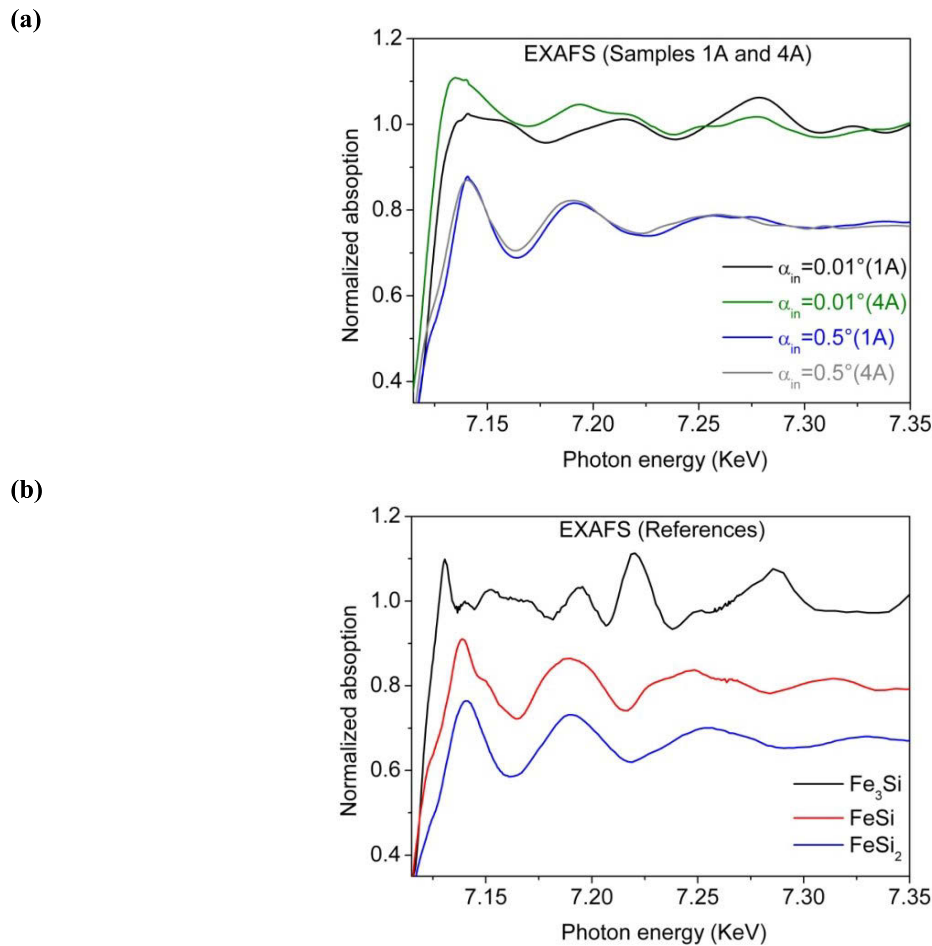

Figure. 5.6: (a) Comparison of normalized Fe K-edge EXAFS spectra of sample 1A and 4A at different X-ray incidence angle. At α_{in} = 0.01°: sample 1A (black) and sample 4A (olive), and at α_{in} = 0.5°: sample 1A (blue) and sample 4A (gray). (b) Comparison of the normalized EXAFS spectra at the Fe K-edge of reference powder samples: Fe_3Si (black), FeSi (red), and $FeSi_2$ (blue). The spectra were shifted vertically for better visibility.

Qualitatively acceptable fits are obtained for all incidence angles, and Fig. 5.7d-e shows a compilation of the fit results for samples 1A and 4A, respectively.

Qualitatively the depth dependence of the phase formation is similar for both samples. This is not surprising because this method is not sensitive to the lateral variations of Fe distribution due to the Fe-free regions such as valleys in rippled sample which do not contribute to the signal. For both samples the contribution of the Fe_3Si silicide rapidly decreases by increasing the incidence angle, and the contribution of the $FeSi_2$ silicide increases accordingly.

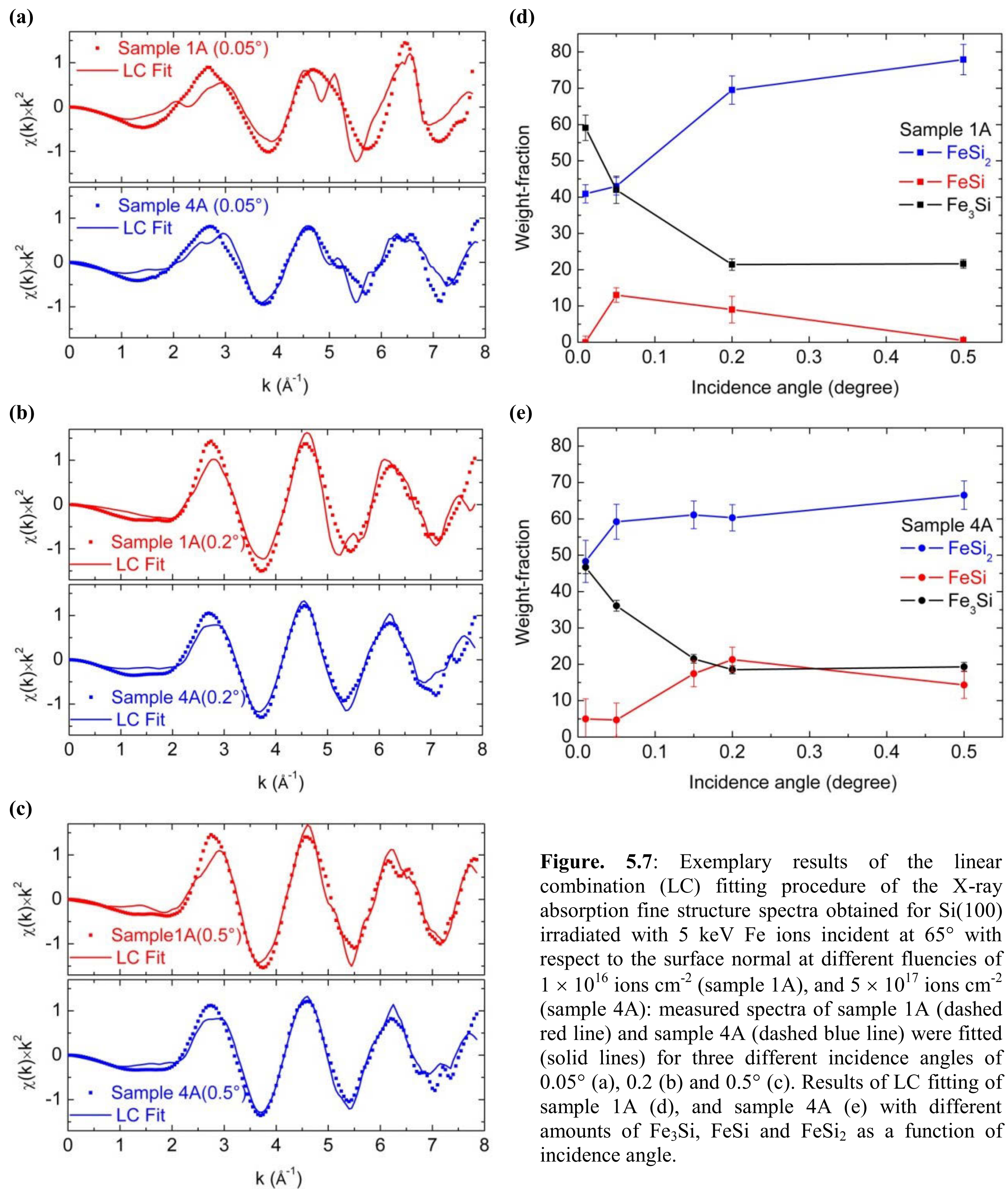

Figure. 5.7: Exemplary results of the linear combination (LC) fitting procedure of the X-ray absorption fine structure spectra obtained for Si(100) irradiated with 5 keV Fe ions incident at 65° with respect to the surface normal at different fluencies of 1×10^{16} ions cm^{-2} (sample 1A), and 5×10^{17} ions cm^{-2} (sample 4A): measured spectra of sample 1A (dashed red line) and sample 4A (dashed blue line) were fitted (solid lines) for three different incidence angles of 0.05° (a), 0.2 (b) and 0.5° (c). Results of LC fitting of sample 1A (d), and sample 4A (e) with different amounts of Fe_3Si, FeSi and $FeSi_2$ as a function of incidence angle.

In addition, it becomes possible to identify the amount and nature of Fe-Si bonds to the spectra. This bond is present in larger amount in sample 4A which is in agreement with the Fe 3p XPS spectra (see Fig. 5.4) showing a larger FWHM of Gaussians for the sample 4A in comparison to sample 1A. Here it should be mentioned that neither in the Fe K-edge XANES and EXAFS spectra (Figs. 5.5 and 5.6) nor in the Fe 2p (not shown) and Fe 3p photoemission spectra (Fig. 5.4) any effect of metal oxidation is observed. Therefore the formation of iron oxide is neglected in our model. Furthermore, the fit quality generally decreases for smaller incidence angle. This is mainly related to the fact that the footprint of the X-ray beam exceeds the actual sample size of 10 mm for incidence angles smaller than about $\alpha_i = 0.28°$, reaching values of e.g. 28 mm for $\alpha_i = 0.1°$, and even 57 mm for $\alpha_i = 0.05°$. Thus the intensity of all measured signals decrease with incidence angle, and the R factors of the fit ($R = \Sigma\, \chi_{exp.}(k)*k^2) / \Sigma\, \chi_{fit.}(k)*k^2)$ increase from about 0.08 – 0.09 for $\alpha_i = 0.2°$ and $\alpha_i = 0.5°$ to about 0.3 - 0.45 for $\alpha_i = 0.05°$. Keeping in mind that the photon statistics are substantially worse for the small incidence angles, however, this fit quality appears reasonable.

Summary and discussion

Using XPS and XAS analyses, the chemical state and atomic coordination of Fe-silicides were investigated in the nearly amorphized surface layer of crystalline Si(100), after irradiation with 5 keV Fe ions at oblique incidence angle. Two samples were prepared and studied with ion fluences of 0.1×10^{17}, just below the threshold for pattern formation (sample 1A), and 5×10^{17} ions cm^{-2}, just above this threshold (sample 4A). The Fe distribution in sample 1A is laterally uniform, whereas it becomes laterally inhomogeneous in sample 4A in which the iron is concentrated in the top region of the ripples at the sides facing the incident ion beam, as seen by TEM. Although no crystalline silicide could be detected by X-ray diffraction [113], XPS and XAS revealed that Fe is chemically bonded in a Si framework within a thin surface layer. Using both methods, it was shown that the Fe concentration of these silicides changes with depth. The atomic coordination is similar to a Fe-rich silicide at the outer surface, while a Si-rich silicide with a structure similar to that of $FeSi_2$ is found at inner interfaces towards the Si crystal.

The chemical depth profiles were deduced from the shift of the Si $2p_{3/2}$ core levels. Considering a functional relationship between the core level shift and the chemical state of Si in different silicide stoichiometry as taken from Ref. [105] (see olive dashed lines in Fig. 5.3), the Fe starts to form silicides where the Si is coordinated by at least three Fe atoms close below the surface (Fe_3Si) and reaches $FeSi_2$ stoichiometry at a larger depth. This depth dependence of the Fe concentration is verified by XAS (Fig.5.7). At the surface, a dominant atomic coordination was found similar to a Fe-rich silicide (Fe_3Si), and the concentration of the lower stoichiometric phases of Fe silicides (mainly $FeSi_2$) is increasing towards the bulk penetration depths. For the flat sample 1A, the Si-rich silicide ($FeSi_2$) appears at a depth of about 3 nm, which is consistent with TEM analysis (Figs 4.6-7) and reflectivity measurements [114] where a layer of high Fe concentration of about 2.5 nm is visible.

The influence of the morphology on the obtained depth dependency can be directly deduced from the results of the XAS measurements for sample 1A and 4A (Fig. 5.5) in comparison with the TEM data (Fig. 4.6-7). A high concentration of Fe is present in one half of the ripple period only. This Fe is accumulated on the side facets facing the ion beam with a thickness that is more than a factor of 2 larger compared to the flat sample (~7 nm). Therefore the XAS spectra of both samples (Fig. 5.7a-b) should show a different depths dependence due to the "laterally averaged" information. However, taking these results into account it can be concluded that the pattern formation is strongly influenced by the formation of Fe-silicides near the surface. Since the different stoichiometry of Fe-silicides have different cohesive energies [115], they have different surface binding energies and thus different sputter yields. In this context, the different sputtering yields of silicon and iron and the inhomogeneous lateral distribution of iron has to be taken into account. Therefore different areas along the surface will exhibit different sputter yields that influence the process of ion beam erosion and may even lead to an enhancement of the processes that are responsible for the ripple formation. This conclusion is in agreement with the predictions of Bradley's theory, in which a chemical reaction between impurity atoms and target atoms are supposed to destabilize the surface as a precondition for ion induced pattern formation.

6 Recrystallization of Fe ion irradiated Si(100)

In the previous chapter, it was demonstrated that the irradiation of the Si(100) surfaces with Fe ions at room temperature causes the formation of buried amorphous silicides with different stoichiometries changing from a Fe-rich silicide (Fe_3Si) at the topmost layer to a Si-rich silicide ($FeSi_2$) towards the bulk Si. Considering the fact that the near surface region is amorphous, crystalline silicides were not observed using X-ray diffraction methods [113]. Therefore, a thermal annealing process was applied to observe the recrystallization process of various silicides.

In this chapter, the structural transition from amorphous to crystalline phase during annealing process is described. To obtain information regarding the formed silicide phases and their spatial distribution in the Fe-Si layer, grazing incidence X-ray diffraction (GI-XRD) measurements were applied. We examined samples, prepared under off-normal irradiation with 20 KeV Fe ions at different fluences of 0.1×10^{17} ions cm^{-2} (sample 1B) and 5×10^{17} ions cm^{-2} (sample 4B) exhibiting a smooth and patterned surface morphology, respectively.

After a short review of the equilibrium phase diagram and preliminary crystallographic properties of the Fe-Si binary system, the experimental procedure of the annealing process is presented. In section 6.1, the effect of ion fluence on the formation of different silicide phases during crystallization of an amorphous Fe-Si layer is investigated. In section 6.2, ion beam-induced strain profiles before and after annealing are presented.

Preliminary crystallographic data

Fig. 6.1a shows the equilibrium phase diagram of the Fe-Si binary system [116]. Various iron silicides with different physical properties are formed as a function of composition and temperature. Some of iron silicide phases (Fe_3Si, FeSi, and $FeSi_2$) are reviewed.

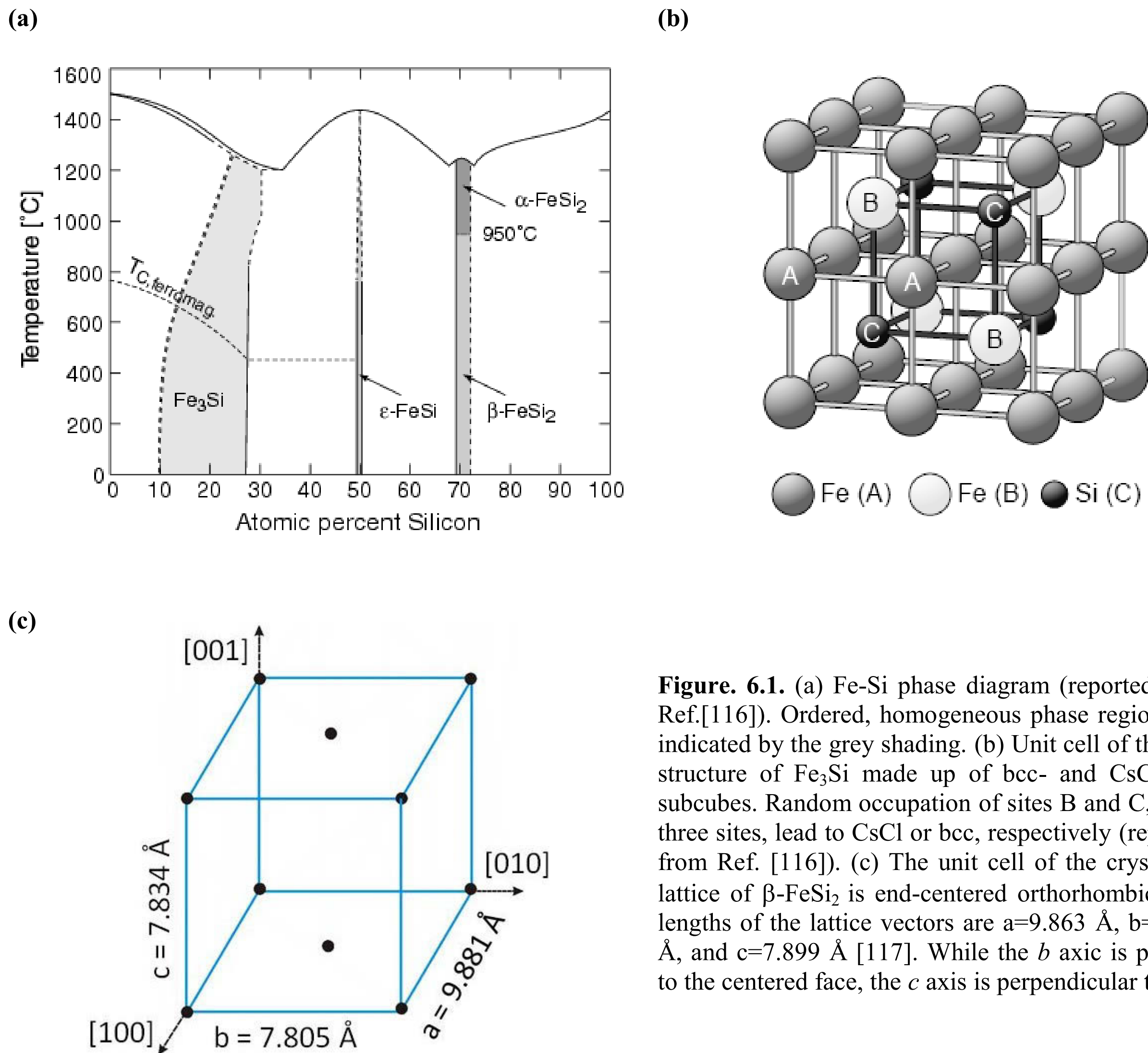

Figure. 6.1. (a) Fe-Si phase diagram (reported from Ref.[116]). Ordered, homogeneous phase regions are indicated by the grey shading. (b) Unit cell of the $D0_3$ structure of Fe_3Si made up of bcc- and CsCl-type subcubes. Random occupation of sites B and C, or all three sites, lead to CsCl or bcc, respectively (reported from Ref. [116]). (c) The unit cell of the crystalline lattice of β-$FeSi_2$ is end-centered orthorhombic. The lengths of the lattice vectors are a=9.863 Å, b=7.791 Å, and c=7.899 Å [117]. While the *b* axic is parallel to the centered face, the *c* axis is perpendicular to it.

The low temperature phases are Fe_3Si and FeSi, the later is starting to grow at 450-500°C [118] and is a semiconductor with narrow band gap of 0.05 eV [119]. At room temperature, Fe_3Si phase is crystallized in the $D0_3$ crystal structure (see Fig. 6.1b) in a cubic unit-cell with a=5.665Å [120]. The cell parameter of FeSi is a=4.4527 Å with the cubic symmetry [121].

Fe-disilicide can form in cubic (metastable γ-$FeSi_2$ phase), orthorhombic (low temperature stable β-$FeSi_2$ phase) and tetragonal structures (α-$FeSi_2$ phase stable at temperature above 930°C). Both α and γ phases have metallic properties. The crystallographic analysis shows that the α phase is better lattice matched with Si than the β phase, while the cubic phase is best

matched with Si among the three $FeSi_2$ phases, because of $a_c \simeq a_{Si}$=5.431 Å. In the case of α-$FeSi_2$ (a_α=b_α=2.695 Å and c_α=5.14 Å), since $2a_\alpha$=5.390 Å, the lattice mismatch between α-$FeSi_2$ and Si or cubic $FeSi_2$ is only 0.7% along the *a* or *b* axis, as compared to a mismatch of ~ 2% for β-$FeSi_2$, grown epitaxially on a Si(100) substrate [122].

The metastable $FeSi_2$ phase transforms into the β-$FeSi_2$ phase upon annealing. The transition temperature was found to decrease with increasing the thickness of the epilayer [123].

The semiconductor β-$FeSi_2$ phase is a narrow band gap (0.85 eV) semiconductor, and starts to nucleate from FeSi at about 550°C, but a much higher temperature is needed for complete crystallization of a β-$FeSi_2$ layer. The β-$FeSi_2$ phase is in equilibrium with Si at low temperature [124]. Indeed the β-$FeSi_2$ phase is a rather peculiar semiconductor as its electronic structure is not based on the SP^3 hybridization, as it is the case for other common semiconductors (Si, Ge, GaAs,…), but on a solid-state Jahn-Teller effect [125]. The unit cell of the end-centered crystalline lattice of the β-$FeSi_2$ phase is shown in Fig. 6.1c [117].

Growth of thin iron silicide on silicon substrate

With very thin films, one observes usually the growth of strained and /or pseudomorphic phases, adopting the substrate structure. Furthermore, in ultra thin films different crystalline phases are observed in the entire composition range [116], which cannot be analyzed in terms of the bulk phase diagram [126]. Their structures and physiochemical properties can be quite different from those expected in the bulk phase diagram. For instance, the tetragonal α-$FeSi_2$ phase has been reported to grow at a temperature (550°C) much lower than predicted value by the bulk phase diagram (at 940°C). In addition, the formation of α-$FeSi_2$ in epitaxy with Si matrix with two type of orientations (fully aligned and twinned with a same type of epitaxial relationship) at the Fe ion implantation in Si(100) during crystallization at 320°C was observed [122, 127]. However, all of them evolved towards the equilibrium phases with increasing thickness and temperature, following equilibrium thermodynamic predictions.

Experimental procedure

Annealing of selected samples was performed in a vacuum chamber with pressure of 10^{-6} mbar. The temperature was selected in the range between RT and 800°C in steps of 100°C. All the samples were analyzed by X-ray diffraction (XRD) at grazing incidence angle (GI) geometry at beamline ROBL at ESRF equipped with a six-circle goniometer and a linear detector. The GI-XRD measurements were performed at a fixed incidence angle (α_{in}) in a step-scanning mode with a step size of 0.1° for thermal annealing and 0.05° for depth profiling, using X-ray wavelength of λ=1.078 Å. The annealing was carried out using DHS 900 Domed Hot Stage Anton Paar GmbH attached to the goniometer equipped with TCU 150 temperature control unit. The heating rate was kept ~ 5°C/min.

AFM analysis

Figs. 6.2(a-b) show the surface morphologies of the samples 1B and 4B after annealing. The morphologies of the surfaces are similar with those before annealing (see Figs. 4.2a, d), except a small variation in RMS roughness. While the surface of sample 1B remains smooth (Fig. 6.2a), it changes to column like morphology for sample 4B (Fig. 6.2b).

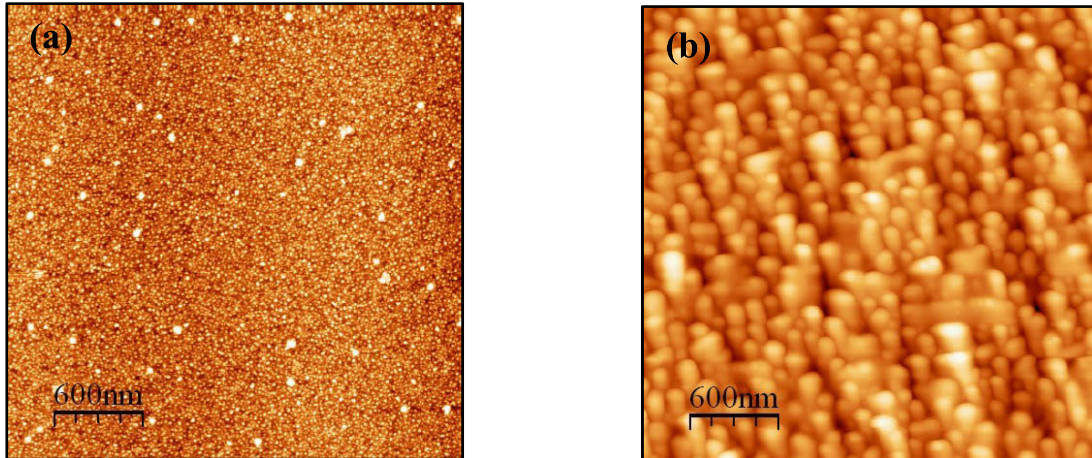

Figure. 6.2. AFM images of Si surfaces irradiated with 20 keV Fe ions at 65° incident angle with respect to the surface normal at different fluences: (a) Sample 1B (z_{max} = 4.83 nm, RMS = 0.37 nm) at 1 × 10^{16} ions cm^{-2}. (b) Sample 4B (z_{max} = 112.8 nm, RMS = 14.52 nm) at 5 × 10^{17} ions cm^{-2}. The z is the height difference corresponding to the colour scale range. The imagines size is 3 × 3 μm^2.

6.1 Effect of ion fluence on the phase composition

6.1.1 Structural evolution in high-fluence Fe ion irradiated Si upon thermal annealing

Fig. 6.3a shows the measured GI-XRD spectra of sample 4B, irradiated at fluence of 5×10^{17} ions cm^{-2}, for different annealing temperatures starting at RT (gray), 400°C (black), 500°C (orange), 600°C (red), 700°C (olive), and 800°C (blue). While upto 400°C no diffraction peaks are observed, at 500°C a small but sharp peak is appeared at 2θ = 20.16° indicating the onset of recrystallization of amorphous Fe-silicides. By increasing the annealing temperature up to 700°C two additional broad peaks are appeared at 2θ ~ 31.7° and 2θ ~ 33.7° accompanied by increasing intensity and width of the observed peak. These three peaks correspond to the diffraction peaks of (220)/(202), (040) and (422) of the orthorhombic β-$FeSi_2$ phase [117, 121, 128]. The asymmetry of the last two peaks indicates a trace of overlapping between the signals of $FeSi_2$ and formed FeSi phase as reported in Ref. [118]. As no reflection from non-reacted iron is detected, all elemental iron is consumed by the growth of silicides, in agreement with X-ray absorption analysis [112]. By increasing the annealing temperature to 800°C, a new small peak at 2θ = 19.45° shows up. This peak is assigned to (110) reflection of ε-FeSi phase [118, 121]. The formation of ε-FeSi and β-$FeSi_2$ phases in Fe ion impalanted Si has already reported in Refs. [127, 129-131]. Katsumata *et al.* [132] reported also on formation of polycrystalline ε-FeSi and β-$FeSi_2$ during annealing of Fe ion implanted Si(001) with differnet energies and fluences.

Fig. 6.3b shows the extracted FWHM of the (220) main reflection of β-$FeSi_2$ as a function of annealing temperature[1]. It can be seen that by increasing the annealing temperature, the FWHM decreases indicating of increasing in crystalline size. The particle size, *t*, was calculated using *Scherrer* equation [133]:

$$t = 0.9\lambda / B \cos \theta_B \quad (6.1)$$

[1] The FWHM of other reflections did not take into account because of difficulty in distinguish between the two phases in these spectra.

where λ is the wavelength of the used X-rays, B is usually measured, in radians, at an intensity equal to half the maximum intensity and θ_B is the angle of diffraction. The inset of Fig. 6.3b shows the variation of calculated particle size of the β-$FeSi_2$ phase along the (220) direction. It can be seen that the average crystalline size increases from ~ 16 nm to ~ 28 nm by increasing annealing temperature from 500°C to 800°C.

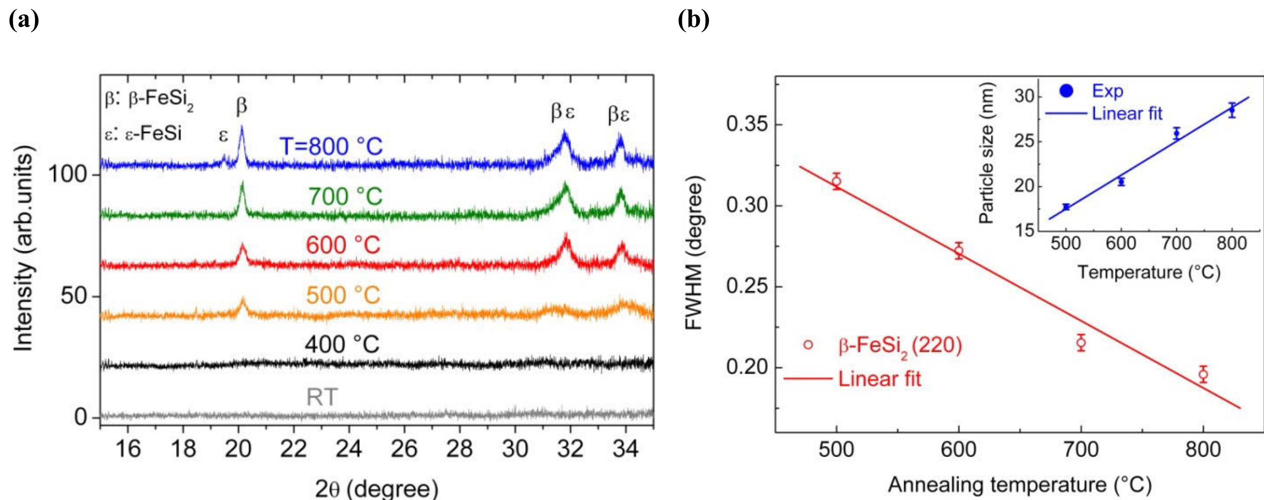

Figure. 6.3: (a) The measured GI-XRD spectra of the sample 4B (irradiated in off-normal with 20 KeV Fe ions at fluence of 5×10^{17} ions cm^{-2}) at 800°C (blue), 700°C (olive), 600°C (red), 500°C (orange), 400°C (black), and room temperature-RT (gray), taken at incidence angle of α_{in}=1° using λ=1.078 Å, and $\Delta 2\theta$=0.1°. (b) The variation of FWHM of the β-$FeSi_2$ (220) reflection with annealing temperature. The insert shows the variation of crystallite size with annealing temperature, calculated for β-$FeSi_2$ (220) reflection using Scherrer formula.

To obtain more information regarding the crystalline phases and their spatial distribution within the formed silicide layer, the GI-XRD profiles were recorded at fixed temperature (T=800°C) as a function of incidence angle varying in steps of 2θ = 0.05°. The measured spectra at α_i = 0.2°, α_i = 0.5° and α_i = 1° are shown in Fig. 6.4a from top to bottom, respectively. At all incidence angles four pronounced peaks are appeared. The two peaks in lower angles with the symmetric shapes

are assigned to ε-FeSi (110), and β-$FeSi_2$ (220)/(202), reflections [129]. The other two peaks in higher angles are asymmetric in shape due to the overlapping between different reflections from these two formed phases [128]. Using Gaussian fits (red and green curves in Fig 6.4a), it was able to decompose these two asymmetric peaks into two main components. The green Gaussians at 2θ = 31.7° and 33.89° are assigned to (210) and (211) reflections of the ε-FeSi phase, respectively [118]. The red Gaussians at 2θ = 31.84° and 33.78° are assigned to (040) and (422) reflections of the β-$FeSi_2$ phase, respectively [118]. It is clear from Fig. 6.4a that the annealed sample consists of both polycrystalline ε-FeSi and β-$FeSi_2$ phases, in which β-$FeSi_2$ is always dominant phase.

The larger the angle of incidence, the deeper the probed region of the sample. Therefore, the fact that the peak intensities decrease with an increase of the angle of incidence is proof for the silicide formation in the surface region. The observation of the more intense peaks at angular positions of three main peaks of the α and β phases suggests that a kind of epitaxy growth adjacent to the sample surface most likely was achieved.

Fig. 6.4b shows the variation of total integrated peak intensities associated with ε (green columns) and β (red columns) phases with incidence angle. While the integrated intensities of both β and ε phases increase by decreasing the incidence angle, the intensity ratio (I_ε/ I_β) of both peaks, as shown by dashed blue curve in Fig. 6.4b, increases from 18% at α_{in}=1° to 37.5% at α_{in}=0.2° over 33.5% at α_{in}=0.5°. This implies that the β-$FeSi_2$ phase lies between ε-FeSi layer and Si substrate. The formation of a periodic structure in Fe implanted Si(001) was also reported previously [131]. This finding is in agreement with Ishimaru *et al.*[129], who reported on the formation of the β-$FeSi_2$ layer between the topmost ε-FeSi layer and Si substrate. In other words, the β-$FeSi_2$ phase is grown close to the inner region of bulk Si(001) which is in agreement with the results of XPS and XANES analyses, showing the formation of Fe-silicides with higher Fe-component on upper part of the ripples (see subsections 5.1 and 5.2).

The β-$FeSi_2$ lattice parameters were determined from the GI-XRD spectra for different incidence angles. In table 6.1, these parameters are compared with the calculated values for the bulk unstrained β-$FeSi_2$ [134] as reference. The strain ε_a, ε_b, and ε_c along the crystal axes are calculated ($\varepsilon_a = (a-a_0) / a_0$, $\varepsilon_b = (b-b_0) / b_0$, $\varepsilon_c = (c-c_0) / c_0$) and given in table 6.1.

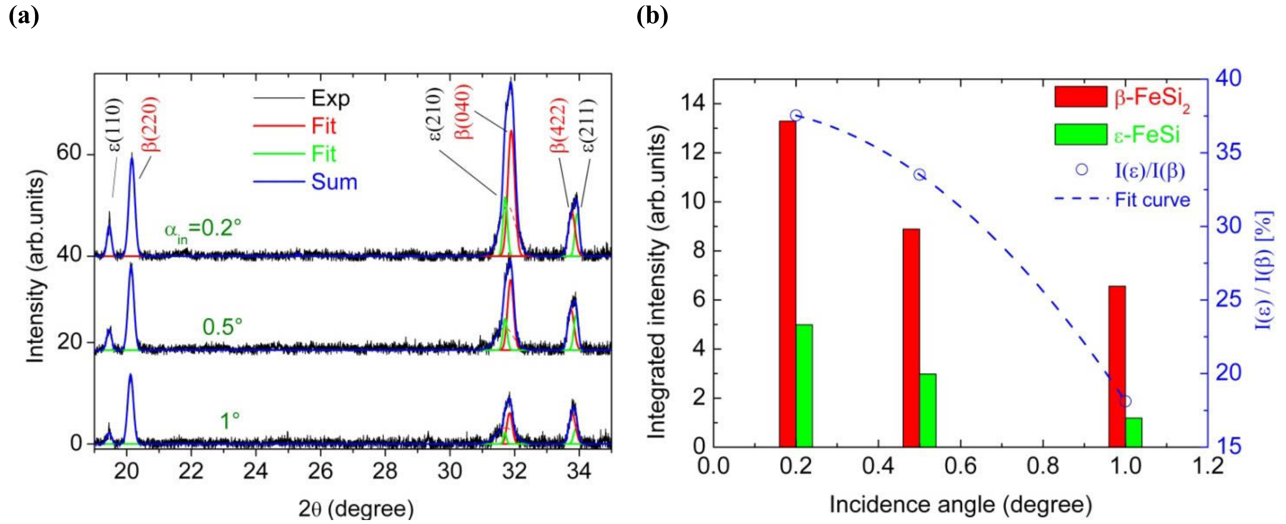

Figure. 6.4: (a) The measured GI-XRD spectra of the sample 4B (irradiated in off-normal with 20 KeV Fe ions at fluence of 5×10^{17} ions cm^{-2}) at annealing temperature of 800 °C at X-ray incidence angle of 0.2° (up), 0.5° (middle), and 1° (down) using λ=1.078 Å, and $\Delta 2\theta$=0.05°. (b) The variation of the total integrated intensities with incidence angles, calculated for β-$FeSi_2$ (red) and ε-FeSi (green). The dashed blue curve is a fit curve over open circles, indicating the variation of ratio of integrated intensity of ε-FeSi to β-$FeSi_2$ phases with incidence angles.

Table 6.1 Lattice parameters of β-$FeSi_2$ phase for the sample 4B at annealing temperature of 800°C, compared with calculated values for bulk β-$FeSi_2$ lattice parameters. The strain: ε_a, ε_b and ε_c along the crystal axes are calculated (ε_a=(a-a_0)/a_0, ε_b=(b-b_0)/b_0, ε_a=(c-c_0)/c_0) using the calculated values for bulk β-$FeSi_2$ lattice parameters from Ref. [134] , as reference.

Phases	a (Å)	b (Å)	c (Å)	ε_a (%)	ε_b(%)	ε_c (%)
ε-FeSi/Exp	4.511	4.511	4.511			1.302
ε-FeSi/calculated (bulk)	4.453	4.453	4.453			
β-$FeSi_2$/0.2° (Exp)	9.941	7.846	7.937	0.609	0.533	1.316
β-$FeSi_2$/0.5° (Exp)	9.963	7.851	7.913	0.834	0.601	1.00
β-$FeSi_2$/1° (Exp)	9.967	7.859	7.857	0.871	0.692	0.296
β-$FeSi_2$/calculated (bulk)	9.881	7.805	7.834			

It is seen that for all incidence angles, all lattice parameters are larger than the unstrained bulk values. By decreasing the incidence angle, the strain in direction of *c* axic increases while in directions of *a* and *b* axes decreases. A compression of *c* is expected due to the Poisson effect when a expansion of *a* and *b* occures in an attempt to match the substrate lattice parameters [69, 135].

the calculated lattice parameter for the ε-FeSi pahse for (110) reflection is a = 4.511 Å for all incidence angles that shows a strain of ε = 1.3 % in compare to bulk value 4.453 Å.

6.1.2 Structural evolution in low-fluence Fe ion irradiated Si upon thermal annealing

Fig. 6.5a shows the GI-XRD spectra of sample 1B, irradiated at fluence of 1×10^{16} ions cm^{-2}, for different annealing temperatures starting at RT (gray), 400°C (black), 500°C (orange), 600°C (red), 700°C (olive), and at 800°C (blue). While upto 500°C no diffraction peaks are observed, reaching 600°C the broadened diffraction peaks at the $2\theta \sim 31.7°$ and ~ 33.7° are appeared as a onset of recrystallization of amorphous Fe-silicides. By increasing the annealing temperature to 700°C and 800°C, these peaks become larger in intensity. In order to increase the surface sensitivity, the X-ray incidence angle was decreased close to the critical angle of total external reflection of Si ($\alpha_c = 0.155°$ at $\lambda = 1.078$ Å).

Fig. 6.5b shows the XRD spectra of this sample at 800°C at different incidence angles of 0.2°, 0.5°, 1° and 5° from top to bottom, respectively, measured with a step of $\Delta 2\theta = 0.05°$. At 5° incidence angle, only one peak is appeared at $2\theta = 24.43°$. This peak is assigned to ε-FeSi (111) reflection. By decreasing the incidence angle to 1°, six peaks are appeared in the diffraction spectra at the $2\theta = 20.45°$, 24.35°, 26.55°, 29.08°, 31.80°, and 33.85° which are assigned to β(220), ε(111), α(111), β(023), β(040), and α(211)/ β(422), respectively [118, 121]. At incidence angle of 0.5°, all peaks increase in intensity accompanied by unusual broadening of β(023) peak. This means that a particular orientation of β phase is dominance at the interface. By decreasing the incidence angle to 0.2°, almost all peaks increase in intensity, indicating the formation of crystalline silicides close to surface. The phase variation as a function of depth can be associated with a change of the Fe concentration profile [127].

The appearance of ε-FeSi(111) reflection at sample 1B shows that different ion fluence or layer thickness causes a critical variation of preferred orientation for ε-FeSi phase growth. A variation in growth orientation by varying implanted Fe concentration was reported for cubic $FeSi_2$ in Refs. [122, 127].

_ENREF_27The peak at $2\theta = 26.543°$ (d = 2.348 Å) is attributed to (111) reflection of α-$FeSi_2$ phase [128] which is absent in the sample 4B. The formation of α-$FeSi_2$ in our case can be compared with results of Tan *et al*. [136]. He reported that Fe implantation with a fluence in (1-3)$\times10^{17}$ cm^{-2} range results in formation of the α-$FeSi_2$ phase, but the β-$FeSi_2$ phase is formed only at a fluence about 5×10^{17} cm^{-2}. Upon annealing, the semiconducting β-$FeSi_2$ phase was formed in Fe-implanted samples independent from the ion fluence [136].

One important difference between α-$FeSi_2$ and β-$FeSi_2$ phases is that the first one has a much simpler crystal structure. Our observation suggests that the formation of α-$FeSi_2$ phase with a simple structure is more favored than the thermodynamically stable β-$FeSi_2$ phase with an orthorhombic structure when the ion fluence is low. Since the β-$FeSi_2$ can be considered as α-$FeSi_2$ having disordered atomic positions [136], by increasing ion fluence β-$FeSi_2$ formation dominants (no α-$FeSi_2$ peaks found at rough surfaces-see Fig. 6.4a).

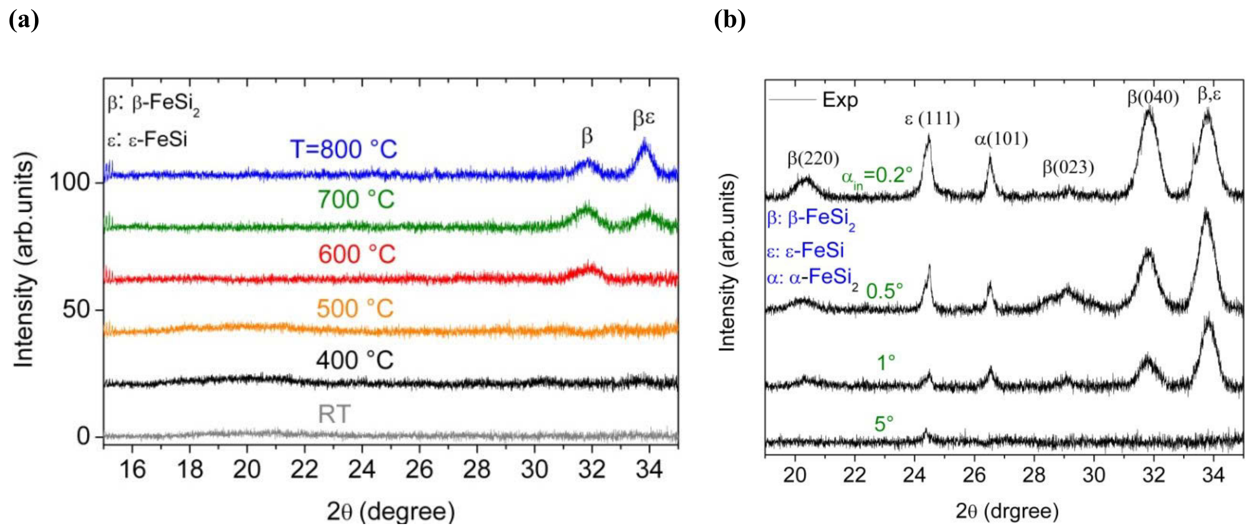

Figure. 6.5: (a) The measured GI-XRD spectra of the sample 1B (irradiated in off-normal with 20 KeV Fe ions at fluence of 1×10^{16} ions cm^{-2}) at 800 °C (blue), 700 °C (olive), 600 °C (red), 500°C (orange), 400°C (black), and room temperature-RT (gray) taken at incidence angle of α_{in}=1° with λ=1.078 Å, and $\Delta 2\theta$=0.1°. (b) GI-XRD spectra of the sample 1B at annealing temperature of 800°C at incidence angle of 0.2°, 0.5°, 1°, and 5°, from top to bottom, respectively, and $\Delta 2\theta$=0.05°.

6.2 Strain analysis

X-ray rocking curve analysis is a non-destructive technique for characterization of lattice strain. By comparing with theoretical rocking curves, profiles of lattice strain can be evaluated. Fig. 6.6a shows the rocking curves of Si(400) reflection of sample 1B at RT before (red curve) and after (blue curve) annealing at T=800°C. Prior to annealing, the signal of the implanted layer shows a shoulder on the low angle side of the substrate peak (but no fringes), indicating lattice expansion of the irradiated region in a direction perpendicular to the surface. Lattice expansion may be caused by interstitial and substitutional atoms as known from other X-ray studies of ion implanted Si [137, 138].

Fig. 6.6b shows the simulated reflection pattern (solid black surve) in comparison to measured (red open circles) one at room temperature. To simulate the strain as a function of

depth the implanted region is divided into a number of thin lamellae in which the strain is kept constant. The disordered parts of an ion implanted crystal may containe atoms which are randomly displaced from their ideal lattice sites causing a reduction of the reflectivity. This decrease of the X-ray reflectivity was taken into account considering a static Deby-Waller factor. The simulated strain profile is illustrated as inset of Fig. 6.6b. It can be seen that the ion beam induced strain reaches its maximum at the depth of around 5 nm below the surface and within a thickness of 5 nm. This thickness is comparable with the penetration depth of Fe ions obtained from X-ray reflectivity at room temperature (see inset of Fig. 4.8d).

After annealing at 800°C, several fringes appear at the left and right sides of the Si (400) reflection peak (see Fig. 6.6a). These fringes are caused by interference of X-rays reflected from the surface and from a buried amorphous-crystalline interface [139]. The thickness of the strained layer, t, may be determined from the angular distance $\delta\theta$ of the interference fringes using the equation [140]:

$$t = \lambda \sin(2\theta_B - \theta) / \delta\theta \sin 2\theta_B \quad (6.2)$$

where λ is the wavelength (1.078 Å), θ the angle at which the period is measured and $\delta\theta$ the fringe period. A thickness of about 28 nm is calculated using the given formula. This reveals that a thin film is formed during the annealing process.

The amount of average strain (neglecting the detailed depth dependence) can be determined from the angular separation between the position of the lowest angle oscillation and the position of the Si Bragg peak, using the equation [140]:

$$\delta a / a = -\delta\theta / \tan\theta_B \quad (6.3)$$

where $\delta\theta$ is the angle between the substrate peak and the peak of the strained layer, and θ_B is the Bragg angle (23.40° for the Si (400) reflection).

Fig. 6.6c shows the simulated reflection pattern (solid black curve) in comparison to measured (blue open circles) one at room temperature after annealing at 800°C. The simulated strain profile is illustrated as inset of Fig. 6.6c.

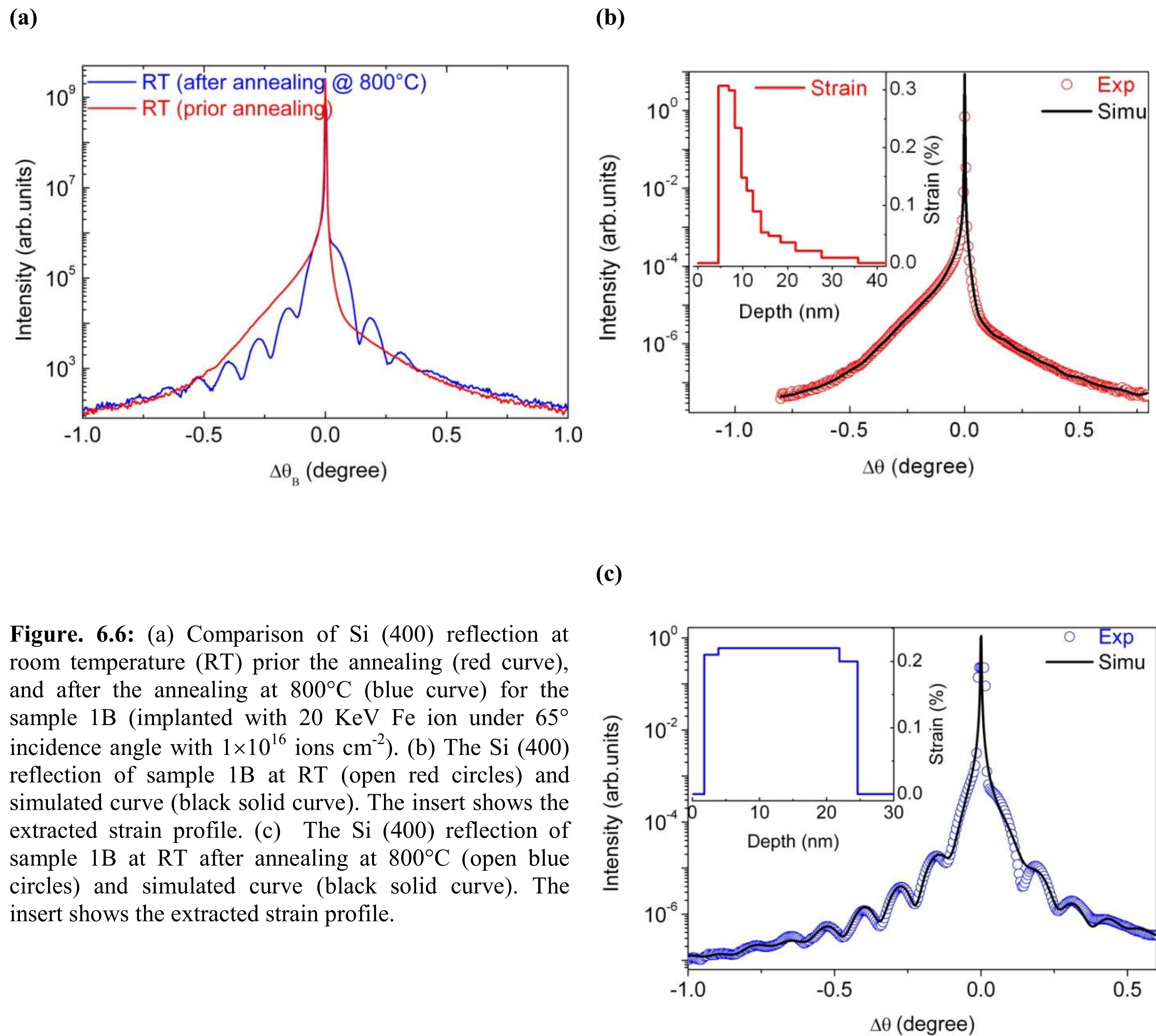

Figure. 6.6: (a) Comparison of Si (400) reflection at room temperature (RT) prior the annealing (red curve), and after the annealing at 800°C (blue curve) for the sample 1B (implanted with 20 KeV Fe ion under 65° incidence angle with 1×10^{16} ions cm^{-2}). (b) The Si (400) reflection of sample 1B at RT (open red circles) and simulated curve (black solid curve). The insert shows the extracted strain profile. (c) The Si (400) reflection of sample 1B at RT after annealing at 800°C (open blue circles) and simulated curve (black solid curve). The insert shows the extracted strain profile.

It seems that the recrystallization of amorphous Si between silicides and bulk Si substrate can be leads to such a modulation on reflection pattern. This interpretation can be confirmed by TEM analysis (see Fig. 4.6a) showing an amorphous bilayer consisting of amorphous Fe-Si and amorphous Si layers, formed on bulk Si. Furthermore, the recrystallization of amorphous Si in the case of high Fluence Fe implanted Si after annealing at 600°C has already been reported by Naito *et al*. [141], showing the formation of a periodic structure of recrystallized buried Si and silicide with different structure compared to the structure of a topmost layer.

Summary and discussion

In summary, the crystallization process of the amorphous Fe-Si layers, formed by a low and high fluence Fe ion irradiation on Si(100) substrates, was examined. The crystallization process was carried out by thermal annealing in which the samples were annealed in the range of RT and 800°C and characterized by GI-XRD during annealing.

Comparing the XRD spectra of a smooth surfac (low ion fluence) and a patterned surface (high ion fluence) shows that in the former case, the crystallization starts at a higher annealing temperature compared to the later one starting at 500°C. This can be related to the different thicknesses of a formed Fe-Si layer on the samples.

The depth profile of the recrystallized Fe-silicides was probed by grazing incidence X-ray diffraction. It revealed that the silicide with higher Fe content (ε-FeSi) is formed close to the surface, and changes to a lower Fe content phase (β-$FeSi_2$) at larger depths. While the polycrystalline β-$FeSi_2$ phase dominates at the irradiated sample with higher ion fluence, a nearly equal ratio between ε-FeSi and β-$FeSi_2$ phases is found at irradiated sample with lower ion fluence. The formation of two equilibrium FeSi and $FeSi_2$ phases was reported by Desimoni *at al*. [131], and their formation temperatures are slightly dependent on the layer thicknesses.

These findings for crystallized silicides are in agreement with the findings by XPS and XAS analyses on amorphous silicides formed on the as-irradiated samples (see chapter 5), showing a formation of Fe-rich silicide (Fe_3Si) on the topmost layer changing to Si-rich silicide ($FeSi_2$) towards buried layers. Here it should be mentioned that the Fe_3Si phase is stable at low temperatures and can not survive at high annealing temperatures.

These findings confirm that small silicides moieties are already formed during the irradiation process. Furthermore, various formed phases are distributed with different ratios within a Fe-Si layer at low and high fluence Fe ion irradiated Si. This suggests that the resulting density inhomogeneity along the surface can be considered as the relevant factor in the process of pattern formation.

7 Ion beam induced pattern formation on Si(001) with incorporation of metal atom impurities

In this chapter it is shown that for a normal and near normal Kr ion incidence, a pattern formation can be developed on Si(001) surfaces due to incorporation of metal impurities like Fe and Cr atoms with a certain amount, offering a new degree of freedom for pattern control. However, to understand the mechanisms being responsible for pattern formation in the presence of metallic atoms, the depth profiling and the chemical state of the metal atoms is required.

In section 7.1, the pattern formation on Si(001) surface using a Kaufman type broad-beam ion source is reported. The Si substrate is bombarded at room temperature with Kr ions in the presence of co-sputtering metal atoms stemming from the ion source itself. X-ray reflectivity (XRR) is used for quantitative determination of depth profiles of the incorporated metal atoms in the irradiated samples. X-ray absorption near edge spectroscopy (XANES) under a grazing incidence angle was used to probe the chemical states of incorporated iron atoms. In section 7.2, the pattern formation on Si(001) wafers using a focused beam ion source is presented. The Si surface is bombarded with Kr ions with simultaneous incorporation of co-evaporated Fe atoms by an e-beam evaporator. X-ray photoelectron spectroscopy (XPS) and X-ray absorption spectroscopy (XAS) under grazing incidence angles were used to probe the chemical states of incorporated iron atoms.

7.1 Ion beam-induced pattern formation in presence of metal atom impurities using a broad-beam ion source

Samples

Two Si(001) substrates were bombarded at room temperature with Kr ions using a Kaufman-type broad-beam ion source. During the ion bombardment, impurity atoms stemming from ion source itself are incorporated in ion sputtering process. The Fe and Cr atoms are sputtered from a stainless steel lining between the extraction system and the sample holder, where Fe is the main component. The co-sputtering Fe/Cr concentration is determined by the divergence of the beam which is controlled by the acceleration voltage U_{acc} of the ion source. While at an acceleration voltage of U_{acc} = -1000 V a large divergence (7°) of the ion beam leads to co-sputtering of material from the lining and hence the deposition of Fe atoms on the sample, a smaller acceleration voltage of U_{acc} = -200 V results in a significantly smaller Fe flux on the sample. The samples were not rotated during the irradiation (for more details see Refs. [46, 142]). Table 7.1 summarizes the sputtering parameters used for the different samples.

Table 7.1 Sputtering parameters of irradiated Si(001) wafers using Kaufman-type broad-beam ion source. The incidence angle of ion beam with respect to the surface normal (α_{ion}) and ion beam energy (E_{ion}) are identical for two samples.

Sample number	Kr^+ ion-Fluence [ions cm^{-2}]	α_{ion}	E_{ion} [KeV]	U_{acc} [V]	Areal density [10^{15} cm^{-2}]	
					Fe	Cr
1L	3.4×10^{18}	15°	2	-1000	1.92	0.44
2L	3.4×10^{18}	15°	2	-200	0.55	0.22

Results and discussion

AFM analysis

Prior to X-ray analysis the surface morphology of the samples have been analysed by using AFM. In Fig. 7.1a, the AFM image of sample 1L shows a surface pattern with discontinuous ripples oriented perpendicular to the ion beam and root mean square (RMS) roughness of 1.05 nm, whereas the Fig. 7.1b shows the AFM image of sample 2L with a smooth surface and RMS roughness of 0.22 nm. The lateral correlations of self-organized structures were evaluated by using two-dimensional fast Fourier transformation (2D FFT). The position of the first order maximum with respect to the origin in the FFT is inversely proportional to the wavelength. The FFT image (inset of Fig. 7.1a) shows a lateral ordering for the sample 1L with ripple wavelength of around 65 nm. In contrast to sample 1L there is no ordering for sample 2L (inset of Fig. 7.1b). Both samples were prepared with the same sputtering parameters with the exception of acceleration voltage U_{acc} which controls the stationary Fe areal density in the surface. RBS analysis shows the areal densities of 1.92×10^{15} cm^{-2} for sample 1L and 0.55×10^{15} cm^{-2} for sample 2L, respectively. Thus, it is assumed that the pattern formation on sample 1L is attributed to the enhanced incorporation of metal atoms.

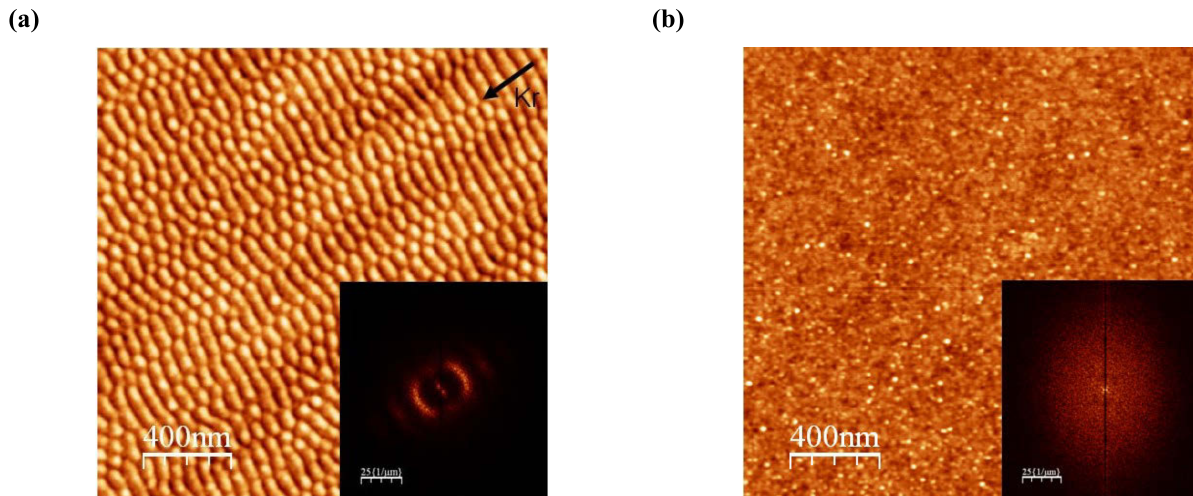

Figure. 7.1 AFM images (2 μm × 2μm) and corresponding Fourier images of Si(001) surface of sample 1L (a) with Fe areal density of 1.92×10^{15} cm^{-2} (z = 6 nm) and sample 2L (b) with Fe areal density of 0.55×10^{15} cm^{-2} (z = 6 nm). The value z is the height difference corresponding to the image contrast between the white and black.

XRR and SIMS analysis

The depth density profile of metal atoms was analyzed quantitatively by XRR. Fig. 7.2a shows the measured (open circles) and simulated (solid lines) X-ray reflectivity curves of samples 1L (red curve) and 2L (blue curve). For angles $\alpha_i > \alpha_c$ (critical angle or total external reflection), XRR curve of the sample 2L shows thickness oscillations indicating a layering of metal atoms close to the surface. This layering is hard to see for sample 1L. The simulation of XRR curves provides the concentration of co-sputtered metals as a function of depth. To do this, the near surface region is divided into a number of thin lamellae with constant electron density. Both thickness and density of each lamella were varied until a coincidence between measured and simulated curves is reached. The corresponding electron density profiles were interpreted by an artificial solid solution $Si_{(1-x)}$ Me_x where Me stands for Fe and Cr, because both metals have very similar electron densities which are indistinguishable by simulation.

The inset of Fig. 7.2a shows Me concentration x as a function of depth obtained from XRR simulation. It can be seen that the metal concentration appears largest in the center of the metallic layer. The maximum metal concentration is found at a depth of around 3.5 nm and 1.6 nm for samples 1L and 2L respectively. Comparing the evaluated density profiles of both samples seen in the inset of Fig. 7.2a, it can be concluded that maximum metal concentration is not on top but slightly below the surface, in the upper part of ripples. The total thickness of the metal layer is 8 nm but 4 nm for sample 1L and 2L, respectively. The drop of intensity for increasing incidence angle is attributed to the surface roughness (σ). It is σ = 1.07 nm for the sample 1L and σ = 0.23 nm for the sample 2L. The larger thickness of the metal layer and the higher surface roughness correlates with the appearance of patterning in sample 1L, whereas lower roughness and smaller metal depth is found for the sample without surface pattering. The XRR results are well confirmed by SIMS profile measurements (Fig. 7.2b). In agreement with XRR we obtain a distribution with 1/e thickness of 8 nm and a maximum of the distribution curve at 3.5 nm for sample 1L (Fig. 7.2c) and 3.5 nm with maximum of the distribution curve at 1.6 nm for sample 2L (Fig. 7.2d). From SIMS it is seen that the amount of Cr is about 20 – 30 % of the Fe content. So Cr is only a minor contribution.

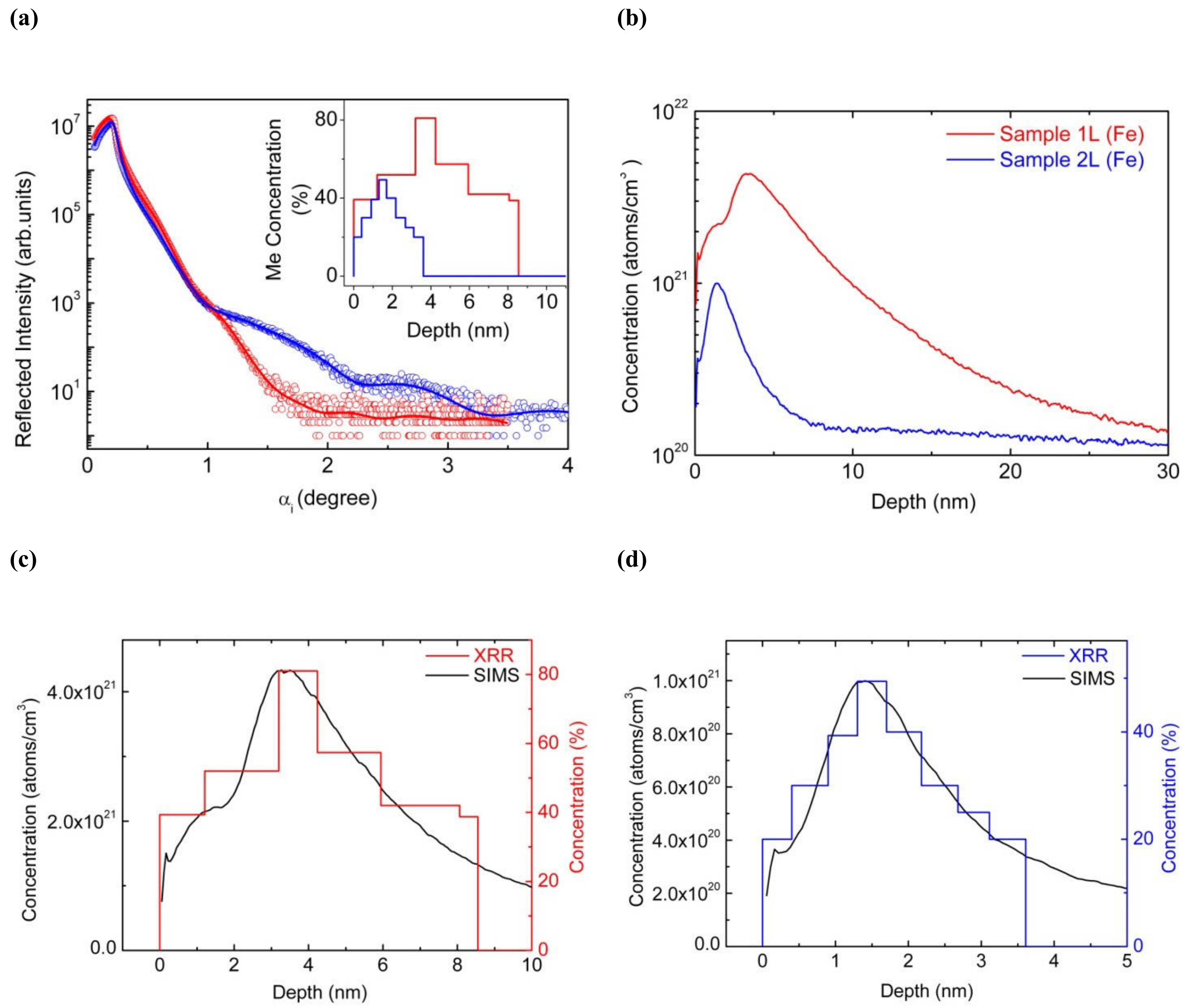

Figure. 7.2 (a) Specular X-ray reflectivity measurements (open circles), calculated (solid line) and depth profiles (inserts) of Me atoms for samples 1L (red) and 2L (blue). (b) SIMS profiles of samples 1L (red curve) and 2L (blue curve). (c) Comparison of XRR (red) and SIMS (black) for sample 1L. (d) Comparison of XRR (blue) and SIMS (black) for sample 2L.

XANES analysis

The XANES spectra of sample 1L with ripple like surface and for sample 2L with smooth surface are presented in Figs. 7.3a-b, respectively, taken in vicinity of the Fe-K edge at 7112 eV under grazing incidence angle of X-ray varying from 0.1° to 0.35°. All spectra show nearly uniform shape except for sample 1L in the region $\alpha_i < \alpha_c$. For the latter case, the XANES spectrum (black curve in Fig. 7.3a) shows a shift toward lower photon energy compared to spectra taken at higher incidence angles. Comparing with XANES spectra of reference samples (see Fig. 5.5c), it can be concluded that a Fe-rich silicide is appeared in the near surface region but the dominance of Si-rich silicide for larger depth. For the sample 2L with smooth surface, XANES spectra are identical for all penetration depth and are dominated by the Si-rich silicide. In other words, pattern formation is accompanied with an enhancement of the iron concentration near the surface

For further analysis the XANES data are fitted with a linear combination of different standard phases. The fitting reveals that for all incidence angles the contribution of the $FeSi_2$ phase dominates. In addition we found a content of 25% of Fe_3Si in the subsurface region of sample 1L but only 12% in sample 2L. In sample 1L the concentration of the Fe-rich phases decreases drastically for larger incidence angles and the related increase of the penetration depth. This variation is not obvious for sample 2L because the spectra do not vary with different incidence angles. The fitting result indicate that the XANES spectrum of the sample 2L always is dominated by $FeSi_2$ and the Fe_3Si is only a minority phase (9% in $\alpha_i = 0.22°$). Since the only different parameter of samples 1L and 2L is the concentration of metal atoms, pattern formation at the surface can be related to the appearance of the Fe_3Si phases in the irradiated region.

(a)

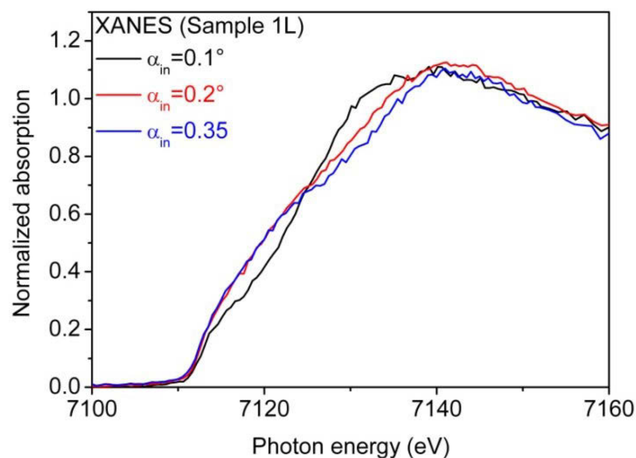

(b)

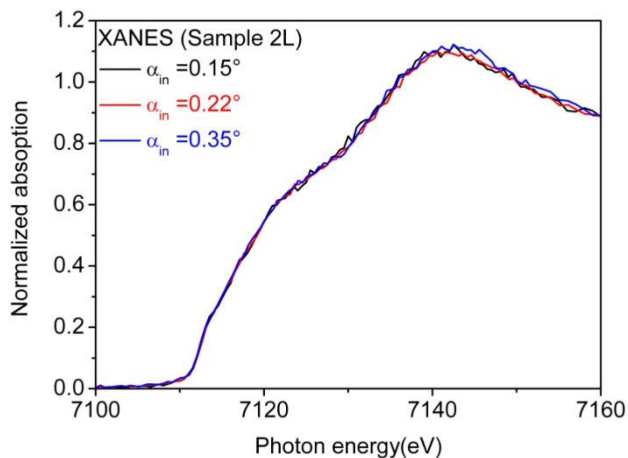

Figure. 7.3 Comparison of normalized Fe K-edge XANES spectra at different X-ray incidence angles of 0.1° (black) , 0.2° (red) and 0.35° (blue) for sample 1L at Fe K edge. (b) comparison of normalized Fe K-edge XANES spectra at different X-ray incidence angles of 0.15° (black) , 0.22° (red), 0.35°(blue), for sample 2L.

7.2 Ion beam induced pattern formation in presence of co-evaporation of Fe using a focused-beam ion source

In this section, ion beam induced pattern formation under co-evaporation of Fe atoms during Kr ion exposure on the Si(001) surface using focused beam ion source is investigated. The sketch of deposition geometry is illustrated in Fig. 7.4a. The 2 KeV Kr ions with a full-width at half-maximum of ≈ 1 mm was scanned over the sample with fluence of 6×10^{17} ions cm^{-2} at normal incidence and Fe atom was co-evaporated from an e-beam evaporator at an incidence angle of 60° with respect to the surface normal during ion exposure. The amount of co-evaporated material is characterized by the atom-to-ion ratio φ_{Fe} / φ_{Kr} = 0.09±0.01 (n_{Fe} = $(4.67\pm0.14)\times10^{15}$ cm^{-2}). For more details see Ref. [143]. After preparation, the sample which is named 1D was imaged by scanning tunneling microscopy (STM).

Results and discussion

STM analysis

Fig. 7.4b shows STM observation of Si(001) taken after co-evaporation during Kr ion beam exposure. Ripple like features are formed on the surface with roughness of σ = 3.1 nm. The height difference spanned by the image contrast between white and black is Δz = 16 nm. The black arrow visualize the projected direction of incoming Fe atoms.

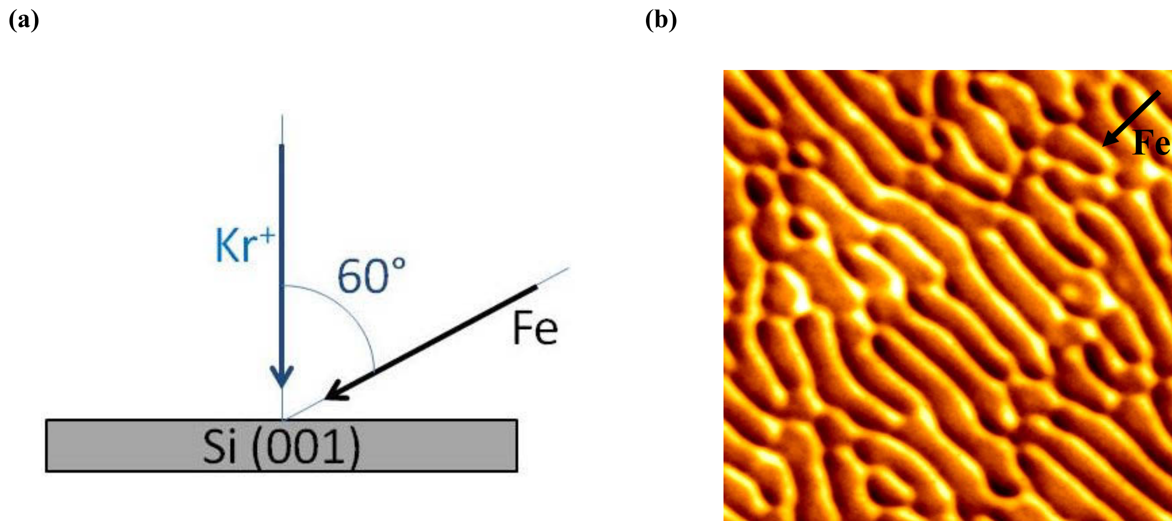

Figure. 7.4 (a). Sketch of deposition geometry for co-evaporation experiment. (b) STM image of Si(001) after Fe co-evaporation during a exposure of 2 KeV Kr ions at fluence of 6×10^{17} ions cm^{-2} under normal incidence. The atom-to-ion flux ratio is $\varphi_{Fe}/\varphi_{Kr} = 0.09 \pm 0.01$ and $n_{Fe} = (4.67 \pm 0.14) \times 10^{15}\ cm^{-2}$. The image size is 1 µm × 1 µm.

X-ray photoelectron spectroscopy (XPS)

XPS survey scan of sample 1D was taken with 23.42 eV pass energy at excitation energy of 180 eV. This survey scan is shown in Fig. 7.5a (blue curve) in the range of $0 < BE < 120$ eV and compared with survey scan of sample 4A (black curve), the patterned surface sample which was prepared by irradiation of direct off-normal Fe ions (see table 4.1). The two survey scans are overally quite similar. This means, the electronic structure of two patterned surface samples are similar. The detailed explanation of observed A, B ,C peaks on the spectra of Fig. 7.5a were already given in subsection 5.1. A small relative intensity of peak A for sample 1D suggests that a smaller amount of Fe-silicide is forms on this sample compared to sample 4A. This is in agreement qualitatively with the results of the RBS measurement that give a higher total Fe concentration of $1\times10^{16}\ cm^{-2}$ for sample 4A compared with $4.67\times10^{15}\ cm^{-2}$ for sample 1D. Furthermore, relatively higher intensity of peak B for sample 1D shows the formation of thicker oxidation layer on sample 1D compared to sample 4A. The lower amount of Fe atoms and higher degree of oxidation layer on sample 1D causes the suppress of Fe 3p peak on survey spectrum of this sample.

For confirmation of the chemical reaction between Fe and Si atoms at sample 1D, a high resolution XPS measurement of Si 2p core levele was taken into account. Considering a few monolayer (ML) deposited Fe atoms on the surface, excitaion energy of 180 eV with pass energy of 2.33 eV providing energy resolution less than 0.1 eV was chosen for higher surface senstivity.

Fig. 7.5b shows the Si 2p core level spectra of sample 1D which can be fitted by four Gaussian peaks (red crves in Fig. 7.5b) with a Shirley type background. The two peaks at about 103.8 eV and 102.2 eV are assigned to SiO_2 and a silicon suboxide SiO_{2-x}, respectively [106]. Those compounds will always form due to the air exposure of the samples after removal from the irradiation chamber. The other two peaks at 99.55 eV and 100.25 eV are ascribed to the spin-orbit splitted levels of Si $2p_{3/2}$ and Si $2p_{1/2}$. In particular the FWHM of the Si $2p_{3/2}$ and Si $2p_{1/2}$ core levels are estimated to be about 0.6 eV. In comparison with reported value of Si $2p_{3/2}$ core levels for different phase of Fe-silicides by Egert and Panzner [105], the found value for the sample 1D coinside with Fe-rich silicide (Fe_3Si). This results also are in agreement with the obtained value for the sample 4A (see Fig 5.2a).

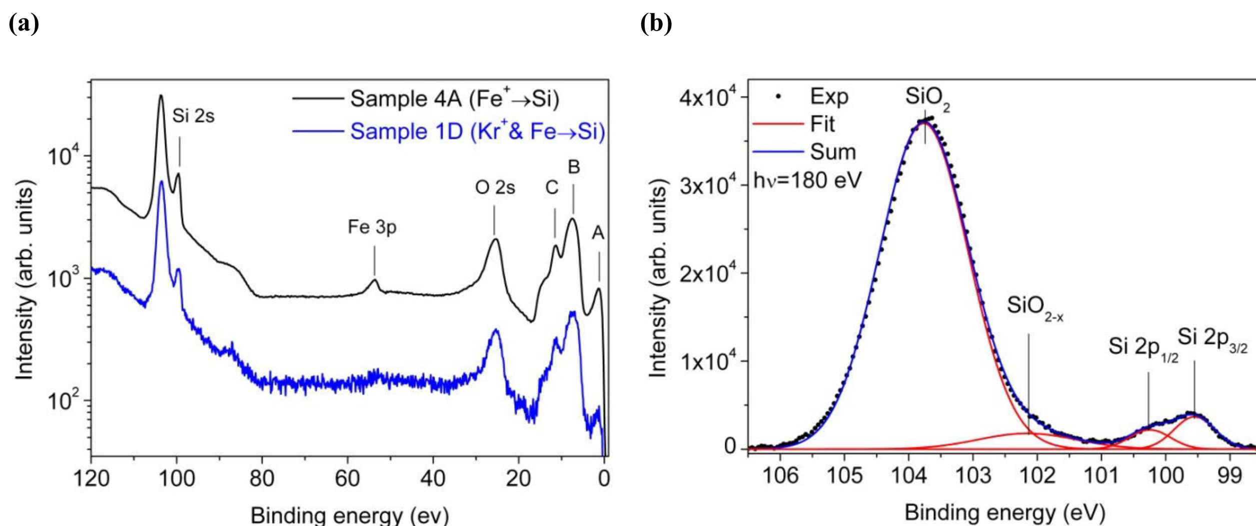

Figure. 7.5. (a) Comparision between survey scan X-ray photoemission spectra of two patterned Si(001) surfaces which were prepared by two different methods. Black curve: correspond to an irradiated surface with direct off-normal Fe ions, sample 4A. Blue curve: correspond to a sputter co-evaporated surface, sample 1D. See text for explanation of peaks A, B, C. (b) Si 2p core level spectra of sample 1D with measured data (full circles). After subtraction of a Shirley type background, the measured data were fitted by four Gaussians (blue sum curve). The excitation energy is hν = 180 eV.

Therfore, the sample 1D can be interpreted qualitatively in similar way as sample 4A, i.e. the formed Fe-rich silicide on topmost layer changed to Si-rich silicide towards the depth. For monitoring the chemical state of Fe atoms at intefeces, XAS analysis was performed in the vicinity of the Fe K-edge for sample 1D.

XAS analysis

Fig. 7.6a shows the comparison of normalized extended X-ray absorption (EXAFS) spectra of sample 1D (red curve) with sample 4A (black curve) at α_{in}=0.5° > α_c=0.22° (critical angle of Si). Except a small difference at intensity value due to the smaller amount of Fe atoms on sample 1D, the peak maxima of both spectra located at 7.140 keV, 7.190 keV and 7.255 keV coincide very well to each other and with those of the $FeSi_2$ reference spectrum (blue curve in Fig. 5.6b). In other words, the $FeSi_2$ formation is dominant for larger depths for the sample 1D as well. Magnified views of the X-ray absorption near edge structure (XANES) of the samples 1D (red curve) and 4A (black curve) are presented at insert of Fig. 7.6a. The similar spectra indicate a similar chemical state of Fe atoms in both samples.

Fig. 7.6b shows EXAFS spectra of sample 1D at α_{in}=0.5° (red curve) and α_{in}=0.1°< α_c (blue curve). By reducing the incidence angle to 0.1° the EXAFS spectrum is modulated so that appearance of a peak at 7.220 KeV is coincide with a peak position at EXAFS spectrum of Fe_3Si reference (see Fig.5.6b). A trend of modulation of EXAFS spectra towards Fe-rich silicides by reducing incidence angle is in agreement with our finding from XPS results showing a formation of Fe-rich silicide at the outer surface. The comparison between XANES spectra of sample 1D at these two incidence angle of 0.1° and 0.5° is illustrated as insert of Fig. 7.5b. No pronounced shift at peak position can be attributed to less surface sensitivity at the α_{in}=0.1° by reminding that the thickness of Fe atoms is limited to a few ML.

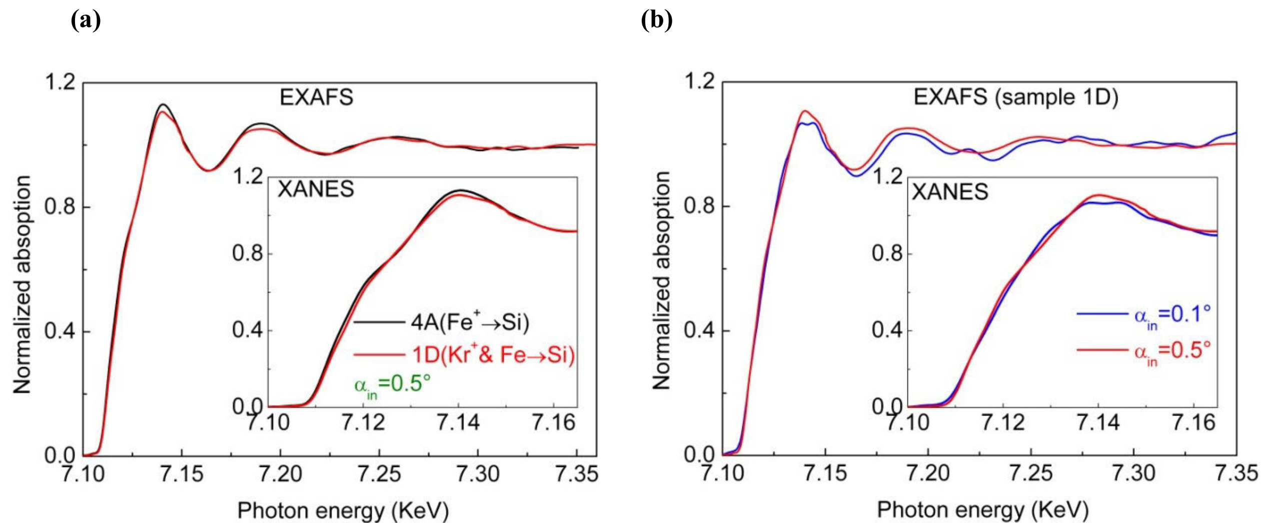

Figure. 7.6 (a) Comparison of normalized Fe K-edge EXAFS and XANES (insert) spectra of two patterned Si(001) surfaces which were prepared by two different methods. Black curves: EXAFS (XANES) spectra correspond to an irradiated surface with direct off-normal Fe ions, sample 4A. Red curves: EXAFS (XANES) spectra correspond to a sputter co-evaporated surface, sample 1D. (b) comparison of normalized EXAFS and XANES (insert) spectra at different X-ray incidence angles of 0.1° (blue) , and 0.5° (red) for sample 1D at Fe K-edge.

Summary and discussion

The role of the incorporation of the metal atom impurities during ion beam-induced pattern formation on Si(001) surfaces was investigated. Si wafers were bombarded with 2 KeV Kr ions using a broad beam and focused beam ion sources. While no pattern is formed on Si surfaces for a normal or near normal ion incidence, incorporation of Fe atoms at a certain amount during the ion irradiation process leads to the formation of patterns (ripples) on the surface.

In the case of a broad ion beam source, It was observed that for a near-normal ion incidence, pattern formation on the surface occurs when the stationary Fe areal density of the surface exceeds a certain threshold. Whereas for a lower concentration of metal atoms, the surface remains smooth, ripples appear for higher metal concentrations. The XRR showed that for the smooth surface, metal atoms are distributed at a lower depth compare to a patterned surface. Grazing-incidence XANES measurements showed that for metal concentrations smaller than a certain threshold Si-rich silicides are formed at the smooth surface, while for higher metal

concentrations the pattern formation on the surface is accompanied by the formation of Fe-rich silicides.

In the case of sputter co-evaporation of Fe on Si(001), while XPS analysis shows the formation of Fe-rich silicides at an outer surface, XAS analysis indicates a dominance of Si-rich silicide with a structure similar to that of $FeSi_2$ at an inner interface towards the Si crystal.

8 Summary and conclusions

In the present work, the self-organized pattern formation on Si(100) surfaces under direct Fe ion bombardment, at ion energies of 20 KeV and 5 KeV was investigated. The ripple formation occurs if the ion fluences exceeds a value of about 1×10^{16} ions cm^{-2}, and the specific properties of the formed ripples (wavelength and amplitude) on the surfaces vary by variation of ion beam parameters (ion energy and fluence). For adequate modeling of surface patterning, identification of relevant active parameters is a prerequisite. It is the aim of our investigation to separate and distinguish these relevant factors. Depth resolved investigations using nondestructive X-ray methods were applied to identify the active factors affecting the pattering mechanism.

X-ray reflectivity (XRR) revealed the formation of a few nm thick sub-surface layers containing the incorporated Fe ions. The newly applied method of extremely asymmetric diffraction (EAD) revealed a net reduction of the surface density scaling with the ion parameters. Ion beam induced net reduction of the surface densities at the patterned surfaces can be explained by the high surface roughness induced by the pattern formation, while at the smooth surfaces this leads to the conclusion that the process of pattern formation could already be started at an Fe fluence lower than $\sim 10^{16}$ ion cm^{-2}. Obtained results for 2 KeV ion energy and lower ion fluence (5×10^{14} ion cm^{-2}) confirm that there is a threshold of ion fluence leading to surface density modulation. Thus, it can be concluded that the systematical variation of surface density with irradiation parameters can be considered as the important parameter related to the patterning mechanism.

The X-ray photoelectron (XPS) and absorption spectroscopy (XAS) analyses revealed that Fe is chemically bonded in a Si framework within a thin surface layer and the Fe concentration of silicides changes with depth. The atomic coordination is similar to an Fe-rich silicide at the outer surface, while a Si-rich silicide with a structure similar to that of $FeSi_2$ is found at the inner interface towards the Si(001) crystal. It is concluded that pattern formation is strongly influenced by the formation of Fe-silicides near the surface. Since the different stoichiometries of Fe-silicides have different cohesive energies [115], they have different surface binding energies resulting in different sputtering yields. Therefore, different areas along the surface will exhibit different sputter yields that influence the process of ion beam erosion and may even lead to an enhancement of processes that are responsible for the ripple formation.

The recrystallization process of the pre-formed amorphous Fe-Si layer was carried out by thermal treatment in which the samples were annealed in the range of room temperature to about 800°C. The samples were characterized by grazing incidence X-ray diffraction (GI-XRD) during annealing. Depth profiling by GI-XRD for the patterned surfaces confirmed that the silicides with a higher Fe content (ε-FeSi) are formed on the topmost layer changing to the silicides with a lower Fe content (β-$FeSi_2$) towards further depths. This finding for crystallized silicides is in agreement with results of XPS and XAS analyses taken at amorphous silicides, formed in the as-irradiated samples. The formed phases are distributed with different ratios within a Fe-Si layer depending to ion fluence. The phase distribution is related to the Fe concentration profile and can be considered as the relevant factor in the process of pattern formation.

The role of incorporated metal impurities acting as a second component during normal ion beam-induced pattern formation on Si(001) surfaces was investigated. Pattern formation on the surface occurs when the stationary Fe areal density in the surface exceeds a certain threshold. The XRR shows that for smooth surfaces the metal atoms are distributed in a lower depth in comparison to patterned surfaces. While XPS analysis shows the formation of a Fe-rich silicide at an outer surface, XAS analysis indicates a dominance of Si-rich silicide with a structure similar to that of $FeSi_2$ at an inner interface towards the Si crystal.

These findings imply that the incorporated Fe atoms during ion beam irradiation of Si(001) surfaces have a similar electronic modulation to Fe ions when directly irradiated on Si surfaces. Considering that the curvature-dependent sputtering and the stress-induced instability are not relevant for surface instability in the case of sputter co-evaporation of Fe on Si(001) [143], it can be concluded that chemical reaction between Fe and Si atoms acts as a relevance active factor for ion beam-induced pattern formation during co-deposition. These results can be compared to the prediction of Bradley and Shipman's theory, in which the surface of an ion-bombarded solid is destabilized by the concurrent deposition of immobile impurities, provided that the impurity flux exceeds a critical value [144].

Acknowledgements

Many people collaborated on this work in order for it to be accomplished successfully.

Foremost, I would like to express my sincere gratitude to my advisor Prof. Dr. Dr. h.c. Ullrich Pietsch for the continuous support of my PhD study and research, for his patience, motivation, enthusiasm, and immense knowledge. His guidance helped me all the time during the research and writing of this thesis.

Besides my advisor, I would like to thank Prof. Dr. Dr. h.c. Bernd Rauschenbach, Prof. Dr. Hans D. Dahmen, and Prof. Dr. Christian Gutt, for being members of my PhD committee, and providing me with a thorough evaluation of my thesis.

I would like to express my gratitude to Dr. Andreas Biermanns-Föth for his assistance and helpful discussion during some phases of this work and Dr. Bahia Arezki, former member of our group, who invested some of her time helping me during the first step.

I would like to give thanks to the colleagues at IOM, in particular Dr. Frank Frost and Dr. Marina Cornejo (former member) for their sample preparation, AFM, RBS, and SIMS measurements and helpful discussions.

I would like to thank the colleagues at HZDR in particular Dr. Stefan Facsko and Dr. Jörg Grenzer for their insightful discussions and samples preparation and some AFM and RBS measurements, and also Dr. René Hübner for the TEM measurements.

I would like to thank Dr. Sven Macko, and Martin Engler from the department of physics, Faculty of Mathematics and Natural Sciences, at the University of Cologne for the sample preparation and STM analysis.

I would like to express my appreciation to Dr. Dirk Lützenkirchen-Hecht, from the faculty of physics at the University of Wuppertal, for his excellent support at the home lab facilities for XPS analysis and XAS measurements at BL-8 at DELTA, accompanied by meaningful advice and stimulating discussion.

I would like to thank beamline scientists Ralph Wagner at BL-8, Dr. Ulf Berges, Dominique Handschak and Frank Schönbohm, at BL-11 at DELTA, Dr. Stephen Doyle at PDIF beamline at ANKA and Dr. Carsten Baehtz at BM-20 at ESRF for the excellent support of the synchrotron experiments.

In addition, I would like to express my sincere thanks to the former and present colleagues who have helped me during the exhausting beamtimes while losing a lot of sleep in the process.

I would like to thank all the former and present members of the Solid State Physics group at University of Siegen for the valuable discussion and for providing a friendly environment in the group.

Finally, I would like to thank my parents for supporting me spiritually throughout my life.

This work has been supported by the Deutsche Forschungsgemeinschaft through FOR 845.

Bibliography

1. Oechsner, H., *R. Behrisch, G. Betz, G. Carter, B. Navinsek, J. Roth, BMU Scherzer, PD Townsend, GK Wehner, JL Whitton: Sputtering by Particle Bombardment II, Springer-Verlag Berlin, Heidelberg, New York, Tokyo 1983. 391 Seiten, Preis:DM 109,*Berichte der Bunsengesellschaft für physikalische Chemie, 1984. **88**(8): p. 779-779.

2. Carter, G., *Proposals for producing novel periodic structures by ion bombardment sputtering.* Vacuum, 2004. **77**(1): p. 97-100.

3. Makeev, M.A., R. Cuerno, and A.-L. Barabási, *Morphology of ion-sputtered surfaces.* Nuclear Instruments and Methods in Physics Research Section B: Beam Interactions with Materials and Atoms, 2002. **197**(3): p. 185-227.

4. Cahill, D.G., *Morphological instabilities in thin-film growth and etching.* Journal of Vacuum Science & Technology A: Vacuum, Surfaces, and Films, 2003. **21**(5): p. S110-S116.

5. Teichert, C., *Self-organized semiconductor surfaces as templates for nanostructured magnetic thin films.* Applied Physics A: Materials Science & Processing, 2003. **76**(5): p. 653-664.

6. Teichert, C., J. de Miguel, and T. Bobek, *Ion beam sputtered nanostructured semiconductor surfaces as templates for nanomagnet arrays.* Journal of Physics: Condensed Matter, 2009. **21**(22): p. 224025.

7. Ziberi, B., et al., *Importance of ion beam parameters on self-organized pattern formation on semiconductor surfaces by ion beam erosion.* Thin Solid Films, 2004. **459**(1): p. 106-110.

8. Facsko, S., et al., *Formation of ordered nanoscale semiconductor dots by ion sputtering.* Science, 1999. **285**(5433): p. 1551-1553.

9. Frost, F., et al., *Surface engineering with ion beams: from self-organized nanostructures to ultra-smooth surfaces.* Applied Physics A: Materials Science & Processing, 2008. **91**(4): p. 551-559.

10. Kree, R., T. Yasseri, and A. Hartmann, *Surfactant Sputtering: Theory of a new method of surface nanostructuring by ion beams.* Nuclear Instruments and Methods in Physics Research Section B: Beam Interactions with Materials and Atoms, 2009. **267**(8): p. 1403-1406.

11. Zhou, J. and M. Lu, *Mechanism of Fe impurity motivated ion-nanopatterning of Si (100) surfaces.* Physical Review B, 2010. **82**(12): p. 125404.

12. Bradley, R.M. and P.D. Shipman, *A surface layer of altered composition can play a key role in nanoscale pattern formation induced by ion bombardment.* Applied Surface Science, 2012. **258**: P. 4161-4170.

13. Bradley, R.M., *Producing ripple topographies by ion bombardment with codeposition of impurities: A curvature-dependent sputter yield is not required.* Physical Review B, 2012. **85**(11): p. 115419.

14. Bradley, R.M., *Nanoscale patterns produced by ion erosion of a solid with codeposition of impurities: The crucial effect of compound formation.* Physical Review B, 2013. **87**(20): p. 205408.

15. Carter, G. and V. Vishnyakov, *Roughening and ripple instabilities on ion-bombarded Si.* Physical Review B, 1996. **54**(24): p. 17647.

16. Chason, E., et al., *Roughening instability and evolution of the Ge (001) surface during ion sputtering.* Physical review letters, 1994. **72**(19): p. 3040.

17. Rusponi, S., et al., *Ripple wave vector rotation in anisotropic crystal sputtering.* Physical review letters, 1998. **81**(13): p. 2735.

18. Carter, G., et al., *Sputtering by particle bombardment II.* Topics in Applied Physics, 1983. **52**: p. 231.

19. Knystautas, E., *Engineering thin films and nanostructures with ion beams,* 2005: CRC Press.

20. Nastasi, M.A. and J.W. Mayer, *Ion implantation and synthesis of materials*. Vol. 80. 2006: Springer Verlag.

21. Sigmund, P., *Sputtering by ion bombardment theoretical concepts*1981: Springer.

22. Nastasi, M. and J.W. Mayer, *Ion implantation and synthesis of materials* 2006: Springer.

23. Charles, K., *Introduction to solid state physics*1987: Wiley Eastern Limited.

24. Chason, E., T. Mayer, and B. Kellerman. *Sputter roughening instability on the Ge (001) surface: Energy and flux dependence*. in *MRS Proceedings*. 1995. Cambridge Univ Press.

25. Chan, W.L. and E. Chason, *Making waves: kinetic processes controlling surface evolution during low energy ion sputtering.* Journal of Applied Physics, 2007. **101**: p. 121301.

26. Herring, C., *Effect of change of scale on sintering phenomena.* Journal of Applied Physics, 1950. **21**(4): p. 301-303.

27. Mullins, W.W., *Solid surface morphologies governed by capillarity.* Metal Surfaces: Structure, energetics and kinetics, 1963: p. 17-66.

28. Orchard, S., *On surface levelling in viscous liquids and gels.* Applied Scientific Research, Section A, 1963. **11**(4-6): p. 451-464.

29. Carter, G., M. Nobes, and I. Katardjiev, *The production of repetitive surface features by oblique incidence ion bombardment.* Philosophical Magazine B, 1993. **68**(2): p. 231-236.

30. Bradley, R.M. and J.M. Harper, *Theory of ripple topography induced by ion bombardment.* Journal of Vacuum Science & Technology A: Vacuum, Surfaces, and Films, 1988. **6**(4): p. 2390-2395.

31. Herring, C., *Diffusional viscosity of a polycrystalline solid.* Journal of Applied Physics, 1950. **21**: p. 437.

32. Mullins, W.W., *Theory of thermal grooving.* Journal of Applied Physics, 1957. **28**(3): p. 333-339.

33. Makeev, M.A. and A.-L. Barabási, *Ion-induced effective surface diffusion in ion sputtering.* Applied physics letters, 1997. **71**(19): p. 2800-2802.

34. Bradley, R.M. and J.M.E. Harper, *Theory of ripple topography induced by ion bombardment.* Journal of Vacuum Science & Technology A: Vacuum, Surfaces, and Films, 1988. **6**(4): p. 2390-2395.

35. Madi, C.S., et al., *Mass redistribution causes the structural richness of ion-irradiated surfaces.* Physical review letters, 2011. **106**(6): p. 066101.

36. Norris, S.A., et al., *Molecular dynamics of single-particle impacts predicts phase diagrams for large scale pattern formation.* Nature communications, 2011. **2**: p. 276.

37. Davidovitch, B., M.J. Aziz, and M.P. Brenner, *On the stabilization of ion sputtered surfaces.* Physical Review B, 2007. **76**(20): p. 205420.

38. Ziberi, B., et al., *Ripple pattern formation on silicon surfaces by low-energy ion-beam erosion: Experiment and theory.* Physical Review B, 2005. **72**(23): p. 235310.

39. Ziberi, B., et al., *Highly ordered nanopatterns on Ge and Si surfaces by ion beam sputtering.* Journal of Physics: Condensed Matter, 2009. **21**(22): p. 224003.

40. Ozaydin, G., et al., *Real-time x-ray studies of Mo-seeded Si nanodot formation during ion bombardment.* Applied physics letters, 2005. **87**(16): p. 163104-163104-3.

41. Hofsäss, H. and K. Zhang, *Surfactant sputtering.* Applied Physics A, 2008. **92**(3): p. 517-524.

42. Sánchez-García, J., et al., *Tuning the surface morphology in self-organized ion beam nanopatterning of Si (001) via metal incorporation: from holes to dots.* Nanotechnology, 2008. **19**: p. 355306.

43. Macko, S., et al., *Is keV ion-induced pattern formation on Si (001) caused by metal impurities?* Nanotechnology, 2010. **21**: p. 085301.

44. Zhou, J., et al., *Nanopatterning of Si surfaces by normal incident ion erosion: Influence of iron incorporation on surface morphology evolution.* Journal of Applied Physics, 2011. **109**(10): p. 104315-104315-6.

45. El-Atwani, O., et al., *Formation of silicon nanodots via ion beam sputtering of ultrathin gold thin film coatings on Si.* Nanoscale research letters, 2011. **6**(1): p. 1-5.

46. Cornejo, M., et al., *Self-organized patterning on Si (001) by ion sputtering with simultaneous metal incorporation.* Applied Physics A: Materials Science & Processing, 2011. **102**(3): p. 593-599.

47. Ozaydin-Ince, G. and K. Ludwig Jr, *In situ X-ray studies of native and Mo-seeded surface nanostructuring during ion bombardment of Si (100).* Journal of Physics: Condensed Matter, 2009. **21**: p. 224008.

48. Bradley, R.M., *Theory of nanodot and sputter cone arrays produced by ion sputtering with concurrent deposition of impurities.* Physical Review B, 2011. **83**(19): p. 195410.

49. Pietsch, U., V. Holý, and T. Baumbach, *High-resolution X-ray scattering from thin films to lateral nanostructures*2004: Springer Verlag.

50. Tolan, M., *X-ray scattering from soft-matter thin films*1999: Springer Berlin.

51. Als-Nielsen, J. and D. McMorrow, *Elements of modern X-ray physics*2011: John Wiley & Sons.

52. Born, M. and E. Wolf, *Principles of optics: electromagnetic theory of propagation, interference and diffraction of light*1999: CUP Archive.

53. Gerhard, T., W. Faschinger, and G. Landwehr, *Depth-sensitive X-ray diffraction using extremely asymmetrical reflections by variation of the wavelength.* Semiconductor science and technology, 1998. **13**(6): p. 583.

54. Ress, H., W. Faschinger, and G. Landwehr, *Depth-dependent x-ray diffraction using extremely asymmetric reflections.* Journal of Physics D: Applied Physics, 1998. **31**(22): p. 3272.

55. Möller, M., et al., *New methods for depth profiling of heterostructures by X-ray diffraction.* Il Nuovo Cimento D, 1997. **19**(2-4): p. 321-328.

56. Abeles, F., *Investigations on the propagation of sinusoidal electromagnetic waves in stratified media. Application to thin films.* Ann. Phys.(Paris), 1950. **5**: p. 596-640.

57. Berreman, D., *Dynamical theory of x-ray diffraction in flat, focusing, and distorted crystals by Abelés's matrix method.* Physical Review B, 1976. **14**(10): p. 4313.

58. Parratt, L.G., *Surface studies of solids by total reflection of X-rays.* Physical Review, 1954. **95**(2): p. 359.

59. Nevot, L. and P. Croce, *Caractérisation des surfaces par réflexion rasante de rayons X. Application à l'étude du polissage de quelques verres silicates.* Revue de Physique appliquée, 1980. **15**(3): p. 761-779.

60. Bragg, W., *The structure of some crystals as indicated by their diffraction of X-rays.* Proceedings of the Royal Society of London. Series A, 1913. **89**(610): p. 248-277.

61. Berman, L.E. and M. Hart, *Preserving the high finesse of X-ray undulator beams from perfect water-jet-cooled diamond monochromators.* Nuclear Instruments and Methods in Physics Research Section A: Accelerators, Spectrometers, Detectors and Associated Equipment, 1993. **334**(2): p. 617-620.

62. Bowen, D.K. and B.K. Tanner, *High resolution X-ray diffractometry and topography* 1998: CRC Press.

63. Authier, A., *Dynamical theory of X-ray diffraction*2001: Wiley Online Library.

64. Battermann, B. and H. Cole, *See for instance Rev.* Mod. Phys, 1964. **36**: p. 681.

65. Pietsch, U. and W. Borchard, *Lattice-parameter-difference measurement of heteroepitaxial structures by means of extremely asymmetrical Bragg diffraction.* Journal of applied crystallography, 1987. **20**(1): p. 8-10.

66. Rustichelli, F., *On the deviation from the Bragg law and the widths of diffraction patterns in perfect crystals.* Philosophical Magazine, 1975. **31**(1): p. 1-12.

67. Bucksch, R., J. Otto, and M. Renninger, *DieDiffraction Pattern'des Idealkristalls fur Rontgenstrahlinterferenzen im Bragg-Fall.* Acta Crystallographica, 1967. **23**(4): p. 507-511.

68. Biermanns, A., et al., *X-ray scattering and diffraction from ion beam induced ripples in crystalline silicon.* Journal of Applied Physics, 2008. **104**(4): p. 044312-044312-5.

69. Pietsch, U., V. Holy, and T. Baumbach, *High-resolution X-ray scattering: from thin films to lateral nanostructures* 2004: Springer.

70. Bruhl, H.-G., et al., *Extreme asymmetric X-ray Bragg reflection of semiconductor heterostructures near the edge of total external reflection.* Journal of applied crystallography, 1990. **23**(4): p. 228-233.

71. Watts, J.F. and J. Wolstenholme, *An introduction to surface analysis by XPS and AES.* An Introduction to Surface Analysis by XPS and AES, by John F. Watts, John Wolstenholme, pp. 224. ISBN 0-470-84713-1. Wiley-VCH, May 2003., 2003. **1**.

72. Seah, M. and W. Dench, *Quantitative electron spectroscopy of surfaces: a standard data base for electron inelastic mean free paths in solids.* Surface and interface analysis, 1979. **1**(1): p. 2-11.

73. Stern, E., D. Sayers, and F. Lytle, *Extended x-ray-absorption fine-structure technique. III. Determination of physical parameters*. Physical Review B, 1975. **11**(12): p. 4836.

74. Lee, P.A. and J.B. Pendry, *Theory of the extended x-ray absorption fine structure.* Physical Review B, 1975. **11**(8): p. 2795-2811.

75. Müller, J.E. and J.W. Wilkins, *Band-structure approach to the x-ray spectra of metals.* Physical Review B, 1984. **29**(8): p. 4331-4348.

76. Gurman, S. and R. Pettifer, *EXAFS study of the structure of amorphous and crystalline arsenic oxide.* Philosophical Magazine B, 1979. **40**(5): p. 345-359.

77. Sayers, D.E., E.A. Stern, and F.W. Lytle, *New technique for investigating noncrystalline structures: Fourier analysis of the Extended X-Ray absorption Fine Structure.* Physical review letters, 1971. **27**(18): p. 1204-1207.

78. Teo, B.K., *EXAFS: basic principles and data analysis*. Vol. 9. 1986: Springer-Verlag Berlin.

79. Lee, P., B.-K. Teo, and A. Simons, *EXAFS: A new parameterization of phase shifts.* Journal of the American Chemical Society, 1977. **99**(11): p. 3856-3859.

80. Teo, B.-K. and P. Lee, *Ab initio calculations of amplitude and phase functions for extended X-ray absorption fine structure spectroscopy.* Journal of the American Chemical Society, 1979. **101**(11): p. 2815-2832.

81. Mills, D.M., *Third-generation hard X-ray synchrotron radiation sources: source properties, optics, and experimental techniques.* Third-Generation Hard X-Ray Synchrotron Radiation Sources: Source Properties, Optics, and Experimental Techniques, by Dennis M. Mills (Editor), pp. 406. ISBN 0-471-31433-1. Wiley-VCH, March 2002., 2002. **1**.

82. Lutzenkirchen-Hecht, D., et al., *The materials science X-ray beamline BL8 at the DELTA storage ring.* Journal of Synchrotron Radiation, 2009. **16**(2): p. 264-272.

83. Tolan, M., et al., *DELTA: Synchrotron light in nordrhein-westfalen.* 2003.

84. Ravel, B. and M. Newville, *ATHENA, ARTEMIS, HEPHAESTUS: data analysis for X-ray absorption spectroscopy using IFEFFIT.* Journal of Synchrotron Radiation, 2005. **12**(4): p. 537-541.

85. Berges, U., S. Döring, and C. Westphal. *PGM-Beamline at the Undulator U55 at DELTA*. in *AIP Conference Proceedings*. 2007.

86. Wojdyr, M., *Fityk: a general-purpose peak fitting program.* Journal of applied crystallography, 2010. **43**(5): p. 1126-1128.

87. Horcas, I., et al., *WSXM: a software for scanning probe microscopy and a tool for nanotechnology.* Review of Scientific Instruments, 2007. **78**: p. 013705.

88. Doolittle, L.R., *Algorithms for the rapid simulation of Rutherford backscattering spectra.* Nuclear Instruments and Methods in Physics Research Section B: Beam Interactions with Materials and Atoms, 1985. **9**(3): p. 344-351.

89. Zhao, Y., et al., *Characterization of Amorphous and Crystalline Rough Surface-Principles and Applications*. Vol. 37. 2000: Access Online via Elsevier.

90. Möller, W. and W. Eckstein, *Tridyn-a TRIM simulation code including dynamic composition changes.* Nuclear Instruments and Methods in Physics Research Section B: Beam Interactions with Materials and Atoms, 1984. **2**(1): p. 814-818.

91. Custer, J., et al., *Density of amorphous Si.* Applied physics letters, 1994. **64**(4): p. 437-439.

92. Bruhl, H.-G., U. Pietsch, and B. Lengeler, *Investigation of (Ga, In)(As,P)/InP single heterostructures by means of extremely asymmetrical Bragg diffraction using synchrotron radiation.* Journal of applied crystallography, 1988. **21**(3): p. 240-244.

93. Klasson, M., et al., *Electron escape depth in silicon.* Journal of Electron Spectroscopy and Related Phenomena, 1974. **3**(6): p. 427-434.

94. Nakazawa, M., S. Kawase, and H. Sekiyama, *Investigations of the SiO_2/Si interface. I. Oxidation of a clean Si (100) surface using photoemission spectroscopy with synchrotron radiation.* Journal of Applied Physics, 1989. **65**(10): p. 4014-4018.

95. Nakazawa, M., et al., *Investigation of the SiO 2/Si interface. II. Oxidation of an HF-cleaned Si (100) surface using photoemission spectroscopy with synchrotron radiation.* Journal of Applied Physics, 1989. **65**(10): p. 4019-4023.

96. Chen, M., I.P. Batra, and C. Brundle, *Theoretical and experimental investigations of the electronic structure of oxygen on silicon.* Journal of Vacuum Science and Technology, 1979. **16**(5): p. 1216-1220.

97. Ciraci, S., S. Ellialtioğlu, and S. Erkoc, *Interpretation of the spectra obtained from oxygen-adsorbed and oxidized silicon surfaces.* Physical Review B, 1982. **26**(10): p. 5716.

98. Hollinger, G. and F. Himpsel, *Multiple-bonding configurations for oxygen on silicon surfaces.* Physical Review B, 1983. **28**: p. 3651-3653.

99. Shabanova, I., et al., *Dependence of saturation magnetization of nickel aerosol powders on the state of surface particles studied by photoelectron spectroscopy.* Fiz. Metal. Metalloved, 1974. **38**: p. 314-322.

100. Pronin, I., et al., *Magnetic-dichroism study of iron silicides formed at the Fe/Si (100) interface.* Applied Physics A, 2009. **94**(3): p. 467-471.

101. Bertoncini, P., et al., *Epitaxial growth of Fe (001) on $CoSi_2$(001)/Si (001) surfaces: Structural and electronic properties.* Physical Review B, 1999. **60**(15): p. 11123.

102. Gomoyunova, M., et al., *Interaction of iron atoms with the Si (100)-2×1 surface.* Technical physics, 2005. **50**(9): p. 1212-1216.

103. Pronin, I., et al., *Magnetic linear dichroism in photoemission from an ultrathin iron silicide film.* Physics of the Solid State, 2008. **50**(3): p. 553-556.

104. Kläsges, R., et al., *Formation of a ferromagnetic silicide at the Fe/Si(100) interface.* Physical Review B, 1997. **56**(17): p. 10801-10804.

105. Egert, B. and G. Panzner, *Bonding state of silicon segregated to α-iron surfaces and on iron silicide surfaces studied by electron spectroscopy.* Physical Review B, 1984. **29**(4): p. 2091.

106. Grunthaner, F., et al., *Local atomic and electronic structure of oxide/GaAs and SiO 2/Si interfaces using high‐resolution XPS.* Journal of Vacuum Science and Technology, 1979. **16**(5): p. 1443-1453.

107. Sánchez-García, J., et al., *Production of nanohole/nanodot patterns on Si (001) by ion beam sputtering with simultaneous metal incorporation.* Journal of Physics: Condensed Matter, 2009. **21**: p. 224009.

108. Sirotti, F., M. De Santis, and G. Rossi, *Synchrotron-radiation photoemission and x-ray absorption of Fe silicides.* Physical Review B, 1993. **48**(11): p. 8299.

109. Gomoyunova, M., et al., *Initial stages of iron silicide formation on the Si (100) 2×1 surface.* Surface Science, 2007. **601**(21): p. 5069-5076.

110. Gomoyunova, M., et al., *Initial stages of silicon-iron interface formation.* Technical Physics Letters, 2013. **39**(4): p. 360-363.

111. Nikolaeva, M., et al., *Iron silicide formed in a-Si: Fe thin films by magnetron co-sputtering and ion implantation.* Vacuum, 2002. **69**(1): p. 221-225.

112. Khanbabaee, B., et al., *Depth profile investigation of the incorporated iron atoms during Kr^+ ion beam sputtering on Si (001).* Thin Solid Films, 2013. **527**: p. 349-353.

113. Carbone, D., et al., *Ion-induced nanopatterns on semiconductor surfaces investigated by grazing incidence x-ray scattering techniques.* Journal of Physics: Condensed Matter, 2009. **21**: p. 224007.

114. Khanbabaee, B., et al., *Depth profiling of Fe-implanted Si (100) by means of X-ray reflectivity and extremely asymmetric X-ray diffraction.* Journal of applied crystallography, 2013. **46**(2): p. 505-511.

115. Moroni, E., et al., *Cohesive, structural, and electronic properties of Fe-Si compounds.* Physical Review B, 1999. **59**(20): p. 12860.

116. Starke, U., et al., *Structural and compositional reversible phase transitions on low-index Fe3Si surfaces.* EPL (Europhysics Letters), 2001. **56**(6): p. 822.

117. Dusausoy, Y., et al., *Structure cristalline du disiliciure de fer, $FeSi_2$.* Acta Crystallographica Section B: Structural Crystallography and Crystal Chemistry, 1971. **27**(6): p. 1209-1218.

118. Milosavljevic, M., et al., *Growth of β-$FeSi_2$ films via noble-gas ion-beam mixing of Fe/Si bilayers.* Journal of Applied Physics, 2001. **90**(9): p. 4474-4484.

119. Nakanishi, O., A. Yanase, and A. Hasegawa, *Electronic energy band structure of MnSi.* Journal of Magnetism and Magnetic Materials, 1980. **15**: p. 879-880.

120. Dahal, N. and V. Chikan, *Phase-Controlled Synthesis of Iron Silicide (Fe_3Si and $FeSi_2$) Nanoparticles in Solution.* Chemistry of Materials, 2010. **22**(9): p. 2892-2897.

121. Li, G., et al., *X-ray diffraction investigation of native Si-Fe alloy minerals from Luobusha, Tibet.* Frontiers of Earth Science in China, 2007. **1**(1): p. 21-25.

122. Lin, X., et al., *Low-temperature ion-induced epitaxial growth of α-$FeSi_2$ and cubic $FeSi_2$ in Si.* Applied physics letters, 1993. **63**(1): p. 105-107.

123. Onda, N., et al., *Epitaxy of fluorite-structure silicides: metastable cubic $FeSi_2$ on Si (111).* Applied Surface Science, 1992. **56**: p. 421-426.

124. Derrien, J., et al., *Semiconducting silicide-silicon heterostructures: growth, properties and applications.* Applied Surface Science, 1992. **56**: p. 382-393.

125. Birkholz, U. and J. Schelm, *Mechanism of Electrical Conduction in β-$FeSi_2$.* physica status solidi (b), 1968. **27**(1): p. 413-425.

126. Chevrier, J. and J. Derrien, *Epitaxial growth of Fe-Si compounds on the silicon (111) face.* Physical Review B, 1992. **46**(24): p. 15946.

127. Desimoni, J., et al., *Ion-beam-induced simultaneous epitaxial growth of α-and cubic $FeSi_2$ in Si (100) at 320° C.* Nuclear Instruments and Methods in Physics Research Section B: Beam Interactions with Materials and Atoms, 1993. **80**: p. 755-758.

128. Rix, W., *Über Eisensilicide: Züchtung von β-FeSi2-Einkristallen durch chemischen Transport, strukturelle und physikalische Charakterisierung*, 2001, Universitätsbibliothek Freiburg.

129. Ishimaru, M., et al., *Formation process of β-$FeSi_2$/Si heterostructure in high-dose Fe ion implanted Si.* Journal of Applied Physics, 2006. **99**(11): p. 113527-113527-7.

130. Gumarov, G., et al., *Effect of ion current density on the phase composition of ion beam synthesized iron silicides in Si (100).* Nuclear Instruments and Methods in Physics Research Section B: Beam Interactions with Materials and Atoms, 1997. **127**: p. 321-323.

131. Desimoni, J., et al., *Ion beam synthesis of cubic $FeSi_2$.* Applied physics letters, 1993. **62**(3): p. 306-308.

132. Katsumata, H., et al., *Fabrication of heterostructure p-β-$Fe_{0.95}$ $Mn_{0.05}Si_2$/n-Si diodes by Fe^+ and Mn^+ co-implantation in Si (100) substrates.* Thin Solid Films, 2001. **381**(2): p. 244-250.

133. Cullity, B.D. and S.R. Stock, *Elements of X-ray Diffraction*. Vol. 3. 2001: Prentice hall Upper Saddle River, NJ.

134. Darakchieva, V., et al., *Effect of rapid thermal annealing on the structure of ion beam synthesized β-$FeSi_2$.* Vacuum, 2002. **69**(1): p. 449-454.

135. Fewster, P.F., *Reciprocal space mapping.* Critical Reviews in Solid State and Material Sciences, 1997. **22**(2): p. 69-110.

136. Tan, Z., et al., *Silicide formation and structural evolution in Fe-, Co-, and Ni-implanted silicon.* Physical Review B, 1992. **46**(7): p. 4077.

137. Pesek, A., et al., *Distribution of strain in Ge ion implanted silicon measured by high resolution X-ray diffraction.* Nuclear Instruments and Methods in Physics Research Section B: Beam Interactions with Materials and Atoms, 1993. **80**: p. 569-572.

138. Tsai, C., et al., *Self-consistent determination of the perpendicular strain profile of implanted Si by analysis of x-ray rocking curves.* Journal of Applied Physics, 1991. **69**(4): p. 2076-2079.

139. Hart, L. and J. Matsui, *X-ray characterization of ion-implanted and rapid thermal annealed silicon.* Semiconductor science and technology, 1992. **7**(3): p. 291.

140. van Berlo, W. and T. Pihl, *X-ray diffraction studies of radiation damage in gallium arsenide.* Nuclear Instruments and Methods in Physics Research Section B: Beam Interactions with Materials and Atoms, 1991. **55**(1): p. 785-788.

141. Naito, M., et al., *Solid phase crystallization of amorphous Fe–Si layers synthesized by ion implantation.* Applied physics letters, 2006. **88**(25): p. 251904-251904-3.

142. Ziberi, B., et al., *Highly ordered nanopatterns on Ge and Si surfaces by ion beam sputtering.* Journal of Physics: Condensed Matter, 2009. **21**: p. 224003.

143. Macko, S., et al., *Phenomenology of iron-assisted ion beam pattern formation on Si (001).* New Journal of Physics, 2011. **13**(7): p. 073017.

144. Bradley, R.M. and P.D. Shipman, *A surface layer of altered composition can play a key role in nanoscale pattern formation induced by ion bombardment.* Applied Surface Science, 2012. **258**(9): p. 4161-4170.